12-16-2013 12:00 AM

High Pressure- Temperature Electrical Resistivity Experiments on Fe-Si Alloys Bearing on Conductive Heat Flow at the Top of the Outer Core

Soushyant Kiarasi
The University of Western Ontario

Supervisor
Dr. Richard A. Secco
The University of Western Ontario

Graduate Program in Geophysics
A thesis submitted in partial fulfillment of the requirements for the degree in Doctor of Philosophy

Recommended Citation

Kiarasi, Soushyant, "High Pressure- Temperature Electrical Resistivity Experiments on Fe-Si Alloys Bearing on Conductive Heat Flow at the Top of the Outer Core" (2013). *Electronic Thesis and Dissertation Repository*. 1793.
https://ir.lib.uwo.ca/etd/1793

HIGH PRESSURE- TEMPERATURE ELECTRICAL RESISTIVITY EXPERIMENTS ON Fe-Si ALLOYS BEARING ON CONDUCTIVE HEAT FLOW AT THE TOP OF THE OUTER CORE

(Thesis format: Monograph)

by

Soushyant Kiarasi

Graduate Program in Geophysics

A thesis submitted in partial fulfillment
of the requirements for the degree of
Doctor of Philosophy

The School of Graduate and Postdoctoral Studies
The University of Western Ontario
London, Ontario, Canada

Abstract

The electrical resistivity of Fe17wt%Si alloy was measured within the solid and the liquid phases up to 5 GPa in 200 ton and 1000 ton cubic anvil presses. Special attention was paid in the investigation to the challenges in resistance measurements in connection with the contaminations originating from the electrode materials and also the dominant role of the electrode resistances in the final results. The current results on Fe17Si alloys yielded insights to the manifestations of the magnetic, order-disorder and melting transitions on the electrical resistivity at high P, T. A drop in electrical resistivity in Fe17Si was observed at the melting boundary at high pressures up to 5 GPa as reported by Baum et al. (1967) at 1 atm. The liquid resistivity results from the present study provide insight on the effect of Si on the electrical resistivity of Fe-Si alloy specifically that the difference in resistivity between Fe and Fe17Si decreased with increasing pressure. The model of saturation resistivity (Mooij, 1973) describes saturation of electron-scattering where the electron mean free path approaches the interatomic distance (Ioffe-Regel criteria); the temperature coefficient of resistivity (TCR) has been shown to change sign due to compositionally-induced changes to the mean free path and interatomic distance. The results of the present study show that pressure can also provide a mechanism for resistivity saturation and change of TCR sign most likely due to reduction in interatomic distance. The present electrical resistivity results of Fe17Si were interpreted in terms of the resistivity saturation model in order to estimate the electrical resistivity of the Earth's outer core. This yielded a range of $9.0\times10^{-7}\Omega$m to $9.4\times10^{-7}\Omega$m which is in agreement with the very recently reported studies on the electrical resistivity of the Earth's core. Using Wiedemann-Franz law, electrical thermal conductivities were calculated to be 103 $\mathrm{Wm^{-1}K^{-1}}$ to 109 $\mathrm{Wm^{-1}K^{-1}}$.

Keywords Electrical resistivity, Fe17wt%Si alloy, high pressure, cubic anvil press, phase transition, magnetic transition, order-disorder transition, Wiedemann-Franz law.

Author's Declaration

I hereby declare that I am the sole author of this thesis. This is a true copy of the thesis, including any required final revisions, as accepted by my examiners.

I understand that my thesis may be made electronically available to the public.

Acknowledgments

First and foremost, I would like to express my sincere thanks to my supervisor, Dr. Richard A. Secco for offering me the opportunity to get involved in the high pressure mineral physics field of research. I am so much grateful for his immense knowledge, all his constructive guidance during my research and his dedication, careful and critical proofreading of my thesis.

My sincere thanks go to Dr. Wenjun Yong for his encouragement, insightful comments and invaluable friendship during the past years of my research.

I am indebted to Jon Jacobs for all I learned from him in the Earth Sciences Departmental Machine Shop. This work would truly not be possible without him. His expertise, innovation, patience, heartfelt support and spiritual encouragement meant a lot to me.

I would also like to thank my fellow labmates Ryan Sawyer, Sean Funk, Tim Officer, Innocent Ezenwa, Marie April Burford, Xueyang Yu and Reynold Sukara for all the wonderful time we had together, and for their invaluable friendship and support.

I would also like to thank Steve Wood for his help in the post experiment sample preparation.

Separate thanks go to John Brunet for all his sincere support and his kind heart.

There is no word to express how much I am in debt to Dr. Karen Assatourians and Dr. Hadi Ghofrani for their invaluable friendship and their sincere support since my arrival in Canada.

Last but not the least; this work could not have been done without the spiritual support, encouragement and endless patient of my Lovely parents Soorya and Hamid and my lovely brothers Sourena and Kiarash. Thank you so much!

Table of Contents

List of Tables

List of Figures

CHAPTER 1

1 Introduction

1.1 Core composition and light elements

The geomagnetic field is generated via dynamo action in Earth's core which is little more than half the radius of Earth. There is no direct access to the source region of the geomagnetic field. On the other hand, core-generated features are not limited solely to the geomagnetic field. Cooling of the Earth's core drives mantle convection and consequently plate tectonics on the surface (Stacey, 2008). Therefore, obtaining information regarding the nature of the Earth's core, including its composition, is fundamental to get a better understanding of the evolution and the current dynamics of the planet.

The composition of Earth's core, both its inner and outer cores, has been debated for a long time. There is overwhelming evidence that Fe is the main constituent of the outer core with approximately 10wt% Ni. However, Birch (1952), put forward the proposition that the outer core is not as dense as Fe and 10 wt% Ni. For the past 60 years, the debate has focused on what other elements are also present in the outer core along with Fe and Ni. Seismic waves and normal mode oscillations of the Earth offer two direct probes of its core and have independently confirmed a 10% density deficit in the outer core compared with an outer core made entirely of Fe and Ni. The existence of light elements alloying with Fe is required in order to justify the “missing mass” inside the Earth’s most inaccessible part. Not every light element can be considered as a core additive. Preferences for a light element are given primarily to candidates that: 1) are cosmochemically in great abundance during the accretionary stages of Earth; 2) elements that can dissolve easily in molten Fe under core-forming P and T conditions; 3) light elements whose physical properties, to the extent they are known, can promote generation of a magnetic field through dynamo action and with geochemically acceptable concentration ranges that can explain the observed density deficit at outer core P and T conditions. After satisfying these criteria, the list of proposed light elements is not a long one. In a critical review paper by Poirier (1994), the most likely candidates are suggested to be silicon, oxygen, sulfur, carbon and hydrogen. An extensive body of theoretical and experimental work has been carried out to determine the candidacy of: **S** (e.g. melting experiments: Williams and Jeanloz, 1990; theoretical calculation of electronic structure and phase stability: Sherman, 1991, 1995, 1997; phase diagram: Li et al., 2001; Morard et al., 2008; first principle calculations of elasticity: Vočadlo, 2007; electronic structure calculations: Côté et al., 2008), **O** (e.g. theoretical calculation of electronic structure and phase stability: Sherman, 1991, 1995; first principle calculations for equation of state of Fe: Stixrude et al., 1997; solubility studies of oxygen: Rubie et al., 2004; sound velocity measurements: Badro et al., 2007; partitioning coefficient study: Asahara et al., 2007; Corgne et al., 2009), **C** (experiment and thermodynamic calculation: Wood, 1993; Wood et al., 2006; Litasov et al., 2013 ; melting experiments: Dasgupta et al., 2009; Hirschmann and Dasgupta, 2009; carbon isotope fractionation experiments: Satish-

Kumar et al., 2011; Wood et al., 2013), **H** (solubility experiment: Fukai,1984; Badding et al., 1991; exchange partition coefficient experiments: Isaev et al., 2007; melting experiments: Sakamaki et al., 2009; sound velocity measurements: Shibazaki et al., 2012) and **Si,** which is discussed in the rest of the chapter and summarized in Table1.1. The issue is so challenging that a competition between these candidates has been continuing for decades with no distinct priority given to any of the candidate so far as a leading constituent of the core light elements. While some studies have proposed incorporation of binary, ternary or even quaternary mixtures instead of a single element alloying in the core (Allègre et al., 1995; Javoy, 1995; O'Neill et al., 1998; Hillgren et al., 2000; Alfé et al., 2002a, 2002b; McDonough, 2003; Siebert et al., 2005, Sanloup and Fei, 2004), this thesis focuses on Si as the light alloying element.

1.2 Geochemical constraints on candidacy of Si in the Earth's core

Taking a single light element alloy model in the outer core, Si could be an appealing target from the cosmochemical point of view because it is the most readily abundant element during the stages of Earth accretion. Comparison of the average composition of the bulk silicate Earth and that of chondritic meteorites as the building blocks of the terrestrial planets, and the elevated Mg/Si ratio of Earth's upper mantle, provide the strongest piece of evidence for the candidacy of Si in the outer core (Allègre et al., 1995; Drake and Righter, 2002; Fitoussi et al., 2009; Tuff et al., 2011). Very recent Si stable isotope studies, which focused on the differences observed between terrestrial samples and meteorites, also have yielded supporting information for the Si candidacy (Shahar et al. 2009, Ziegler et al. 2010). Based on the experimental findings, silicate has higher $^{30}Si/^{28}Si$ than metal which suggests that during Earth's core formation ^{28}Si may have diffused to the metallic core. The ^{28}Si migration left high ^{30}Si/^{28}Si signature of the bulk silicate Earth due to dissolution of ~6 wt% Si into the early core (Shahar et al. 2011).

1.3 Si solubility in the molten outer core

The solubility of Si in liquid Fe plays an important role in its candidacy which has raised significant debates. Pressure, temperature and oxygen fugacity are the three most important factors that can affect the partitioning of Si in Fe. In a very recent and comprehensive study by Ricolleau et al. (2011), after examining many possible core formation scenarios with different fO_2, they reported Si to be the main alloying element of the outer core with a range from 5 to 11 wt%. According to Ricolleau et al. (2011) study, decreasing oxygen fugacity (fO_2) can significantly increase the Si solubility in molten Fe. An appropriate value of fO_2 depends on the chosen core formation model. Even with fO_2 fixed, the solubility of Si in liquid Fe has been shown to be positively correlated with temperature and pressure (Ringwood and Hibberson, 1991; Ito and Morooka, 1995; Kilburn and Wood, 1997; O'Neill et al., 1998; Gessmann et al., 2001). Therefore, Si becomes a favorable candidate for both inner and outer core within the list of light elements.

1.4 Density deficit in the Earth’s core

Any supporting evidence of the candidacy of Si based on cosmochemistry as well as experimental data on the solubility of Si in molten Fe is required to pass the density deficit test in order to be accepted as a valid supposition. Robust results from several studies support Si as a potential light-element constituent of Earth’s core based on both density and velocity data (Badro et al., 2007; Funtikov et al., 2007; Antonangeli et al., 2010; Sata et al., 2010). The amount of Si that can account for 1% density deficit in the core varies from 1.5wt% to 3 wt% (Guyot et al., 1997; Zhang and Guyot, 1999; Lin et al., 2002; Hirao et al., 2004). If a linear relationship (i.e. ideal mixing) can be assumed between density deficit and concentration of Si (Sata et al., 2010), 6-10% density deficit in outer core and 1-3% in the inner core (Li and Fei, 2003) yields the presence of 11-19wt. % Si in outer core and 1.5 -5.5 wt. % Si in the inner core. If one considers a non-ideal volume of mixing with a negative value of the excess mixing molar volume of Si (Tateyama et al., 2011), the anticipated Si composition will be even higher based on the density deficit argument.

1.5 Sound velocity

Sound velocity comparison between the real Earth's profile and that of the Fe alloys can independently put constraints on Earth's core composition. The bulk sound velocity of the outer core is suggested to be 3% higher than that of pure liquid Fe (Anderson and Ahrens, 1994). Based on sound velocity and density compatibility with the Preliminary Reference Earth Model (PREM), studies have suggested evidence that substitution of Si in Fe increases the V_p and V_s at high pressures at a given density for different Si concentrations (Lin et al., 2003a, 2003b; Dobson et al., 2003; Hirao et al., 2004; Badro et al., 2007; Funtikov et al., 2007; Antonangeli et al., 2010; Mao et al., 2012). Following these results, various Siwt% has been suggested to match the sound velocity requirements under core conditions as shown in Table1.1.

Table 1.1 Summary of recent studies on FeSi alloys

Author	Method	Si wt%
Lin et al. (2003a)	Static compression of Fe-Si alloy	8-10 (outer core); 4 (inner core)
Li and Fei (2003)	Density deficit	11-19 (outer core); 1.5-5.5 (inner core)
Hiaro et al. (2004)	Density and sound velocity measurement	3-5 (inner core)
Wade and Wood (2005)	Partitioning of sidrophile trace elements	5-7
Sakai et al. (2006)	Solubility of Si and O in molten Fe	4 core-mantle boundary(CMB)
Wood et al. (2006)	Metal–silicate partitioning	5
Badro et al. (2007)	Sound velocity	2.8 (outer core); 2.3 (inner core)
Chen et al. (2007)	Thermal expansion of Fe-Si	11-19
Funtikov et al. (2007)	Density and sound velocity measurement	10 (outer core)
Asanuma et al. (2008)	Phase relations of Fe–Si alloy	3.4 (inner core)
Shahar et al. (2009)	Si isotope studies	6
Fitoussi et al. (2009)	Si isotope studies	6-8
Antonangeli et al. (2010)	Sound velocity measurements	1-2 (inner core)
Sata et al. (2010)	Density deficit	12.5
Ziegler et al. (2010)	Si isotope studies	6
Tuff et al. (2011)	Metal–silicate partitioning	4.3
Ricolleau et al. (2011)	Partition coefficients for silicon	5-11(outer core)
Mao et al. (2012)	Sound velocity	8 (inner core)

1.6 Electrical resistivity of Fe-Si alloys and objectives of the study

The geomagnetic dynamo is a robust feature of the Earth that requires a metallic core. This provides an independent constraint on the Earth's core constituents. As one of the independent constraints on the Si candidacy, the contribution of Si to the electrical resistivity of Fe-Si alloy under relevant Earth's core pressure and temperature can be examined. If one decides to rely on the simplest scenario of Si to be the single light element, its presence should promote generation of a magnetic field through dynamo action. The minimum conductivity requirement for the Earth's dynamo is estimated to be 2.5×10^{5} Sm^{-1} which is equivalent to a resistivity of 4×10^{-6} Ωm (Stacey, 2008). This is within the range of values estimated for the electrical conductivity of Fe under core's condition (Stacey and Anderson, 2001). The electrical conductivity of Fe, as central property of the Earth's core will be also modified by alloying with lighter elements. Silicon contents ranging from 0.2 to 23.18 wt% have proven to meet the minimum electrical conductivity requirements for dynamo action (Bridgman, 1957; Matassov, 1977). On the other hand, the existence of a metallic core explicitly implies also a thermal conductivity of the core to be of metallic characteristic which means continuous conductive heat transport in the core. That imposes a serious requirement for the sustainable core dynamo energy source. A factor of two uncertainty in electrical resistivity does not appear critical to dynamo action but it has a strong impact on thermal evolution of the core. Therefore, Earth's core thermal budget imposes a lower limit on the electrical resistivity of the Earth's core. The lower limit of electrical resistivity itself relies on the thermal evolution models of the Earth's core. There is no consensus on the thermal evolution models and consequently on the lower bound electrical resistivity values of the core's constituents. Although the lower limit of electrical resistivity for Fe alloys is debatable, shock wave studies as well as very recent theoretical calculations and experiments (Keeler and Mitchell, 1969; Keeler and Royce, 1971; Matassov, 1977; Gomi et al., 2013; Pozzo et al., 2012 and 2013) suggest Fe-Si alloys offer lower electrical resistivity under core condition than previous studies (Stacey and Anderson, 2001).

Despite the vital importance of the high pressure and high temperature electrical resistivity values for liquid Fe-Si alloys, except for limited studies of Yang (1999), no high P,T experimental study so far has been reported on liquid Fe-Si alloys. For the first time, a more detailed study on the electrical resistivity of liquid Fe17wt%Si (Fe17Si) was carried out up to 5 GPa and high temperatures up to 1700^{o}C in the present research. This specific composition is on the upper limit of the proposed light element Si composition of the core (Poirier, 1994). Comparing the electrical resistivity of Fe17Si from the present research and that of pure Fe can shed light on the physics of electronic scattering mechanisms in Fe-Si alloys with high Si composition which in turn will have implication on the candidacy of Si as a light alloying in the Earth's core.

CHAPTER 2

2 General experimental methods

2.1 High pressure apparatus

All electrical resistivity experiments were carried out in either a 200 ton or a 1000 ton press (Figure 2.1). Both apparatuses function on the hydraulically-driven symmetrical advance of six tungsten carbide anvils toward a central cubic volume which produces quasi-hydrostatic pressure at the centre of the cubic pressure cell. Both presses were previously pressure-calibrated at room and high temperatures. Calibrations of the 200 ton press carried out during this study were based on known standard phase transitions in Bi I-II (2.54 GPa), TI I-III (3.7 GPa) and Ba I-II (5.5 GPa) which were determined by observing an abrupt change in their electrical resistance or equivalently in voltage drop across the samples as shown in Figure 2.2. These calibration experiments were repeated for different cycles. However, the best fitted polynomial curve to the first cycle results was considered as the calibration plot as shown in Figure2.3. Voltage drop across the sample was measured with a Solarton 7061 voltmeter while an Agilent E3632A DC power supply provided a constant current across the sample.

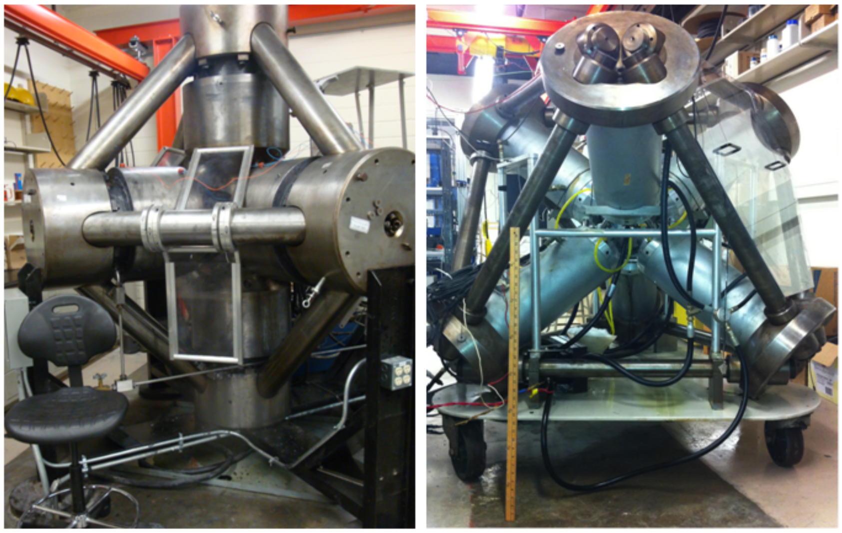

Figure 2.1 1000 ton (left) and 200 ton (right) presses .

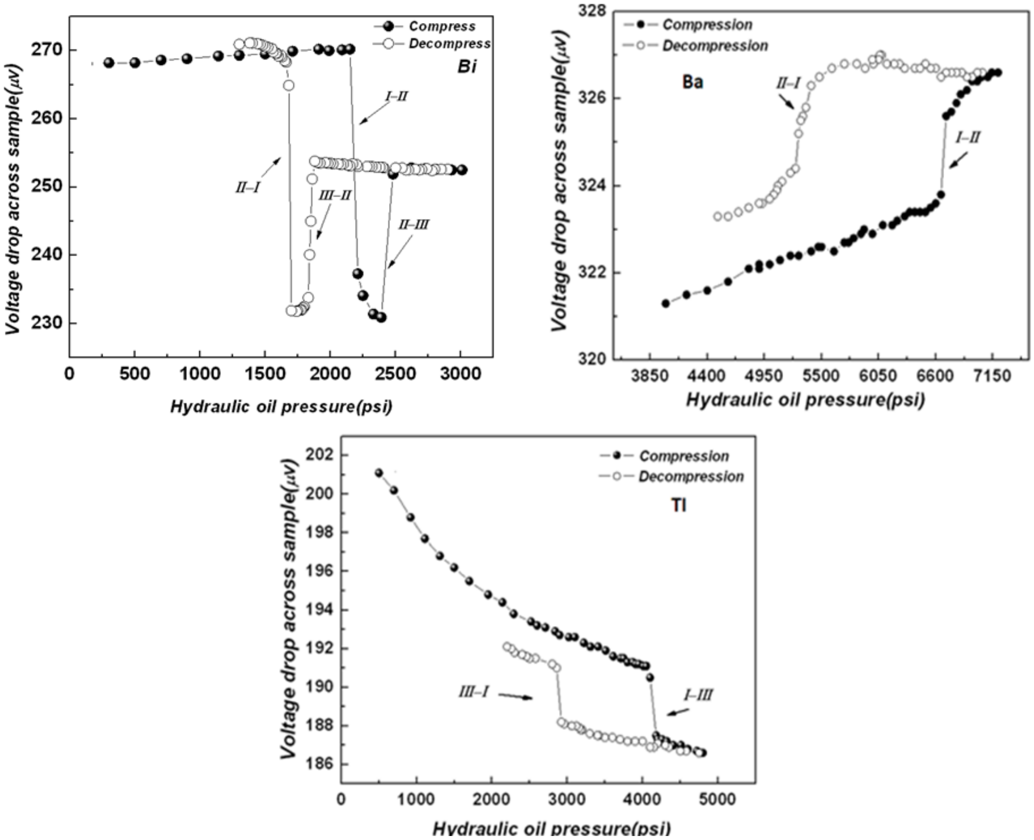

Figure 2.2 Typical plots of voltage drop versus hydraulic oil for three calibrants in runs for pressure calibration of the 200 ton press.

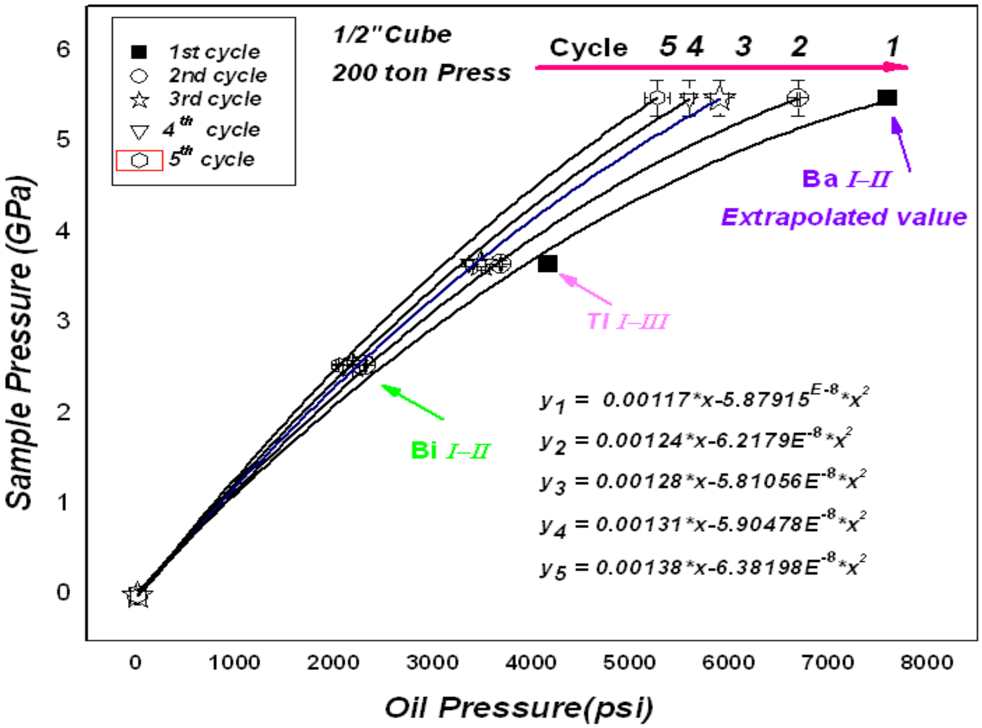

Figure 2.3 Room pressure calibration for 200 ton press.

2.2 General features of pressure cell design

Formation of gaskets on the oversized pyrophyllite ($Al_4Si_8O_{20}OH_4$) pressure cell cube maintains high quasi-hydrostatic pressure within the center of the pyrophyllite in which a boron nitride (BN) capsule encloses the sample. Thermally insulating zirconia (ZrO_2) sleeves were employed in addition to two ZrO_2 disks placed on top and bottom of the BN capsule. Temperature was recorded via an S-type (Pt/Pt-10% Rh) thermocouple passing through the BN wall. The thermocouple was electrically isolated from the furnace by alumina (Al_2O_3) ceramic sheaths. Pressure correction for the thermo-emf values was applied (Bundy, 1961). All above mentioned features were commonly shared with high pressure cell designs (Figure 2.4) in the 200 and 1000 ton presses in the current research.

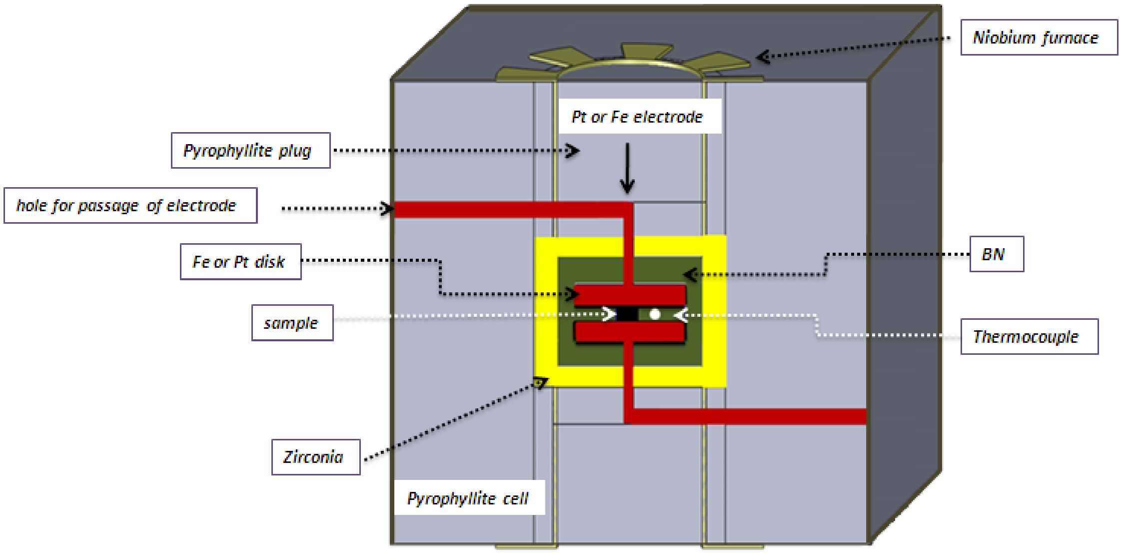

Figure 2.4 Schematic illustration of the basic cell design in the 200 and the 1000 ton presses.

2.2.1 Heating system

Two main heating systems were employed:

1. External heating which arises mostly from ohmic heating when currents up to 370A from a Mathis LV750 low voltage AC power supply are passed through a cylindrical Nb foil furnace of 0.005" thickness, surrounding the sample.
2. Self heating system, in which a varying current up to 218A from the 10KW EMS DC power supply, passes through the sample and produces the required heat.

2.2.2 Data acquisition methods

Experiments carried out in the 200 ton press were not computer-controlled, whereas those performed in the 1000 ton press had a precise and simultaneous record of heating rate, time, voltage and current which will be discussed in the following chapter. Data acquisitions of thermocouple emf and voltage drop across the sample were accomplished via a Solarton 7061 voltmeter in the 200 ton press experiments while an Agilent E3632A DC power supply provided a constant current across the sample. In the 1000 ton press experiments, an Agilent 34970A multimeter with several channels was employed for simultaneously recording the current passing through the sample, corresponding voltage drop across the sample and the current passing through the Nb furnace from the Mathis LV750 low voltage AC power supply.

2.2.3 Electrode material and configurations

Investigating electrical resistivities typically of the order of 10^{-7} to 10^{-6} Ωm (solid phase) for pure Fe and also Fe-Si alloys with small percentage variation at the phase transition to the liquid phase, under high P,T condition is a serious challenge from several perspectives. One of the most challenging issues is isolating the electrical resistivity of the sample from the rest of the circuit components which is of critical importance. Most of the inner cell components are electrical insulators (e.g. BN, ZrO_2 and pyrophyllite). Therefore, the main part of measurement errors imposed on the final data stems from the electrode material which is attached to the sample. These circuit elements play a key role in affecting the recorded electrical resistivity data and bring about masking the real electrical resistivity changes of the sample under investigation. Resolving this problem by choosing the right electrode material and knowing its electrical resistivity, the electrode geometry and also the way the electrodes are connected to the sample has been taken in to account. As the aim of this study is to investigate the electrical resistivity of Fe17Si within the liquid phase at high pressure, the melting temperature of the electrode compared to the sample (Fe, Fe-Si alloy) also should be considered as a critical feature. Among the three major methods of connecting electrical leads to a sample, “welding”, “mechanical contact” and “atomic contact”, the last two ways have been tried for Fe-Si sample and for pure Fe respectively. The last method is considered as the best option. Also, as the pressure will guarantee a secure contact with the sample and the electrode, "mechanical contact" is the second preferred option which benefits from avoiding the risk of oxidation of the "welding method". Among tested materials in high P, T experiments, pure Fe wire and also Pt are considered standard materials having dual functionality as current and potential leads. Figure 2.5 illustrates typical electrode configurations that have been used for experiments.

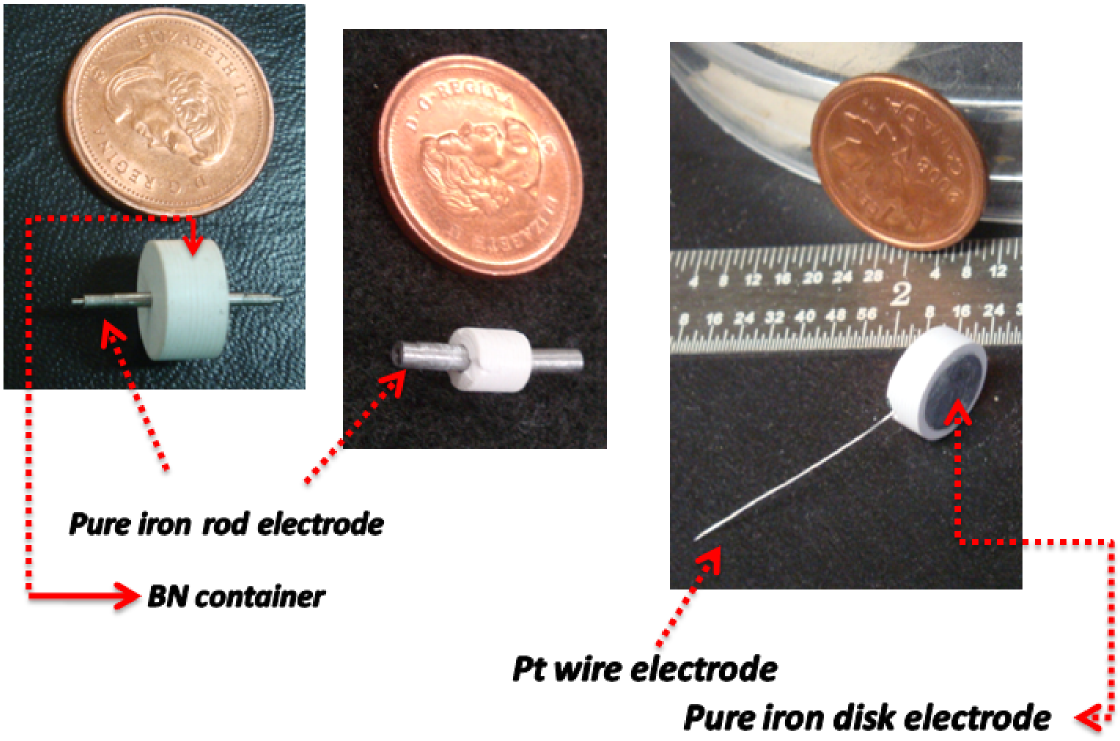

Figure 2.5 The variety of electrode configurations tested in this study.

2.3 Resistance measurement

2.3.1 Two wire method

In some experiments carried out in the 1000 ton press with Fe17Si samples, electrical resistance was directly recorded by a resistance meter. Therefore, only two wires were utilized to measure electrical resistance of the circuit which not only records the resistance of the sample in the centre of the cube but also includes the additional resistance from all other electrodes, wirings from the anvils to the resistance meter and also the possible internal resistance of the meter (Figure 2.6). However, considering the difficulty in separating these contributions to the overall resistance of the circuit, the 2-wire method is not a favored method for pure Fe or Fe-Si alloys. Therefore, another type of resistance measurement, called the 4-wire method, was tried.

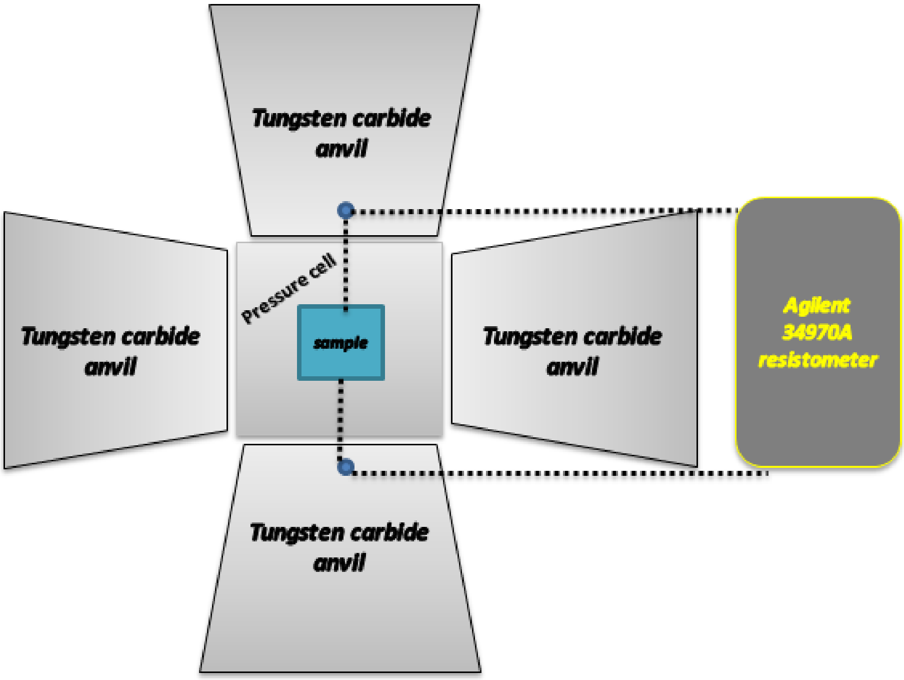

Figure 2.6 Schematic illustration of 2-wire resistance method.

2.3.2 Four wire method

Except for those Fe17Si experiments carried out in the 1000 ton press which employed the 2-wire method, the rest of experiments in the 200 ton and 1000 ton presses employed a 4-wire method, Type A or B. In Type A, the sample is not directly connected to the current source and to the voltmeter but, one set of wires connecting through the cell to the sample, serves as both current and voltage lead as shown in Figure 2.7a. This electrical path is split into two different paths immediately after it exits the sample. It should be emphasized that this method is not a true 4-wire method and should be modified according to Type B as shown in Figure 2.7b. In Type B of the four wire method, the current and voltage drop leads are each a separate set of wires starting from the sample in the centre of the cell. This method is the ideal one, as it will eliminate the voltage drop contribution originating from the circuit components other than the sample. This specific four-wire method was tried with an H-shape sample for pure Fe which will be explained later in Chapter 4.

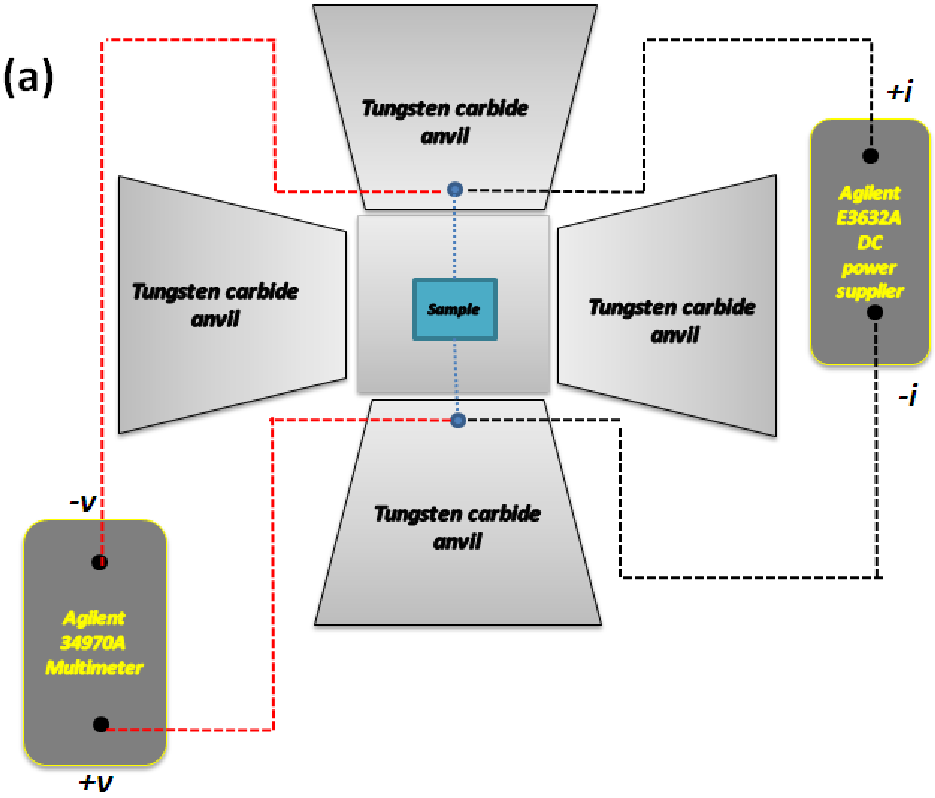

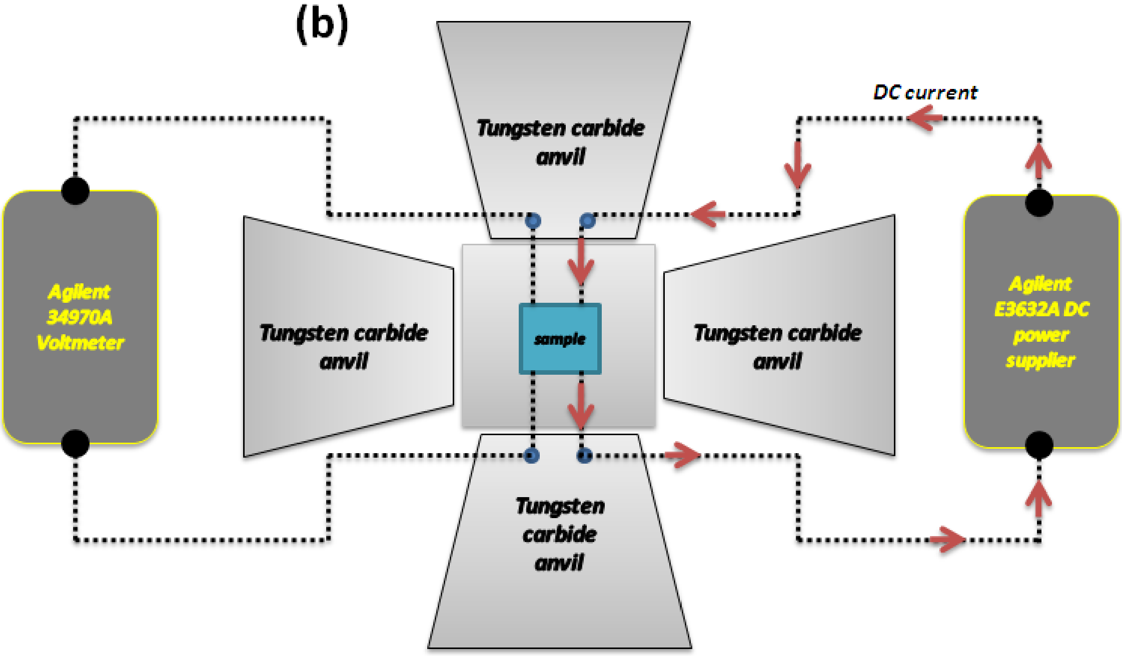

Figure 2.7 Schematic illustration of 4-wire method a) Type A, b) Type B.

CHAPTER 3

3 Solid pure Fe electrical resistivity at high pressure and temperature

Pressure and temperature can result in structural phase transitions as well as affecting band structure and magnetic interaction in transition metals including pure Fe. Electrical resistivity is a striking manifestation of these crystal structure and band structure alterations which can be tracked as a slope change in resistivity versus pressure or temperature plots. The electrical resistivities of most metals increase approximately linearly with temperature and decrease with pressure so that for an “ideal” metal, resistivity along the melting curve is proposed to be constant (Stacey and Anderson, 2001). However, being a ferromagnetic transition metal at ambient condition, with a partially filled d band ($3d^6 4s^2$), the resistivity behavior of Fe is more complicated than simple metals such as copper under the effect of temperature and pressure. In an electronically simple metal such as copper, all conduction electrons are of the same type, while Fe has two types of electron states, s and d electrons, which contribute to conduction in different ways. 3d electrons have much higher density of states (DOS) at the Fermi level than 4s electrons. However, being more tightly bound and much less mobile than 4s electrons, 3d electrons have less contribution in conduction compared to

4s electrons. The conduction electrons can be scattered by three major mechanisms: phonons (lattice vibrations): ρ_{ph} , magnons (spin disorder waves): $\rho_{magnetic}$ and by an interband s-d scattering mechanism (where s electrons are scattered into the d-band): $\rho_{s\text{-}d}$. These effects can be described as interacting under Matthiessen's rule:

$$\rho = \rho_{ph} + \rho_{s-d} + \rho_{magnetic} \tag{3.1}$$

Temperature and pressure will each have their specific influence on each of these contributions which is discussed separately in the following.

3.1 Temperature effect

Below the Curie temperature, T_C , resistivity variation with temperature exhibits a non-linear relation due to T^2 dependence of ρ_{mag} while the other resistivity components have a linear dependence on temperature. Well above Tc, it is usually assumed that ρ_{mag} is almost fixed at the value of 8×10^{-7} Ωm at high temperatures and resistivity follows the normal pattern of approximate proportionality to temperature (Weiss and Marotta, 1959). However, within the high temperature region, growth of resistivity of pure Fe and its alloys is believed not to continue indefinitely with temperature but rather show a "saturation" trend. This thermally- induced "saturation" characteristic does not apply only to Fe but to most metallic systems, particularly transition metals and their compounds (Mooij, 1973; Fisk and Webb, 1976; Allen, 1980; Gunnarsson et al., 2003). The saturation is suggested to happen when the thermally reduced mean free-path of conduction electrons becomes comparable to the interatomic spacing which is so-called Ioffe-Regel criterion. Following that, $\rho(T)$ approaches a constant value within the range of approximately$1\times10^{-6} – 2\times10^{-6}$ Ωm(Gunnarsson et al., 2003). This is the case of pure Fe in its γ phase where it appears to saturate at a value of 1.68×10^{-6} Ωm (Bohnenkamp et al., 2002). The mechanism responsible for saturation phenomena and also the universality of its value for metallic systems are the subject of debate. However, the temperature dependence of resistivity seems to follow a simple parallel-resistor formula (Wiesmann et al. 1977):

$$\frac{1}{\rho(T)} = \frac{1}{\rho(T)_{ideal}} + \frac{1}{\rho_{sat}} \tag{3.2}$$

where, $\rho(T)$ is the total resistivity, ρ_{ideal} is the ideal resistivity that would be expected in the absence of saturation and is given by “Matthiessen’s rule” and ρ_{sat} is the maximum resistivity at saturation.

3.2 Pressure effect

Applying hydrostatic pressure affects the interatomic distances and potentials, which may consequently alter the band structure and magnetic interactions in transition metals. The influence of pressure on each of the separate electrical resistivity mechanisms, and consequently on the total electrical resistivity of Fe, is not as well understood as the influence of temperature and there is no exact expression that explains the pressure dependence of each scattering agent in equation 3.1 (Yousouf et al., 1986). However, as a common feature for electrical resistivity of metals it is known that electrical resistivity decreases as pressure increases due to the damping effect of pressure on the amplitude of atomic vibrations which reduces phonon resistivity (ρ_{ph}). The effect of pressure on the band structure is more complicated than on phonons when it comes to a half-filled d orbital metal such as Fe, since conduction 4s and 3d electrons are not contributing to conduction in the same manner under the effect of pressure. There is a common agreement that an increase in pressure broadens the d-band and thus lowers its density of states, (Kmetko, 1971; Boness and Brown, 1986). It follows that s-d scattering must also decrease. On the other hand, in Fe the 4s states, which dominate conduction, are spread much more in energy than the 3d states and the effective number of conduction electrons decreases faster with pressure than the number of d-states into which they can be scattered. It follows that pressure increases the resistivity of Fe more than it does for metals such as copper (Stacey and Loper, 2007). However, still there is a need to have accurate theoretical relationships that describe the T and P-induced variation of DOS for both d and s electrons. The effect of pressure on ρ_{mag} is considered to be small, as experiments up to 9 GPa do not show a significant shift of Curie temperature with pressure variation (Leger et al., 1972). Pressure induced d-band broadening is suggested to be the main mechanism for magnetism suppression in Fe which finally yields a magnetic transition that precedes the structural bcc-hcp transition between 12-18 GPa at room temperature (Lota et al., 2007). At the bcc-hcp transition, the electrical resistivity undergoes a jump as a function of pressure (Sha and Cohen, 2011). Following the bcc-hcp jump, resistivity diminishes gradually. From the other perspective, it is argued that as the pressure reduces interatomic distances, electrical resistivity saturation discussed in the previous section is linked to pressure with the following equation:

$$\frac{1}{\rho(T,V)_{total}}=\frac{1}{\rho(T,V)_{ideal}}+\frac{1}{\rho(V)_{sat}} \tag{3.3}$$

where V stands for volume (Gomi et al., 2013). High pressure diamond anvil cell (DAC) experiments of pure Fe up to 100 GPa by Gomi et al. (2013), confirms the saturation dependency on pressure for electrical resistivities that can have an implication for the electrical and thermal conductivity of the Earth’s core and will be later discussed.

3.3 Pure Fe electrical resistivity under the Earth's core condition

Linking the behavior of electrical resistivity of Fe to the Earth's core is possible if its electrical resistivity is investigated in the liquid state under the combined effects of high P, T condition. In spite of some number of studies of electrical resistivity of pure Fe in the liquid state at room pressure (Powell, 1953; Regel and Mokrovski (values reported by Cusack, 1963); Baum et al., 1967; Van Zytveld, 1980), the number of experimental studies on the electrical resistivity of liquid Fe under high P, T is scarce (Yousouf et al., 1986; Secco and Schloessin, 1989; Deng et al. 2013). However, attempts on thermodynamic calculations, and band structure simulations have been successful in investigating the electronic properties of liquid Fe under high P, T conditions. From thermodynamic calculations of Boness and Brown (1986), it follows that the density of states at the Fermi level for liquid Fe does not differ much from that calculated for pure crystalline Fe. Therefore, it suggests that the behavior of electrical resistivity of pure Fe cannot be dramatically different from the preceding solid phase which allows the solid phase electrical resistivity of pure Fe to provide guidance about its liquid phase electrical resistivity. Considering the effect of high pressure, band structure calculations by Elsasser and Isenberg (1949) put forward an extreme case of the pressure induced electronic transition phenomenon for pressures as high as the Earth's core. They suggested that electronic configuration of liquid Fe under core pressure might undergo a transition from $3d^7$ $4s^1$ to the $3d^8$ state. Therefore, the emptying of the s band leads to a large increase of the core resistivity due to low mobility of d electrons. This conclusion prompted several theoretical studies on bcc, fcc and hcp band structure of solid pure Fe under high pressures (Kmetko, 1971; Bukowinski, 1976 and Boness and Brown, 1986). It was proved that basic form of the DOS function exhibits invariance apart from the expected energy broadening and DOS reduction under core pressure conditions. Therefore, electronic transition will not occur up to a four-fold compression. It implies a similarity in electronic behavior of Fe at outer core conditions and that of observed experimental values at lower P, T conditions. These considerations, give more confidence to the application of laboratory P, T electrical resistivity values to core conditions. However, because the band structure of pure Fe is not fully understood under the combined effect of pressure and temperature, extrapolations are still challenging. Stacey and Anderson (2001) employed the high pressure electrical resistivity measurements of Bridgman (1957) and Matassov (1977) on pure Fe and Fe alloys and suggested the invariance of the electrical resistivity of pure Fe on the melting boundary which made the extrapolations to the core condition easier. However, later, Stacey and Loper (2007) argued that differences in the pressure response of s and d electrons were not accounted for in Stacey and Anderson (2001). They revised the electrical resistivities of pure Fe reported in Stacey and Anderson (2001) by suggesting that the DOS of s electrons is affected more strongly than the DOS of d electrons by the effect of pressure. Therefore, DOS of s electrons will reduce more under high pressure than that of d electrons which resulted in greater estimated value of electrical resistivity of Fe at core conditions. On the other hand, very recent first principle calculations (de Koker et al., 2012; Pozzo et al., 2012; Pozzo et al., 2013), suggest a different picture of the electrical resistivity magnitude under the Earth’s core P, T condition. They calculated the electrical resistivity of the Earth’s core to be 2-3 times lower than the estimates of Stacey and Loper (2007). According to Gomi et al. (2013) and Hirose et al. (2013), electrical resistivity saturation is proposed to be the key factor that can provide a reasonable explanation for the very recent Earth's core electrical resistivity estimations and propose a different picture of the Earth's electrical resistivity behavior.

CHAPTER 4

4 Pure Fe experiments

4.1 Full cube design experiments in 200 ton press

For pure Fe resistivity measurements in the 200 ton press, a traditional “full cube design” was employed with the general features being the same as explained in Chapter 2. A “full cube design” means that holes are drilled into a full cube of pyrophyllite and components are inserted in the holes on assembly of the cell. Figure 4.1 shows a cross-sectioned view of a full cube design (Figure 4.1a) and a photo of the recovered (i.e. post experiment) and sectioned region containing the sample and electrodes (Figure 4.1b).

4.1.1 Resistance measurements

To measure the electrical resistivity, a constant current of 100 mA was passed through the Fe wire sample which was obtained from ESPI Metals Company (99.999% purity and diameter of 0.005”). The voltage drop across the sample was recorded by a Solarton 7061 voltmeter. A Pt electrode was used as it is a malleable material and easy to make a disk shape end.

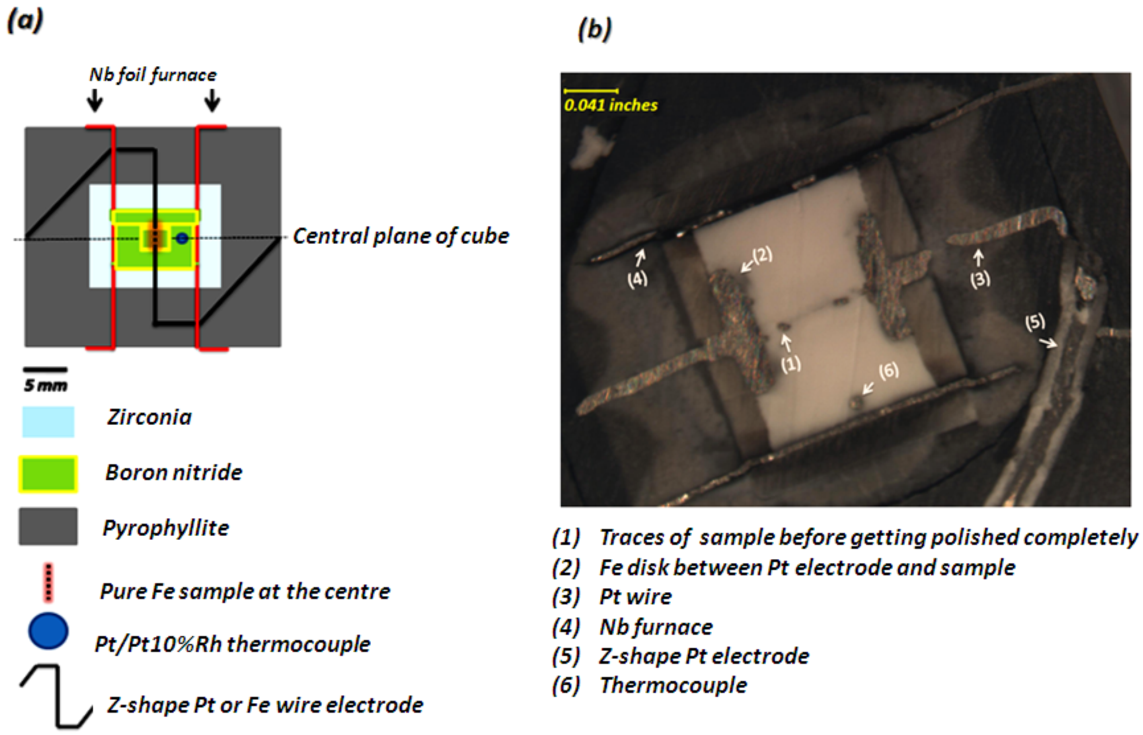

Figure 4.1 (a) Schematic cell design in the 200 ton press for pure Fe sample, (b) a section view of the quenched cell.

Electrodes had dual functionality as current and a potential lead in the two- wire method. The thermocouple emf was also recorded with the same voltmeter using a different channel. By calculating the resistance and measuring the geometry of the sectioned sample under the microscope, as shown in Figure 4.1b, the electrical resistivity was calculated as follows:

$$\rho = R \times A / L \tag{4.1}$$

where

$$R = V/I \tag{4.2}$$

and, A is the cross sectional area and L the length of the quenched sample, V and I are the measured voltage drop across and constant current through the sample. All experiments were pressurized first to a fixed pressure of 2 GPa and then heated through melting. The goal of each experiment was to traverse the melting point so that measurements of the resistivity could be made in the liquid state. However, it should be noted that for this group of experiments, data acquisition for all quantities: thermocouple emf, current, voltage drop across the sample, furnace current and furnace power, were not synchronized as they were separately and sequentially read and manually recorded from the voltmeter screen.

4.2 Results for 200 ton press experiments

The phase diagram of pure Fe shown in Figure 4.2 is used to identify the probable P, T-induced phase changes.

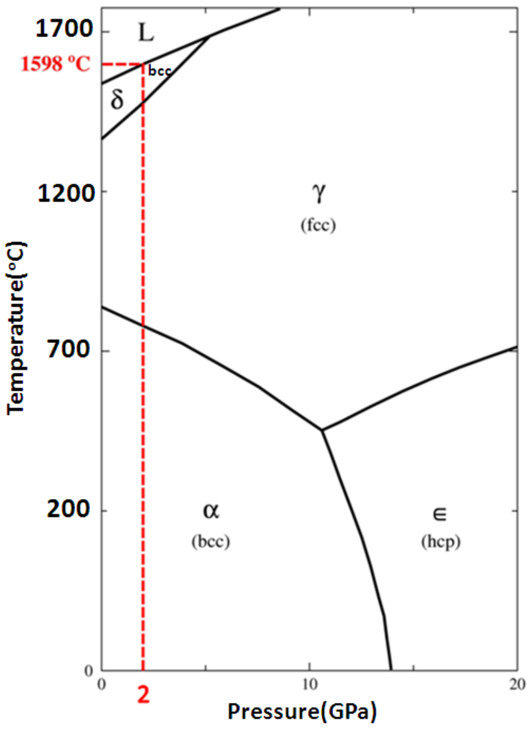

Figure 4.2 Pressure–temperature phase diagram of pure Fe (after Anderson, 1986). The red dashed line indicates 2 GPa melting temperature

Resistivity versus temperature plots of three selected experiments; I21, I22 and I23 are illustrated in Figure 4.3 with a comparison to data by Secco and Schloessin (1989).

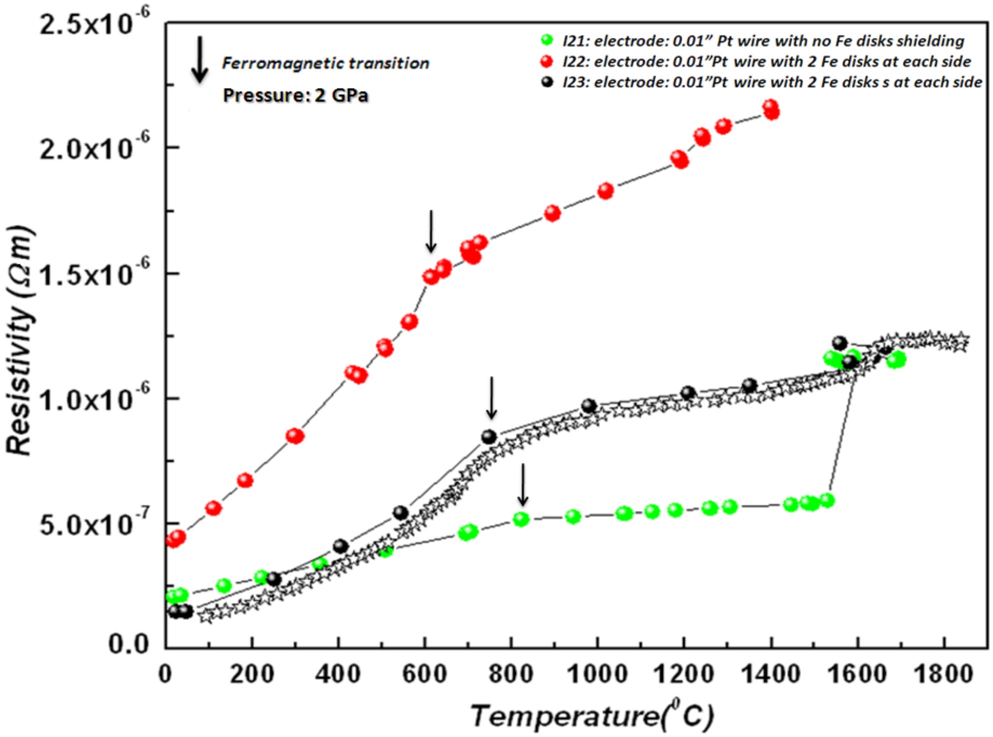

Figure 4.3 Temperature dependence of electrical resistivity for pure Fe in the 200 ton press along with Secco and Schloessin (1989) data at 2.48 GPa, shown by stars.

The notation I indicates Fe is the sample, 2 is representative of experiments carried out in 200 ton press and n (1:3) is the sequential number of the experiment. The I21 run, exhibits an extraordinarily big jump in resistivity at the melting transition ($\rho_{liquid}/\rho_{solid}$=1.89) which is inconsistent with the rest of results at the solid-liquid transition and the source of problem could not be identified. In I22, due to the loss of electrode prior to the melting temperature of Fe, the experiment could not record the melting transition. The I23 run appeared to be a successful run and exhibits a much better agreement with the reported trend from Secco and Schloessin (1989). In all three cases, the magnetic transition (ferromagnetic to paramagnetic) is very obvious.

4.2.1 Chemical contamination

As data acquisition was not automatic, there are no quantitative data on the heating rates. Also, electron microprobe analysis was not done for this series of experiments. However, comparing the experimental condition with future experiments within the present work (Figure 6.26) it can be claimed that heating was definitely not as fast as short duration experiments. On the other hand, in Figure 4.3, I21 is the only run with a direct contact with Pt wire and the rest have Fe disk (0.004" thick) shielding against a direct contact with Pt electrode. Therefore, specifically for the first unprotected experiment (I21), the chance of interdiffusion of Fe and Pt together cannot be ignored. As a distinctive feature of I21, the order of resistivity appears to be the lowest among all (Figure 4.3). Nevertheless, I22 and I23, which had the same number of Fe disks shielding (two at each side) and with an approximately the same prolonged heating duration, do not share an identical electrical resistivity order of magnitude. Therefore, no conclusive information can be obtained by solely comparing possibly low-contaminated (I22 and I23) runs with I21 on the grounds of chemical contamination. It is of interest to note that I21 liquid data points coincide very well with the δ region as well as the melting boundary of Secco and Schloessin (1989) and also with I23 liquid points. Examining the electrical resistivity of Pt at room pressure by Van Zytveld (1980), the ratio $\rho_{liquid}/\rho_{solid}$ is approximately 1.38 compared to that of pure Fe, which is approximately 1.08, as shown in Figure 4.4.

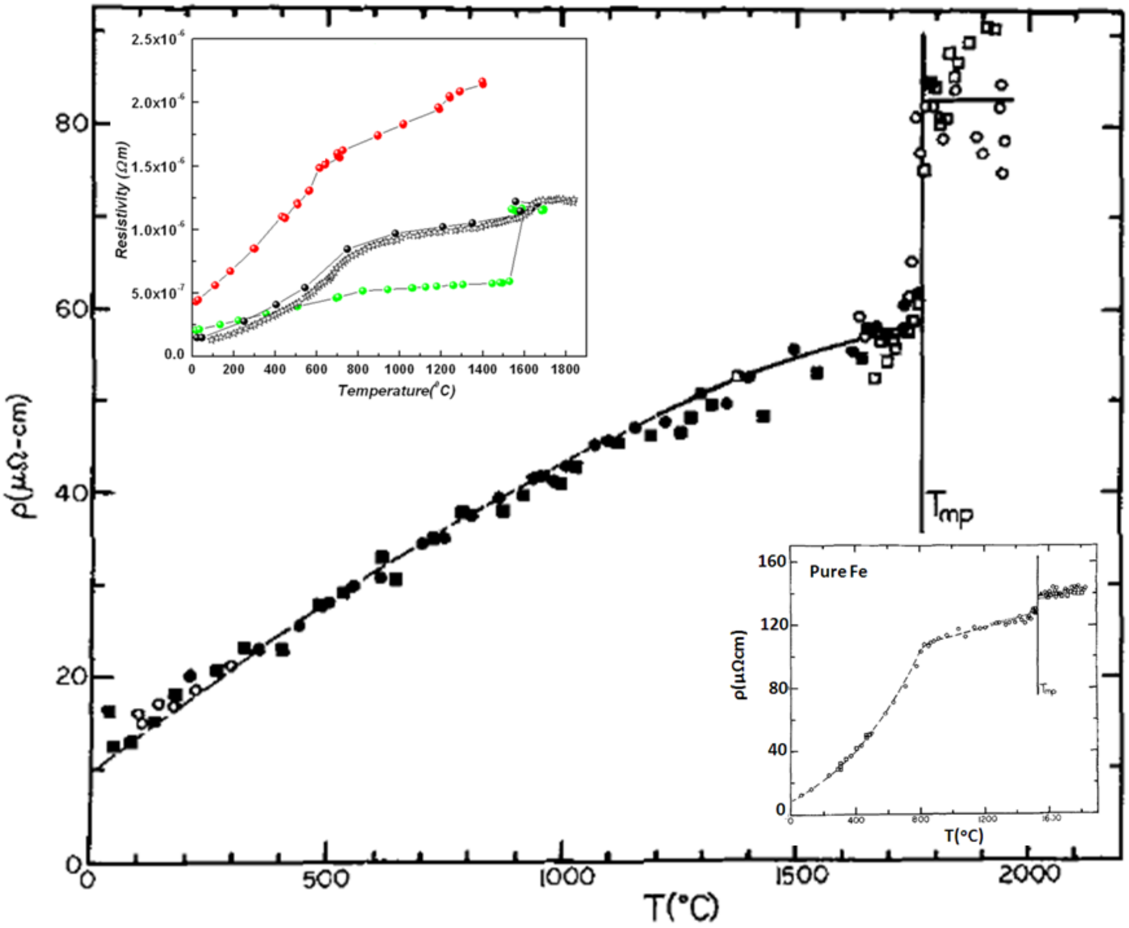

Figure 4.4 Temperature dependence of Pt from Van Zytveld (1980). The upper insert is the data for pure Fe from the present study and the lower insert is data for pure Fe from van Zytveld (1980).

Also considering the phase diagram of Fe-Pt at room pressure as shown in Figure 4.5, the melting temperature of the alloy is lower than Fe up to around 45wt%Pt. The phase diagram in Figure 4.5 also indicates the magnetic transformation drops as the wt%Pt increases. Having all the above-mentioned information, the amount of jump at the melting transition in I21, is much higher than the expected variation specific to pure Fe and more identical to Pt melting transition electrical resistivity characteristics. Also,

Figure 4.3 suggests that the magnitude of electrical resistivity values for I21 has more similarity to pure Pt and smaller than I22 and I23 values.

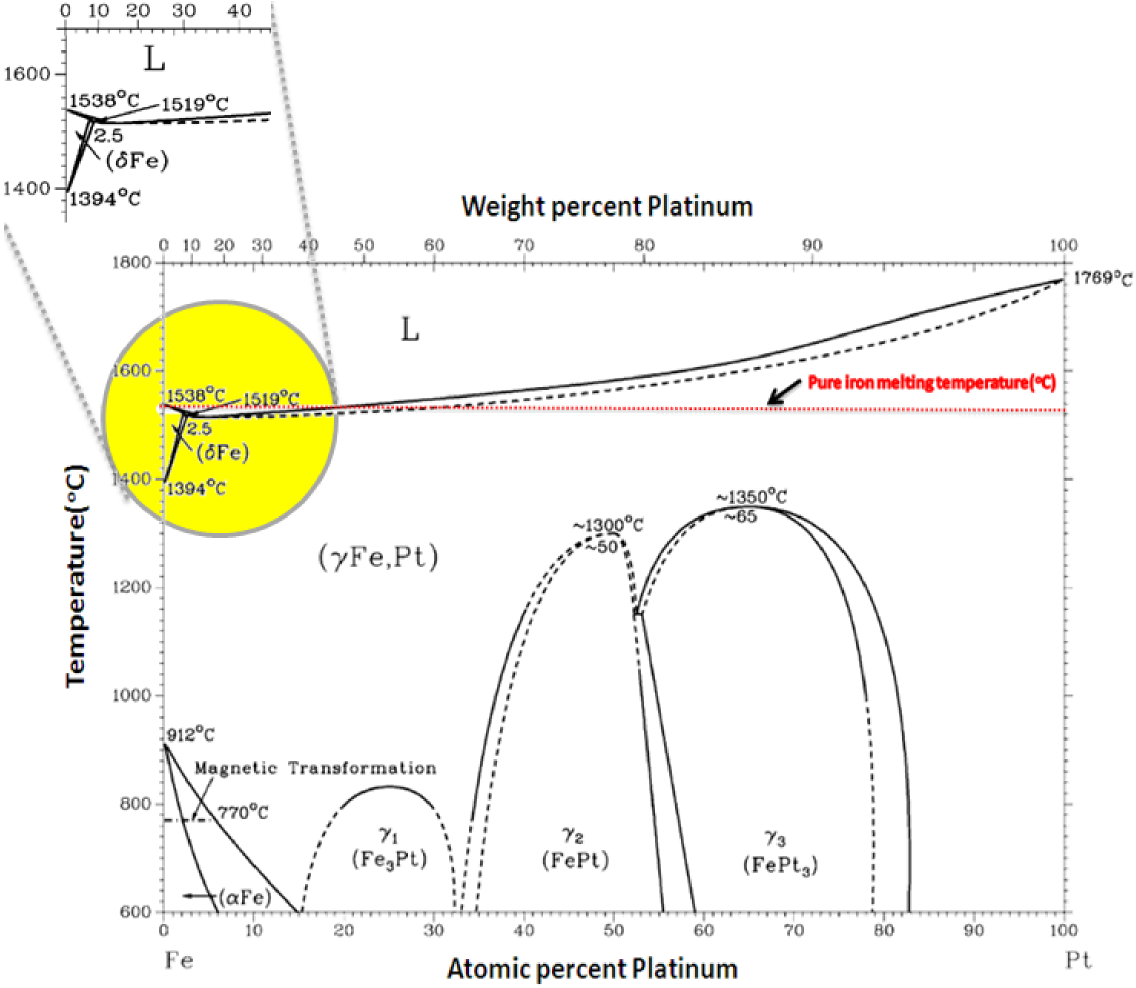

Figure 4.5 Phase diagram of Fe-Pt alloy (after Massalsky, 1996).

Having a closer inspection of Figure 4.5, suggests that the transition temperature in I21 resembles the $Fe_3Pt(\gamma_1)$ to $FePt(\gamma)$ phase at ~800°C corresponding to 50-60 wt%. Therefore, the kink around 800°C cannot be associated with magnetic transition but the phase transition in Fe-Pt system. In terms of melting temperature, both I21 and I22 exhibit lower values than I23, which can be regarded as a sign of contamination. However, it does not provide any indication of the possible amount of Pt contamination.

Based on the clues provided by melting temperature comparison, and also by the amount of jump at the melting transition, it is suggested that, I21 has more contamination than the rest of the series.

4.2.2 Electrical contribution from the circuit

Looking at the electrical resistivity results from another perspective, it should be noted that, with the same sample diameter of 0.05” in comparison to the Pt wires of 0.01”thickness; the shorter length of Pt electrode within the I21 cell yields a smaller magnitude for resistivity values compared to the I22 cell with the longer Pt wire. Comparing with the data of Secco and Schloessin (1989) data at 2.48 GPa, the only consistent resistivity result is the I23 cell with an Fe sample being three times as long as that of I21 and I22. In other words, it appears that elongating the length of Fe wire at the expense of the length of Pt remarkably improves the order and behavior of electrical resistivity of pure Fe. The difference in pressures between I23 and the experiment of Secco and Schloessin (1989) can account for the slightly higher resistivity of I23 since $(d\rho/dP)_T < 0$ and the pressure for I23 experiment was lower than their experiment. Therefore, the geometrical configuration of the experiments can yield a very significant resistance contribution from the electrodes in a 2-wire experiment. In I21 and I22 cells, the length of the sample is just a small proportion of the whole cell length which is 24% for I21 and 14% for I22 whereas for I23 it amounts to 68%. Therefore, if one considers the electrical resistivity of Pt and Fe to be almost identical at room P, T condition (ρ_{Pt} =105 nΩm and ρ_{Fe} =100 nΩm) (Van Zytveld, 1980), and if the thermal gradient within the hot zone is ignored (vertical offset along the central axis leads to a temperature difference of ~ 100 °C at most); a G-factor, indicating the relative resistance contribution of Pt and Fe, can be defined at room temperature as:

$$G_{electrode} = L_{electrode} / A_{electrode} = R_{electrode}/\rho_{electrode} \quad (4.3)$$

$$G_{sample} = L_{sample} / A_{sample} = R_{sample}/\rho_{sample} \quad (4.4)$$

$$G = G_{electrode} / G_{sample} = R_{electrode}/R_{sample} \times \underbrace{\rho_{sample}/ \rho_{electrode}}_{\textbf{\textit{Constant}}} \quad (4.5)$$

where, *L* stands for length and *A* for the cross section area.

A value of G>1 indicates that the resistance of the electrode dominates over the resistance of the sample. The results summarized in Table 4.1 give a clear indication that Pt electrode has at least as much contribution in the electrical resistivity as the Fe sample and has a dominant role in I22.

Table 4.1 Main characteristics of pure Fe experiments in 200 ton press

Exp.	G factor (22 ^{o}C)	Room T resistivity ($10^{-7}\Omega$m)	Melting T (^{o}C)	Resistivity at melting ($10^{-6}\Omega$m)	R_{liquid}/R_{solid}
I21	0.79	2.01	1563± 34	1.15	1.9
I22	1.5	4.3	N/A	2.2*	N/A
I23	0.3	1.5	1605±28	1.17	1.09

* Resistivity at highest temperature reached (1400^{o}C) but melting not observed.

4.2.3 Circuit against chemical contamination

Comparing results from Figure 4.3 and Table 4.1, circuit geometry is the dominant effect at least for low temperature values. I21 is likely to have the highest chemical contamination among all, while its G-factor lies between the two others. Although the Pt contamination may reduce the electrical resistivity values because of the lower resistivity of Pt compared to Fe, the G-factor of I21 is not the lowest among all. I22 and I23 are likely to have the same amount of chemical contamination because of the same number of Fe disk shielding, with I22 having the largest G-factor among all and the highest value of resistivity as well. With I22 and I23 likely having similar degrees of contamination, G-factor can clearly explain the higher electrical resistivity of I22 compared to I23 because of its higher G-factor value. Therefore, even with a low heating rate which can make the sample vulnerable to the chemical reaction with the electrode leads, I23 exhibits acceptable electrical resistivity values. One can conclude that, the relative length and diameter of the sample compared to the rest of conductive part of the electrical circuit inside and outside of the cell is of critical importance for a cell with pure Fe sample and Pt electrode. This fact urges a measuring method that can reduce or completely rule out the effect of electrode contribution to the resistivity measurements as much as possible.

4.3 1000 ton press experiments: H-shape design

Experiments that were performed in the 200 ton press all used the two-wire method for measuring electrical resistances. However, taking into account the two major sources of error in the 200 ton experiments as being possible chemical contamination and more importantly, circuit electrical resistance contribution, there was a serious need to develop a four-wire method design and investigate the possible differences. Therefore an H-shape design was developed for the first time. An H-shape of continuous pure Fe was fabricated out of a bulk Fe rod as shown in Figure 4.6. One continuous H-shape piece of pure Fe serves three simultaneous functions of being the sample, the heater in the center part (self heating system), and also potential and current leads. A significant advantage of this design is that sample, current, and potential leads all have “atomic attachment” to one another.

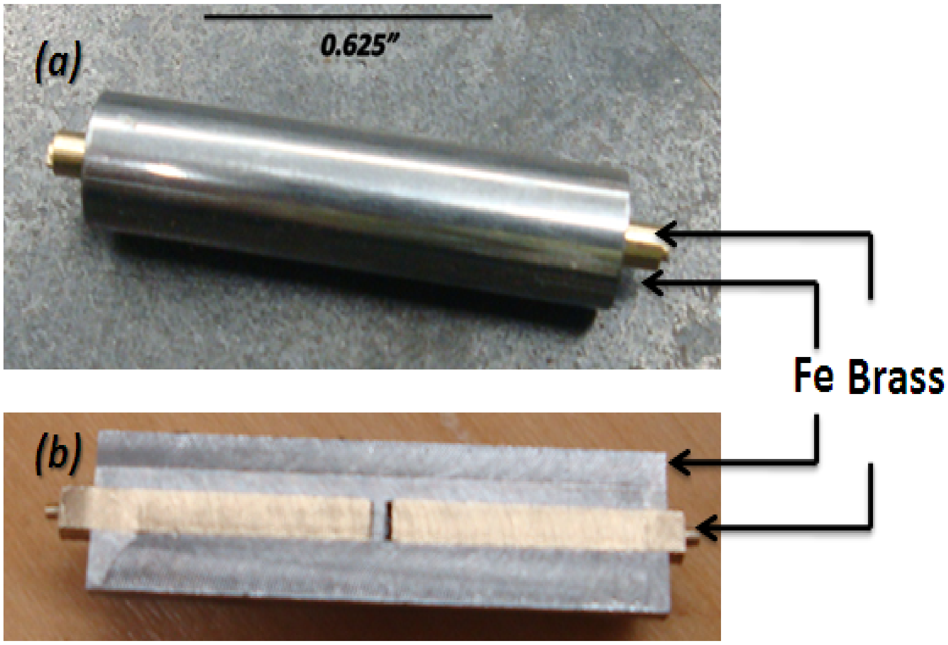

Figure 4.6 (a) starting Fe rod material with rod inserts made of brass; (b) machined H-shape Fe piece out of the initial rod. An axial hole was drilled in the Fe rod and filled with a brass rod in order to facilitate machining of the H-shaped Fe.

As illustrated in Figure 4.7, H-shape Fe is enclosed by a BN capsule. The pressure transmitting medium is pyrophyllite and the current lead, for both the self-heating Fe sample as well as for measuring Fe resistance, is a graphite bar which is attached to Fe leads. The DC current which passes through the sample provides a self-heating system and is sufficient to melt the sample. The current, corresponding voltage drop and the thermocouple emf values were all recorded simultaneously by Agilent 34972A digital voltmeter on 3 separate channels. The thermocouple was an S-type (Pt/Pt-10% Rh) inserted perpendicular to the central plane of the half cell but with a lateral offset of ~ 0.03" from the sample. Employing two-half pyrophyllite cubes gives greater assurance of having a perfect contact between the graphite and Fe current leads.

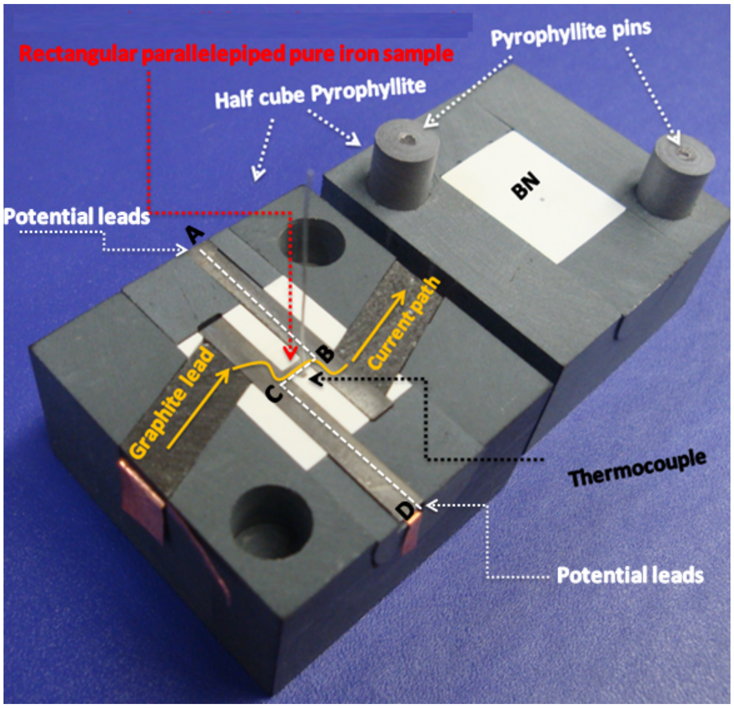

Figure 4.7 Plan view of H-shape cell; Potential leads are Fe sections A-B and C-D which measure potential drop across sample between C and D. The edge length of each half cube is 1.25”.

Also, H-shape design makes it much more convenient for creating more sophisticated designs inside each half cube pyrophyllite. Ideal current, potential lead connection devoid of common problems existing in traditional design provides a unique chance to obtain high resolution electrical resistivity data in which, recorded voltage drop across the sample can be safely considered to originate solely from the sample. As illustrated in Figure 4.7, the voltage drop is measured across the sample BC with potential leads AB and CD. As the design developed, the location of the thermocouple was moved closer to the sample from the initial 0.05” to 0.03”. Within several test experiments, an optimum geometry for the graphite and current leads was obtained in order to avoid any hot spot by passage of current.

4.3.1 Experimental results

Electrical resistivity of pure Fe is plotted in Figure 4.8 at a fixed pressure of 2.27 GPa. The transition temperatures in H-shape design are much lower than expected from the P, T phase diagram of Fe shown in Figure 4.2. This is primarily due to the significant thermal gradient within the cell specific to the internal self-heating systems (H-shape or conical design: Secco and Schloessin (1989)). Thermocouple positioning can lead to additional difference between recorded temperature and the actual temperature of the sample. However, the thermocouple was placed as close as possible to the sample area (within 0.03” distance) which is closer than the traditional full cube design (0.07” offset from the sample).

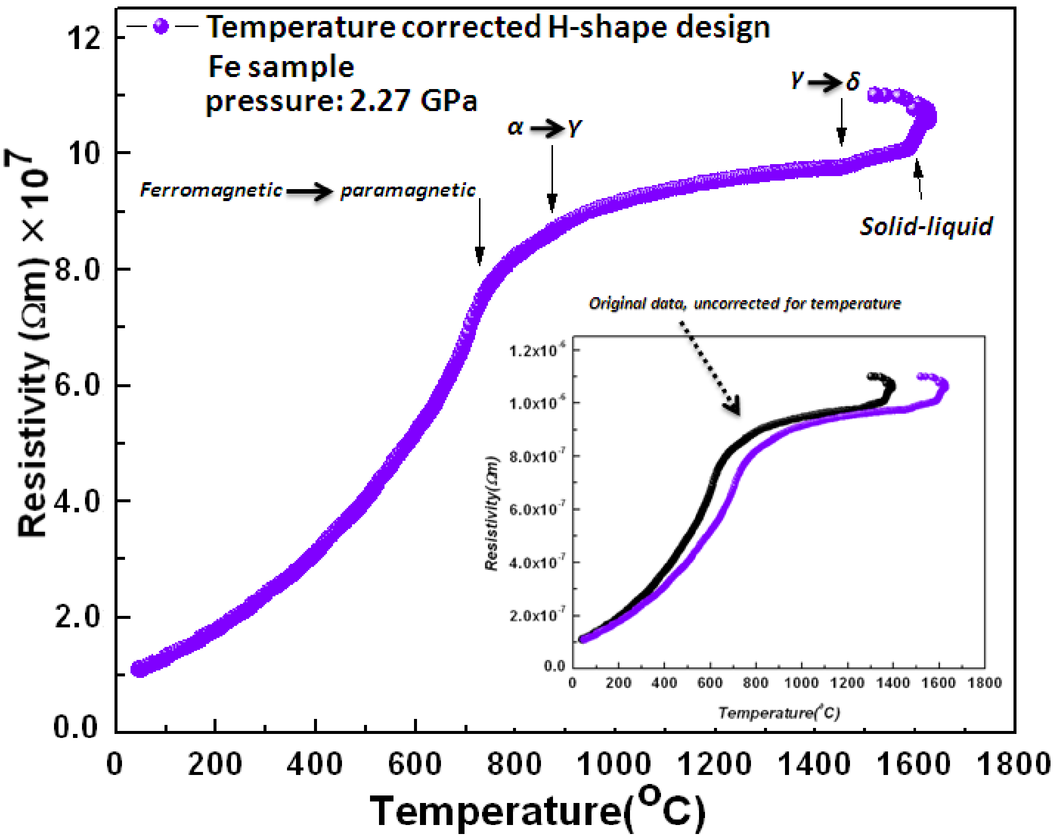

Figure 4.8 Temperature gradient corrected electrical resistivity data for Fe at 2.27 GPa from H-shape design. Inset shows original electrical resistivity data along with corrected values for the effect of thermal gradient. Resistivity scale indicates that all plotted values have already been multiplied by 10^7.

In an attempt to make temperature corrections, three electrical resistivity reference points at room temperature, α to γ transition and also melting transition were chosen. A quadratic polynomial was fitted to the temperature difference at the reference points between the H-shape transition temperatures and those from Strong et al. (1973). This polynomial was used to correct the T values of the H-shape design (insert in Figure 4.8). In a self-heating system, in addition to resistivity-temperature plots which can be directly used to indicate the transition points, current-temperature plots also contain noteworthy information regarding transition temperatures provided that, the current passing through the sample could be well adjusted so that the heating rate remains approximately constant (Secco and Schloessin,1989). However, as the current adjustment was not automated at a fixed rate in the present study, it makes it difficult to link sudden changes in current to phase transitions, which makes interpreting resistivity data and transitions not as straightforward as for a traditional external heating system. Providing an example, a current versus temperature plot in Figure 4.9, suggests a melting transition interval which does not exactly match the corresponding transition area in the resistivity-temperature plot.

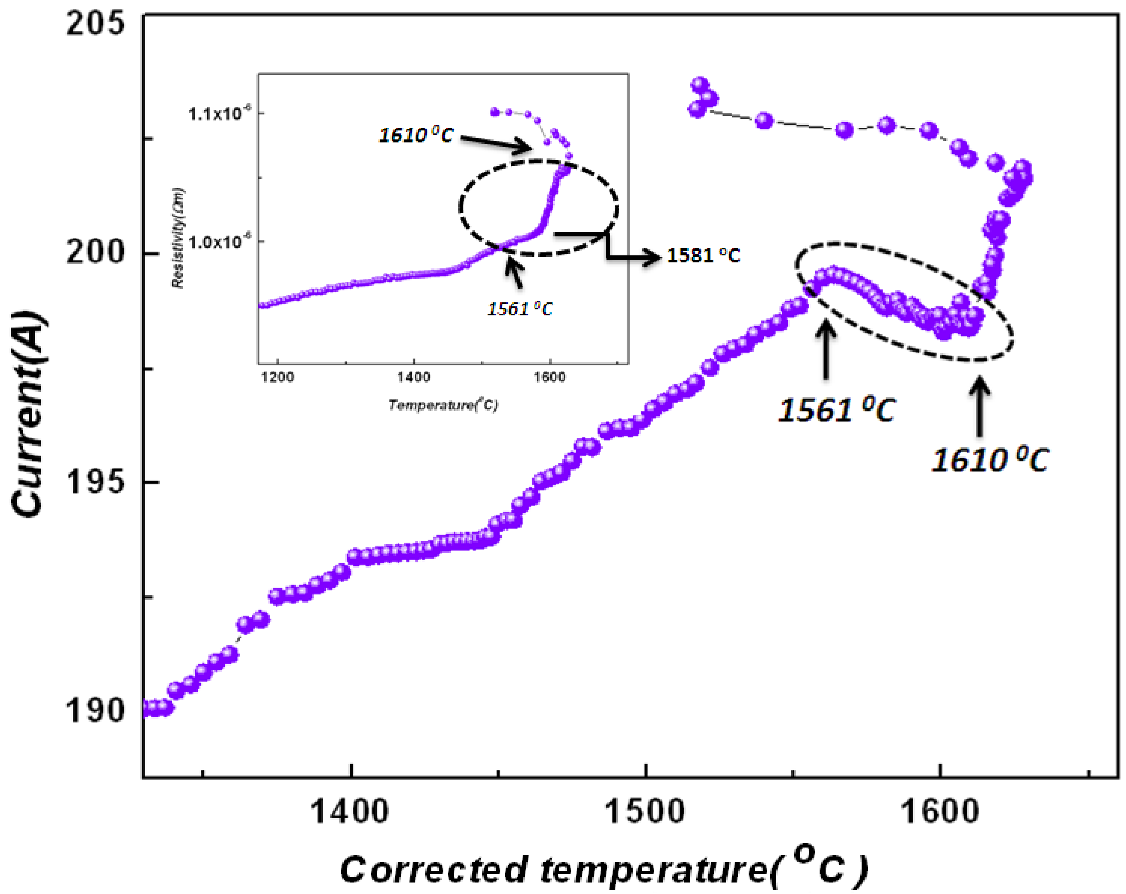

Figure 4.9 Comparison between phase transition identification between current-temperature plots and electrical resistivity versus temperature plots (insert).

Hence, it is more preferable to identify melting transition based on resistivity versus temperature data for the H-shape design unless an automated heating system is employed. The resistivity versus temperature plot in Figure 4.8 indicates a very clear transition signal for most of the four expected magnetic and structural phase transitions. Of more interest, compared to the traditional full cube design, it is the first time in this study to observe a clearly recognizable γ to δ transition around 1466 °C. Figure 4.10 illustrates the heating rate of H-shape design compared to a typical, very fast heating rate for the L16 run on Fe at 2.23 GPa discussed in Chapter 6.

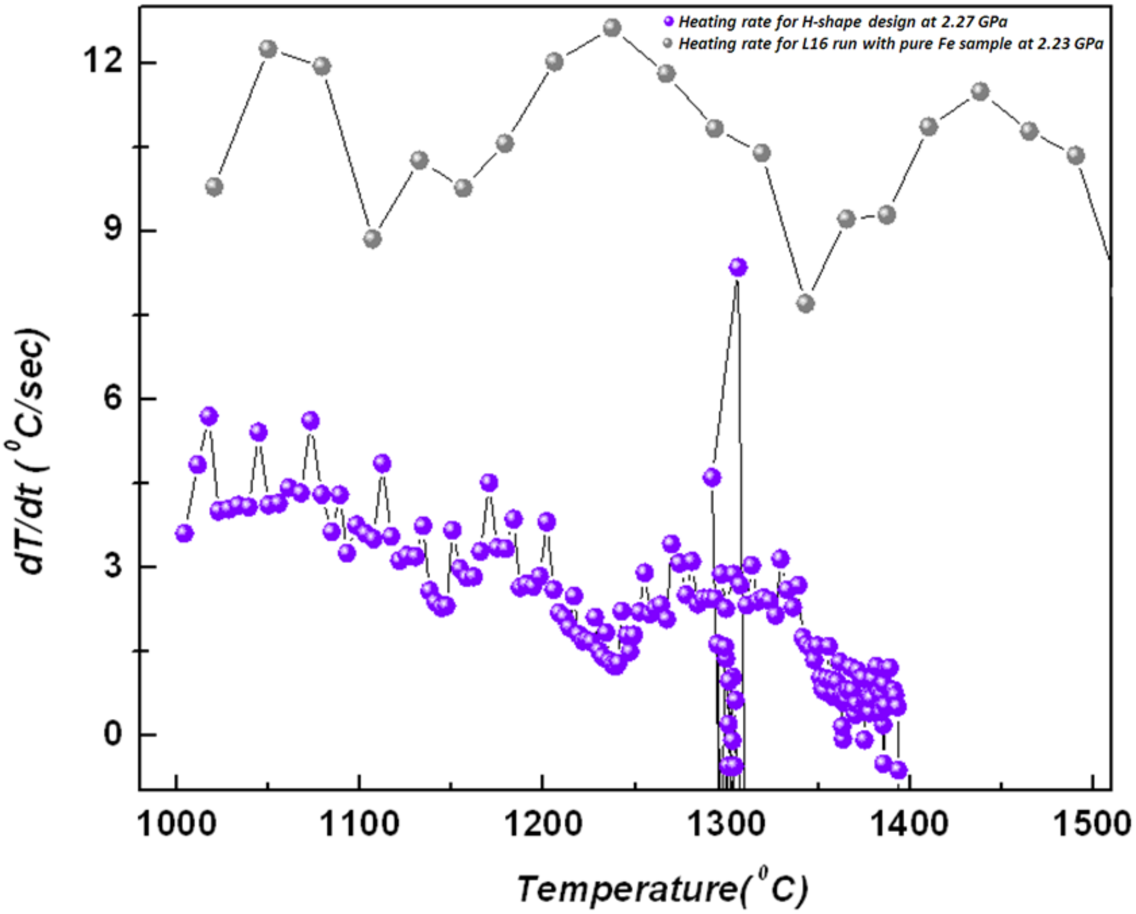

Figure 4.10 Heating rate comparison between H-shape design on pure Fe and a typical fast heating run in the 1000 ton press for Fe17Si sample.

In spite of removing the chemical contamination problem in H-shape design, it is still more preferable to make the heating rate as fast as possible in order to prevent the molten sample from diffusing into the thermocouple which is very close to the sample in the H-shape design.

4.3.2 Temperature coefficient of resistivity

The α to γ structure change is much better recognized in the temperature coefficient of resistivity (TCR= dln(ρ)/dT) versus T plots shown in Figure 4.11.

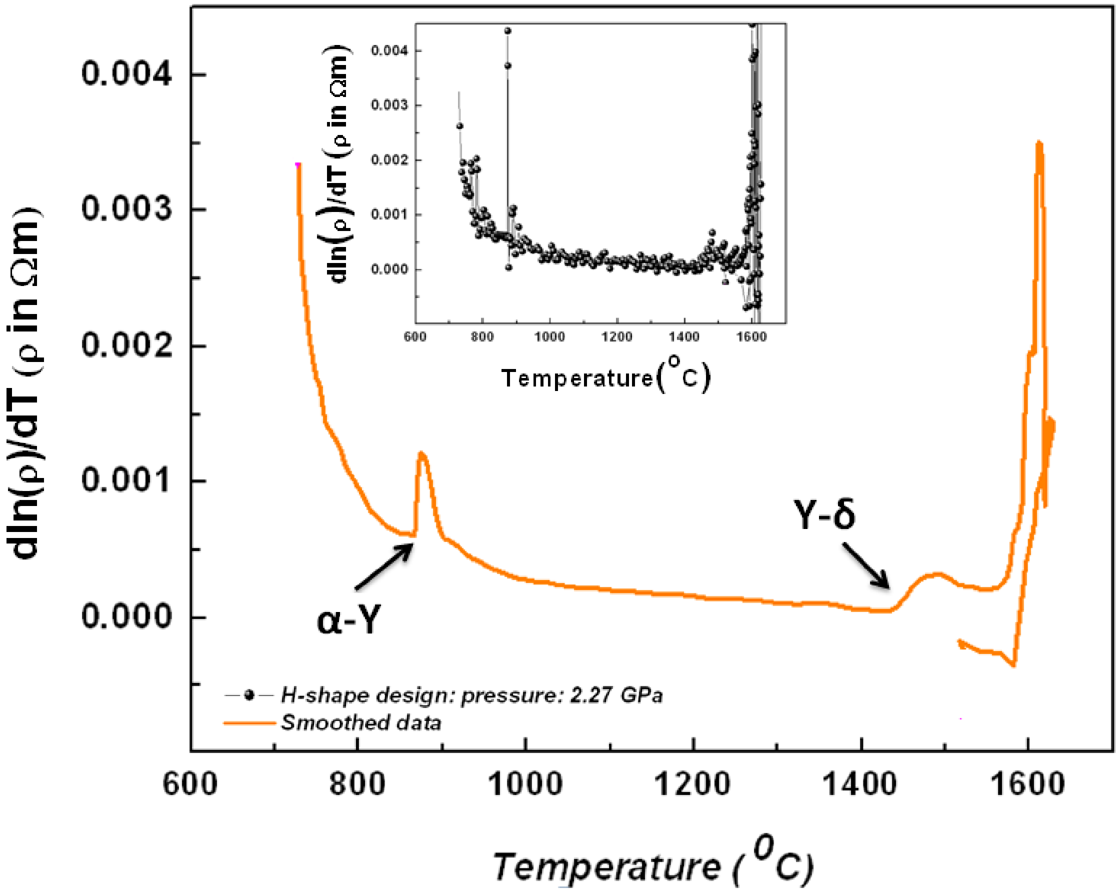

Figure 4.11 Smoothed TCR values for H-shape design. The insert illustrates the unsmoothed data.

As an important assessment for H-shape resistivity data, attempts were made to calculate the TCR within the melt and compare it with available data. There were not enough data points for I23 within the melt to calculate a reliable TCR value and I22 was believed to not have undergone melting. Therefore, a TCR value for I21 was calculated to be 2×10^{-4} K^{-1} and for the H-shape design, the TCR value was 3.2×10^{-4} K^{-1}. Secco and Schloessin (1989), reported the TCR values within liquid Fe to be of the order of 10^{-4} K^{-1}. Therefore, traditional and H-shape design values are proven to be well within the range.

4.4 Conclusion

A summary of the main results on the electrical resistivity of Fe of the present study in comparison with reported values from literature is given in Figure 4.12 and in Table 4.2. Comparing the traditional 2-wire method for I23, against the 4-wire H-shape, the behavior of electrical resistivity of both methods within solid and liquid phase is comparable. The melting temperatures of both designs also are within range comparing to the reported melting temperature from Secco and Schloessin (1989) at the same pressure as well as compared from the phase diagram of Anderson (1986) in Figure 4.8.The resistivity values obtained from both designs in the present study show comparable values to Secco and Schloessin (1989) and more importantly they all exhibit significant lower electrical resistivity values than room pressure experiments. This is well in accord with the expected characteristics of pure Fe to have a negative pressure coefficient of electrical resistivity (PCR) (Secco and Schloessin, 1989; Sha and Cohen; 2011). In terms of sensitivity to structural transitions though, the H-shape design has proven to be a more successful design specifically for the γ to δ transition which was more challenging to detect possibly because of the frequency of data acquisition in earlier experiments. However, as there was no electron microprobe (EMP) analysis carried out on these samples, no solid conclusion can be made regarding the effect of Pt contamination on pure Fe electrical resistivity in the I-series experiments and in the H-shape design.

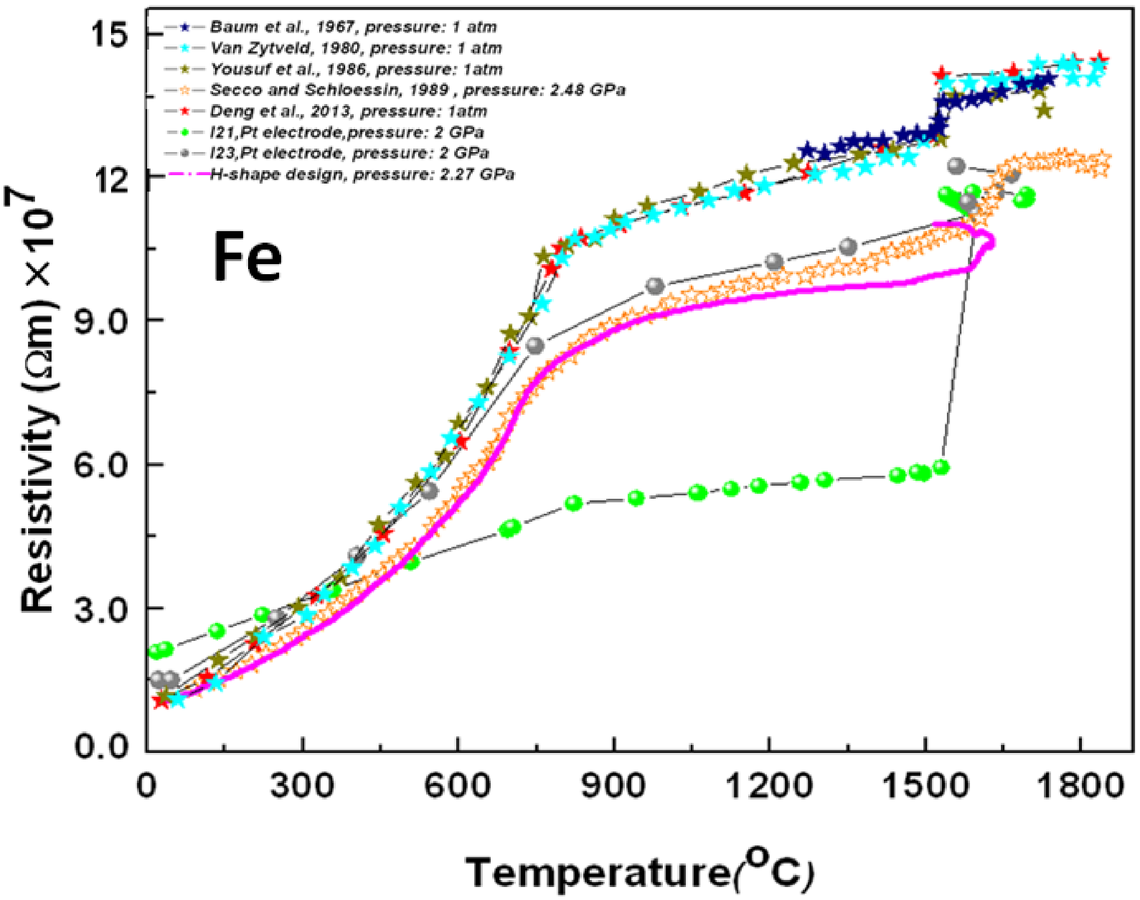

Figure 4.12 Temperature dependence of electrical resistivity of Fe from the present study compared to values from the literature. Resistivity scale indicates that all plotted values have already been multiplied by 10^7.

On the other hand, the contribution of the circuit electrical resistivity, which was a very significant factor in the traditional full cube design, was completely removed for the case of H-shape circuit. Therefore, either a modified two wire method should be deployed in which circuit resistance plays a minor role in the measured results or a 4-wire method should be considered for resistivity experiments on Fe. From all above mentioned arguments, H-shape design can be recommended for the electrical resistivity studies of conductive material under high pressure, high temperature provided that, brittleness of the sample (e.g. Fe-Si alloys) does not hinder fabrication of the H-shape piece.

Table 4.2 Data summary of the present work along with selected previous studies on pure Fe

Author	Pressure (GPa)	Melting T (^{o}C)	Resistivity at melting ($10^{-6}\Omega$m)	R_{liquid}/R_{Solid}
Powell (1953)	room pressure	1535	1.39	1.09
Baum et al. (1967)	room pressure	1532	1.35	1.038
Van Zytveld (1980)	room pressure	1535	1.37	1.08
Yousuf et al. (1986)	room pressure	1535	1.26	1.06
Deng et al. (2013)	room pressure	1518	1.28	1.09
Secco and Schloessin (1989)	2.48	1622 ± 17	1.12	1.07
H-shape design(this study)	2.27	1599±11	1.07	1.038
I23(this study)	2	1605±28	1.13	1.09

CHAPTER 5

5 Literature review on Si effects on electrical resistivity of Fe-Si alloy

Since early in the 20th century, the effect of Si on the electrical resistivity of pure Fe has been investigated from a metallurgical standpoint at ambient conditions. However, with Si being a strong candidate for the outer core (reviewed by Poirier, 1994), knowledge of the electrical resistivity of Fe-Si alloys under the Earth's core pressure and temperature is critical. On the other hand, as the outer core is liquid, there is a strong need for having experimental results as well as theoretical studies on the liquid phase of Fe-Si alloys. However, due to challenging technical problems associated with high P, T experiments, the number of experimental studies for Fe-Si alloys under core conditions is scarce. Pressure, temperature and alloying effects, interact in a complicated way so that they cannot be easily added or multiplied to each other. As the phase diagram of Fe-Si alloys is indispensible for having an accurate interpretation of electrical resistivities and the melting temperature of Fe-Si, a brief discussion is provided in the following before a review for temperature and pressure effects on electrical resistivity.

5.1 Phase diagram of Fe-Si alloys

Understanding the phase diagram of Fe-Si alloys at ambient and high pressure is necessary to characterize the observed resistivity anomalies of the present experimental work. The Fe-Si T-X phase diagram at 1 atm has been extensively studied by several chemists, metallurgists and physicists (Hansen, 1958; Hultgren et al., 1973; Kubaschewski, 1982; Bannikh et al., 1986; Ohnuma et al., 2012). Close to 17wt% Si, the phase diagram becomes more complicated than lower Si concentrations and also there are considerably fewer literature studies on that region. The compiled atmospheric pressure T-X phase diagram by Numakura and Tsugawa (1972) and Ohnuma et al. (2012) is shown in Figure 5.1. There are five phases α, α_1, α_2, η and ε of interest close to 17wt% Si. The first three have body-centered cubic (bcc) structure, η has an ordered hexagonal-closed packed (hcp) structure of $D8_8$ type and ε has an ordered cubic structure of B20 prototype (Matassov, 1977). Phase α is disordered compared to two other bcc phases, α_1 shows short range order (superstructure $D0_3$ of $AlFe_3$ type) and α_2 shows long range order (superstructure B2 of CsCl type). $D0_3$ may be viewed as being made up of four fcc sublattices with atoms A, B, C and D regularly positioned along the body diagonal with A atom at the centre of a cube with four B and four D atoms at the corners. Fe atoms occupy the A, B and C sites and Si atoms sit on the D site. Fe atoms on A and C sites have tetrahedral point symmetry while Fe atoms on the B sublattice have cubic point symmetry (Kudrnovskỳ et al., 1991; Rhee et al., 2004). Starting from room temperature, the phase diagram in Figure 5.1a suggests that on approaching the melting boundary, several coexistence regions of the above mentioned phases will be met. Above Xsi = 0.25, phase α_1 coexists with phase ε up to 825°C and with phase η between 825 and 1020°C. The updated phase-diagram of Fe-Si alloys is illustrated in Figure5.1b which has more detailed investigation on the coexistence areas of α_1 and α_2 up to Xsi = 0.25. However, the challenging issue is to recognize these boundaries by an appropriate method. The more debatable point is to introduce the effect of high pressure and then investigate the possible (i.e. as yet unmapped) changes in phase boundaries. In the next chapter, it will be shown that electrical resistivity is able to discriminate between different structures including order-disorder phases up to the melting boundary.

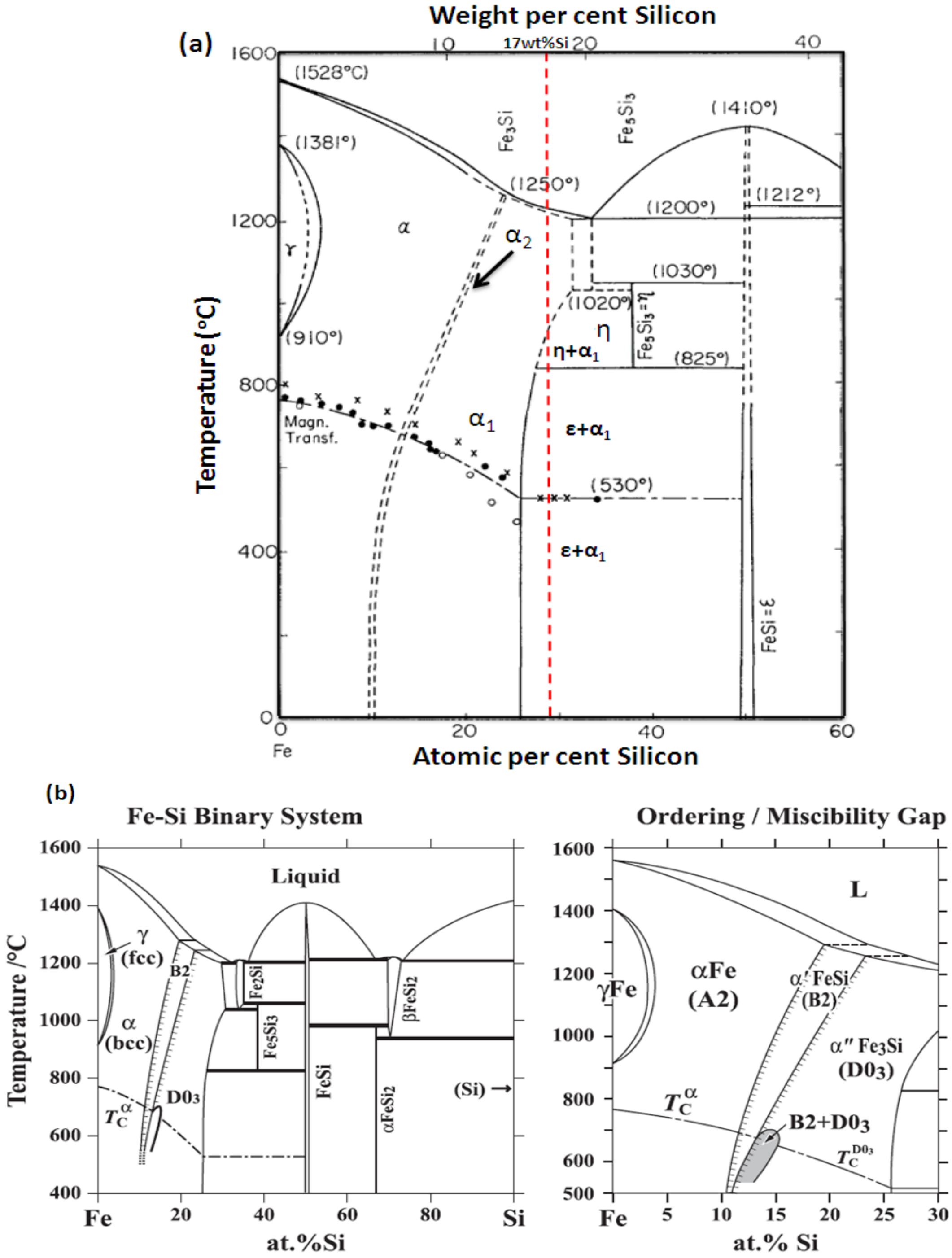

Figure 5.1 (a) Fe-Si phase diagram at 1 atm from Numakura and Tsugawa (1972). Red dashed line approximately indicates the 17wt%Si composition. (b) Ohnuma et al. (2012).

5.2 High pressure phase diagram of Fe-Si

Most of the high P,T experimental and theoretical investigations on Fe-Si alloy phase diagram have been either focused on Si concentrations less than 10 wt% (Zhang and Guyot, 1999; Lin et al., 2002; Asanuma et al., 2008; Lin et al., 2009; Brosh et al., 2009) or 16-18 wt%Si at high pressure but room temperature (Lin et al., 2003a; Hirao et al., 2004) or 16-18 wt%Si alloys of Fe at high pressure, high temperature but not covering the low pressure range (2-5GPa) of interest in the present study (Miller, 2009; Morard et al., 2011; Fischer et al., 2012). A very recently reported phase diagram (Fischer et al., 2012) result is shown in Figure 5.2.

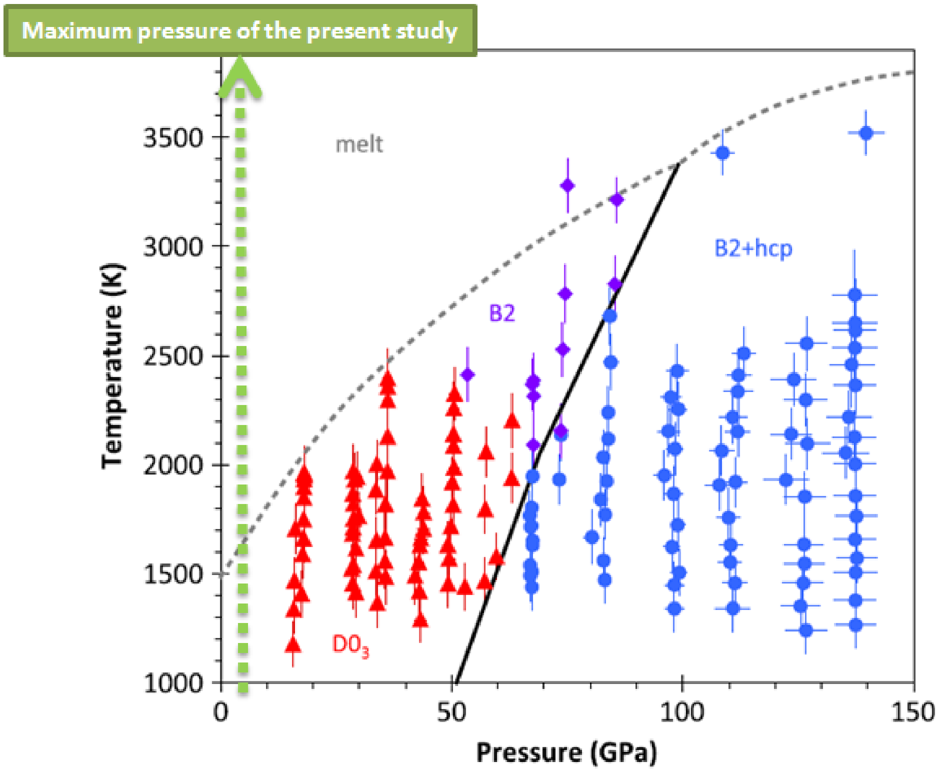

Figure 5.2 High P–T phase diagram of Fe–16Si alloy from Fischer et al., (2012). The dashed arrow indicates the maximum pressure attained in the present study.

5.3 Composition effects on the electrical resistivity of Fe-Si alloys

Based on several experimental studies, it is commonly known that the addition of silicon markedly increases the electrical resistivity of Fe (Yensen, 1915; Corson, 1928; Domenicali and Otter, 1955; Glaser and Ivanick, 1956; Pry, 1959; Backlund, 1961; Baum et al., 1967; Littmann, 1971; Numakura and Tsugawa, 1972; Nishino et al., 1993; Varga et al., 2002; Ruiza et al., 2005). Reported values from experimental works exhibit a linear dependence of electrical resistivity on Si concentration for low Si wt% as shown in Figure 5.3 which compares Si with other impurities in Fe.

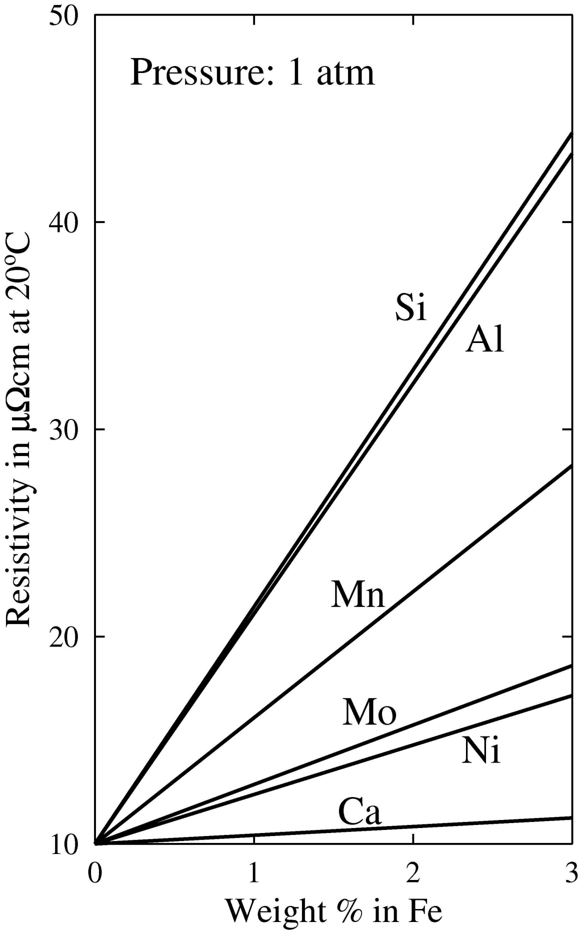

Figure 5.3 Electrical resistivity of several binary Fe alloys (after Pry, 1959).

However, as the Si concentration increases beyond 3wt% Si, as shown in Figure 5.4, the reported experimental values do not follow a linear trend anymore.

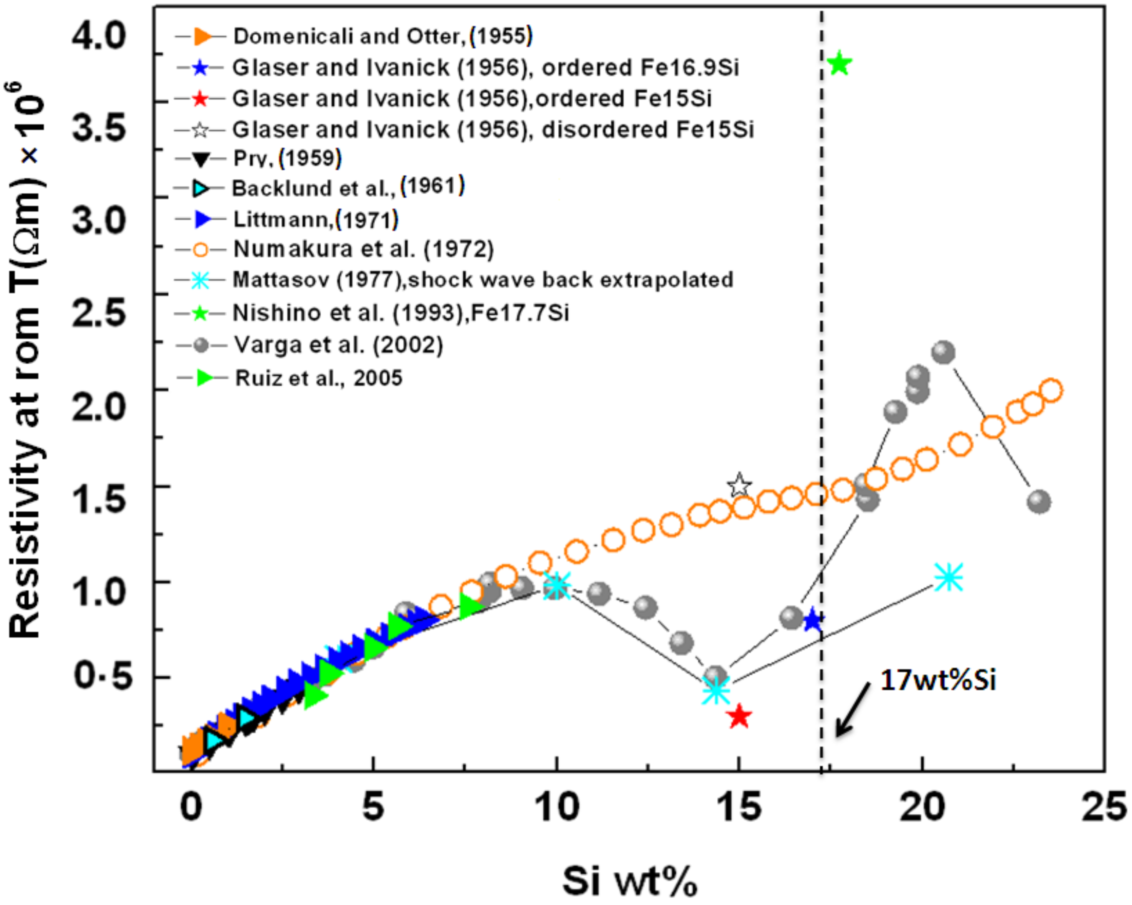

Figure 5.4 Review of room pressure and temperature electrical resistivities of Fe-Si alloys at 1 atm reported in literature. Open symbols indicates reported disordered compositions. Resistivity scale indicates that all plotted values have already been multiplied by 10^6.

Adding more silicon into the system shows a more complicated behavior. Studies from Numakura and Tsugawa (1972), Varga et al. (2002), and Ruiz et al. (2005), revealed more surprising behavior for higher Si composition alloys. Their results put strong emphasis not only on the Si composition effect on the electrical resistivity behavior, but also on the effect of different thermal treatment history of Fe-Si alloys between 5-20 wt%Si on the structure and consequently electrical resistivity of the quenched phase. As it is shown in Figure 5.4, between 5-20wt%Si, the same composition can have different electrical resistivity values based on whether the sample is quenched slowly (gray solid circles in the kettle bottom shaped curve) or quickly (the orange open circles). This phenomenon is in fact related to the order-disorder behavior of FeSi alloys, which for some compositions, such as 15wt%Si, according to Glaser and Ivanick (1956), can lead to a difference in resistivity of a factor of 3 between the two states. The order-disorder is a structural feature that is attributed to the formation of B2 and $D0_3$ phases as the highly ordered structure compared to α phase which is a disordered bcc phase. For compositions around 4-6.5 wt%Si, this ordering behavior and its effect on various physical properties of Fe silicon alloys, has been studied extensively because of the vast industrial application of this specific range of compositions that exhibit good magnetic properties, i.e. low coercivity and high permeability. Therefore, these alloys have a potential application in magnetic devices (Ciurzyfiska et al., 1994; Ciurzynska, 1998; Ros-Yanez et al., 2005; Wittig et al., 2008; Cava et al., 2011; Fu et al., 2011). The order-disorder phenomenon highlights the need for critical consideration for the starting Fe17Si material in the experiments of the present study which was prepared by compressed, heated and quenched Fe17 Si alloy. The stock Fe17Si alloy powder was purchased from Goodfellow Corporation with a reported purity of 99%. The other impurities are Al (0.01%), Cr (0.05%), Mn (0.07%), Ni (0.08%) and Ti (0.02%) which total 0.23%. This amount of impurity is not expected to significantly alter the results reported here. The heating and cooling rates are explained in Chapter 6.

5.4 Temperature effects on the electrical resistivity of Fe-Si

The temperature dependence of electrical resistivities of Fe-Si alloys, are well characterized compared to the pressure effects because of the practical difficulties specific to high pressure experiments. It is suggested by theory (Rossiter, 1987) that in dilute alloys, the scattering from impurity atoms is nearly independent of temperature so that the resistivity at any temperature can be written as (Matthiessen rule):

$$\rho_{total}(T) = \rho_0 + \rho(T) \qquad (5.1)$$

where, ρ_0 stands for residual (impurity) resistivity and $\rho(T)$ indicates the temperature dependence of pure Fe resistivity. However, it is only for dilute alloys that this rule can be applied. Considering the impurity concentrations suggested for the Earth' core, this rule fails to work and Si impurities affect the scattering mechanisms (Zinovev et al., 1973). For non-dilute Si concentrations, the temperature dependence of resistivity of Fe-Si alloys at a fixed pressure has a strong dependency on the composition of Si and does not obey the Matthiessen rule anymore. As an indication, studies by Nishino et al. (1993), show that based on Si composition and below the Curie temperature, TCR value at room pressure is different for various Si compositions and no longer resembles pure Fe TCR behavior up to 25wt%Si. Another study on electrical resistivity of Fe-Si alloys in the range of 800 to 1700^{o}C, shows that close to the melting temperature, TCR values are negative for compositions of 14.36 to 75 wt% Si in contrast to that of pure Fe (Baum et al., 1967). This again points to the fact that Fe-Si alloying system does not follow the simple additive rule under the effect of temperature. From another perspective, Mooij (1973) suggested that temperature-induced high electrical resistivity in metallic conductors, tends to reduce TCR value and finally making it negative above a critical value of resistivity in such a way that electrical resistivity saturates at a universal value of about 100-160 μΩcm over which the mean free path of electron, Λ, becomes comparable to the lattice spacing a_o. At this condition called the Ioffe-Regel criterion, the Matthiessen rule breaks down. However, later on Tsuei (1986) argued that resistivity values of saturation are not a universal range. In conclusion, for dilute Si concentrations, the overall temperature dependency of the alloy follows that of pure Fe as was discussed in Chapter 3. However, for high Si concentrations, the resistivity behavior of alloys varies in a more complicated fashion with temperature as is observed in the present study and discussed in the next chapter.

5.5 Electrical resistivity of Fe-Si under Earth's core condition

Aiming to estimate electrical resistivity behavior under Earth's core condition, pressure dependency of electrical resistivity should be also considered. Challenges encountered are more serious in the case of pressure effects as there are not so many experimental data at high pressures to be used as extrapolation reference points. Bridgman (1957), reported measurements of resistivity for Fe and six Fe-Si alloys (0-3 wt%Si) at pressures up to 10 GPa. According to Bridgman (1957), pressure reduced the thermal scattering but it does not reduce the effect of impurity disorder. His results suggest that pressure and temperature can both lead to electrical resistivity increase for Fe-Si alloys. Based on such a finding, Gardiner and Stacey (1971), also conclude that adding impurity will modify the PCR values of pure Fe. Aiming for higher pressures comparable to the Earth's core, estimates of the pressure effect on the electrical resistivity of Fe-Si alloys was guided by shock wave observations (Matassov, 1977) which was carried out on the electrical resistivity of four Fe-Si alloys (4.02, 10, 14.35 and 20.72 wt%Si) in the pressure and temperature range of 50-140 GPa and 327-2245°C. According to Matassov (1977), the alloying effect of Si becomes less pronounced in electrical resistivity values as the pressure is increased. All resistivity measurements of different Si wt% compositions in addition to pure Fe, tended to converge at high pressures comparable to the Earth's core values. Recently, Gomi et al. (2013), performed high-pressure (up to 100 GPa), low-temperature measurements of electrical resistivity of Fe and a Fe-Si alloy (2.05 wt%Si). Their results suggest that Fe-Si electrical resistivity values follow a "saturation trend" as a function of pressure. Considering the effect of high P,T together, except for Matassov (1977), a few theoretical studies also have attempted to model the behavior of Fe-Si alloys at higher pressure and temperatures which are not yet possible to attain under laboratory conditions. This has been accomplished by either extrapolation of experimental values of Fe-Si electrical resistivities (Gardiner and Stacey, 1971; Yang and Secco,1999; Stacey and Anderson, 2001) or theoretical studies using first principle calculations and density functional theory respectively (de Koker et al., 2012; Pozzo et al., 2012 and 2013). Fundamental difficulties for extrapolating experimental data points to the core conditions do not exclusively stem from lacking knowledge about the individual effects of pressure, temperature or alloying but more importantly how these parameters interact and finally affect the resistivity. In an attempt to assess the individual effects of pressure, temperature and light element alloying on the electrical resistivity of Fe, Gardiner and Stacey (1971), combined values from Bridgman (1957) and Baum et al. (1967) and came up with the conclusion that at core temperatures but zero pressure, the effect of alloying with Si can be neglected. According to their assessment, the only significant effect of alloying on the electrical resistivity is to modify the pressure coefficient of resistivity. Matassov (1977) suggests that pressure and temperature effects in Fe-Si alloys are seen to compensate each other to a much larger degree than that observed in Fe. There is still need for data in order to understand the interconnecting effects of pressure, temperature and composition on electrical resistivity of Fe-Si alloys and specifically at the Earth core conditions.

CHAPTER 6

6 Fe-Si electrical resistivity experiments

6.1 Experiments in the 200 ton press

The general features of cell design have been discussed in Chapters 2 and 4. It should be noted that, in all Fe-Si experiments, external heating method was deployed, using a 0.005" thick Nb foil.

6.1.1 Powder sample

For all Fe-Si experiments carried out in the 200 ton press, the traditional, full cube design was used with the general aspects illustrated previously in Figure 2.4. For ease of discussion, experimental runs are denoted by P2n, where P stands for powder; 2 indicates the 200 ton press and n is the sequence number of the experiments. Four of the five experiments had a powder sample with 0.095" diameter and run P25 had a 0.05" diameter Fe17Si sample. For the first two experiments (P21, P22), electrical contact was made to the sample by deploying a Pt electrode in addition to Fe disks (0.004" thick) between sample and Pt electrode which served as a chemical shielding against possible Pt contamination. Cross sections of quenched cells are shown in Figure 6.1.

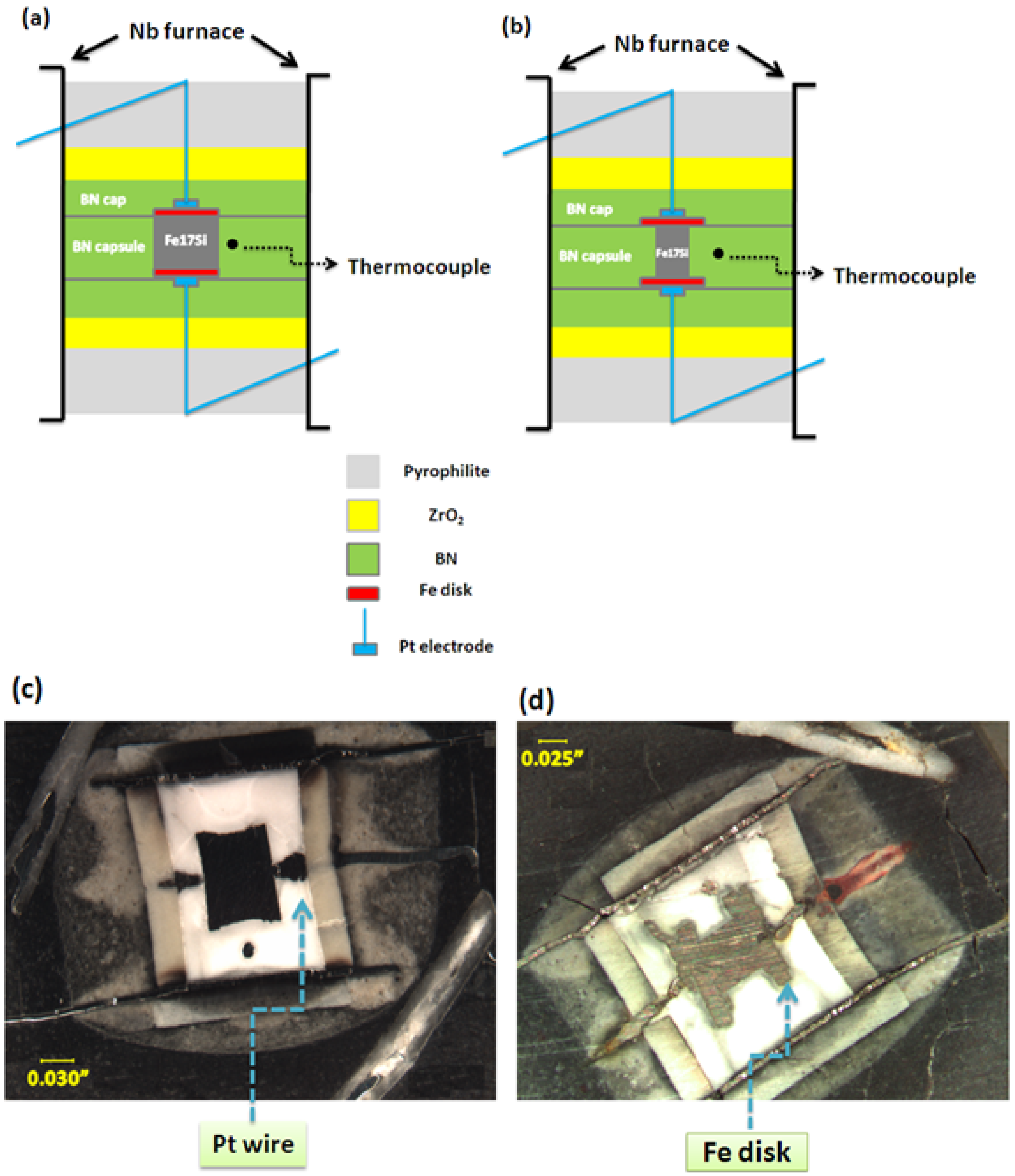

Figure 6.1 (a) Schematic cell drawing of P21; (b) schematic cell drawing of P25; (c) cross- section of recovered P21 cell with Pt electrode; (*d*) P25 cell with Fe rod electrode.

The next three cells (P23, P24, and P25) were designed to have pure Fe wire (0.01” thick) as the potential lead, with P25 having an extra Fe disk 0.1” diameter and 0.03” long in between the sample and Fe wire at each side. The idea was to remove the thin pure Fe electrode farther away from the hot zone and substitute that with less resistant pure Fe disk electrode.

6.1.2 Resistance measurements

For all electrical resistance experiments carried out in the 200 ton press, the two wire method was employed. Data acquisition was not automated and measurements were recorded manually from the voltmeter screen with the circuit voltage drop and emf values being measured via different channels of a Solarton 7061 voltmeter. The constant current through the sample was supplied by an Agilent E3632A power supply. A typical 100 mA constant current was sent through the sample to generate a measurable voltage in each run. Cells were pressurized to 2 GPa and then heated up through the melting point at a fixed pressure. Compared to later experiments in the 1000 ton press, the heating rate was steady and slow with the whole process lasting typically 45 min. As a common practice in our lab, quenched cells were cut in half and polished to allow geometry inspections which would then be incorporated into resistivity data calculation along with resistance values. Quenched cells for the first two runs, (P21 and P22), were sent for electron microprobe analysis (EMP) seeking information on any possible chemical contamination. The experimental details of the EMP are in Appendix A.

6.1.3 Results and discussion for 200 ton press experiments

Resistivity data plotted against temperature for all runs are illustrated in Figure 6.2.

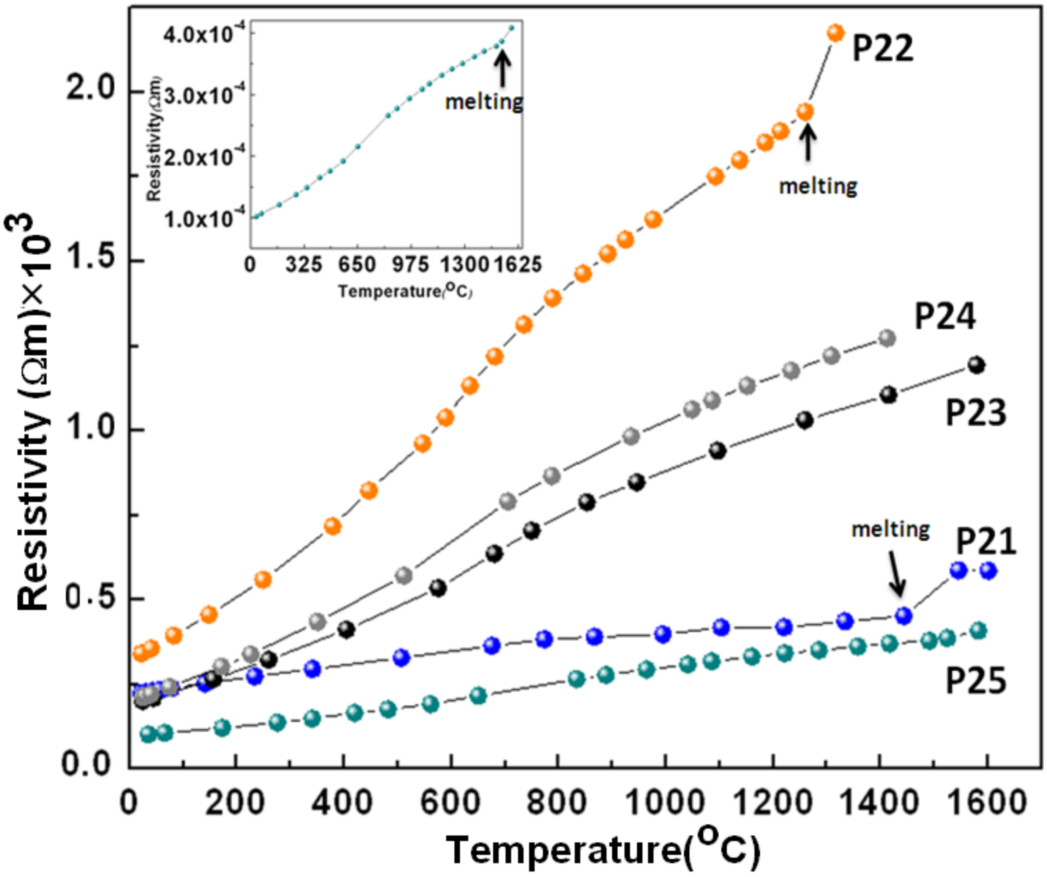

Figure 6.2 Temperature dependence of electrical resistivity of Fe17Si powder samples carried out in 200 ton press (P21-P25). Pressures were all at 2 GPa. P21 and P22 have Pt electrode with 2 and 4 Fe foil disks, respectively, shielding at each side of the sample. P23 and P24 have 0.01” thick pure Fe wire as the electrode material and P25 has a combination of 0.1” thick Fe disk and 0.01” thick Fe wires as for the electrode. The insert is the magnified view of P25 run results. Resistivity scale indicates that all plotted values have already been multiplied by 10^3.

Based on Yang and Secco (1999), as the only available high P,T study (up to 5 GPa) on Fe17Si electrical resistivity, the melting signature was expected to be a jump in resistivity versus temperature data, in contrast to a drop in resistivity at melting reported by Baum et al. (1967). Looking for melting signature as a discontinuity in resistivity versus temperature data, a jump was clearly observable for P21, P22 and P25 runs without any evidence of melting for P23 and P24 experiments. It should be noted that, the general cell design characteristics of the P2n series, was similar to what Yang and Secco (1999) employed for the electrical resistivity design. Lack of fast data acquisition method did not allow for collecting enough data points within the liquid phase for P21, 22 and P25 runs. The phase diagram of Fe17Si from Yang and Secco (1999), as shown in Figure 6.3, was used as a reference to expect the melting temperature during the experiment.

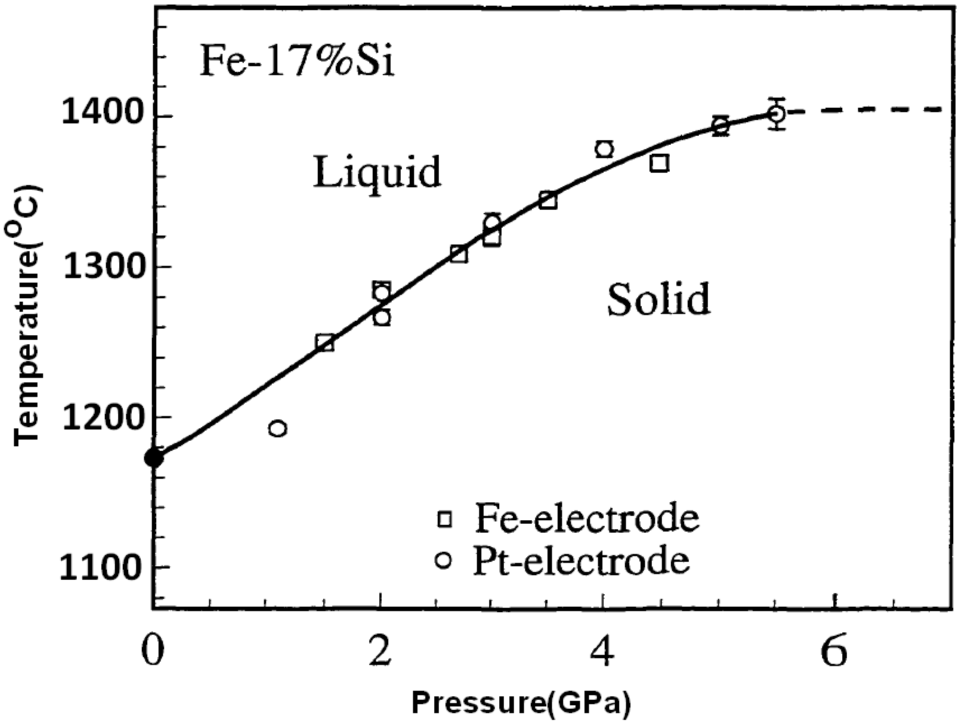

Figure 6.3 Melting boundary of Fe17Si at pressures up to 5.5 GPa (after Yang and Secco 1999).

Samples from P21 and P22 were analyzed with EMP method for any possible contamination and the results as shown in Figure 6.4. There was a significant amount of Pt diffusion into the sample for P21 experiment (Table A1 in Appendix A).

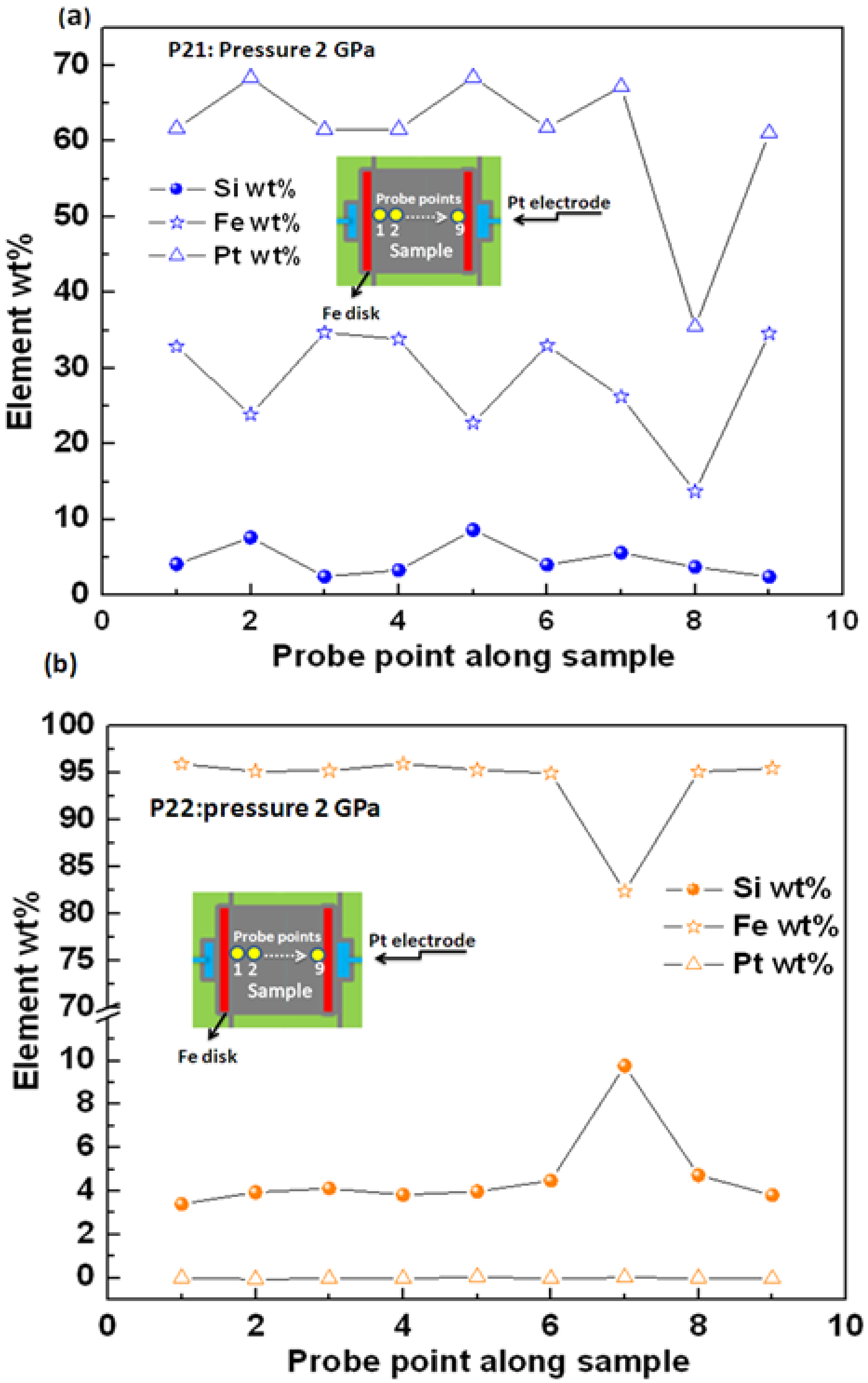

Figure 6.4 (a) EMP results for P21 cell; (b) EMP results for P22 cell.

In other words, the degree of contamination, made the system to turn into Fe-Pt-Si alloy with Pt a dominant constituent and a very small presence of Si (2-8wt %). For P22, which was protected against Pt by 4 Fe foil disks (0.004" thick) at each side of the sample, Pt contamination was reduced significantly. However, for this run, EMP results revealed that dominant contamination stems from Fe instead of Pt. Strictly speaking, this time, the chemical system of sample was turned into Fe-Si alloy with Fe dominant and again a very small amount of Si. For the rest of the experiments, P23 and P24 in which pure Fe wire was used as an electrode, which was lost at the end of the experiment, no solid-liquid signal was observed. On the other hand, for the last run in this series, P25, the melting signal was clearly observable. In connection with the EMP results and the heating rate, which was slow for all experimental runs compared to later experiments, it seemed three different systems of compositions were produced as a result of contamination: Pt rich Fe-Si-Pt system (P21); Fe rich Fe-Si-Pt system (P22) and possibly Fe rich Fe-Si alloy (P23, P24 and P25). In Table 6.1, the experimental characteristics are summarized. At first glance, the closest melting temperature to what Yang and Secco (1999) reported at 2 GPa (1312 °C) belongs to the Fe rich Fe-Si-Pt system. However, it should be noted that all melting temperatures, even for Fe-rich contaminated system (P25), are not close to the melting temperature of pure Fe at 2 GPa. In terms of the order of electrical resistivity though, P21 and P25 show resistivity magnitude closer to Yang (1999) values while the rest are approximately 10 times higher than Yang (1999). At this point, the second vital parameter that shows itself is the geometry of electrical circuit inside the cell. Taking all samples of approximately the same diameter (0.095") and with approximately a fixed circuit length inside the cell, the smaller the sample means the higher proportion will be the electrode resistance contribution. Also taking into account the diameter of electrodes (0.01”) compared to that of the samples, it seems reasonable to explain the highest resistivity for P22. On the other hand, the pure Fe electrode in P25 with wider diameter (0.05”) has the least electrode contribution among all which is reflected in it having the lowest electrical resistivity.

Table 6.1 Experimental characteristics for powder Fe17Si sample compressed in the 200 ton press.

Chemical system of recovered sample	Melting temperature (^oC)	Resistivity at high temperature/melting (Ωm)
Pt rich; Fe-Si-Pt (P21)	1444	4.52×10^{-4}
Fe rich Fe-Si-Pt (P22)	1260	1.94×10^{-3}
Fe rich Fe-Si alloy (P23, 24 and 25)	For P25: 1491 No melting observed for (P23 and 24)	3.78×10^{-4} (P25)

6.2 Experiments in the 1000 ton press with powder sample

For the pressure cell design in 1000 ton press experiments, the same general aspects as the 200 ton design were employed. Two main designs, Types A and B, were tested in which the Fe17Si sample was in the form of powder. In this series of experiments, each run is called P1n in which, P stands for powder sample; 1 indicates the 1000 ton press and n, the number of the experimental run in the series.

6.2.1 Fe17Si Chemical buffering design (Type A)

These specific experiments were designed to reduce the contamination problem by introducing a buffering method as well as a high heating rate. The design was aimed to delay diffusion of Fe and Pt into the sample by elongating the Fe17Si length away from the hot zone which removes the contact between the Fe electrode and the central hot zone of sample. As is illustrated in Figure 6.5, a long length of Fe17Si consisting of a small diameter Fe17Si central cylinder as well as a large diameter Fe-Si buffering disk at both sides are enclosed with a stepped BN capsule.

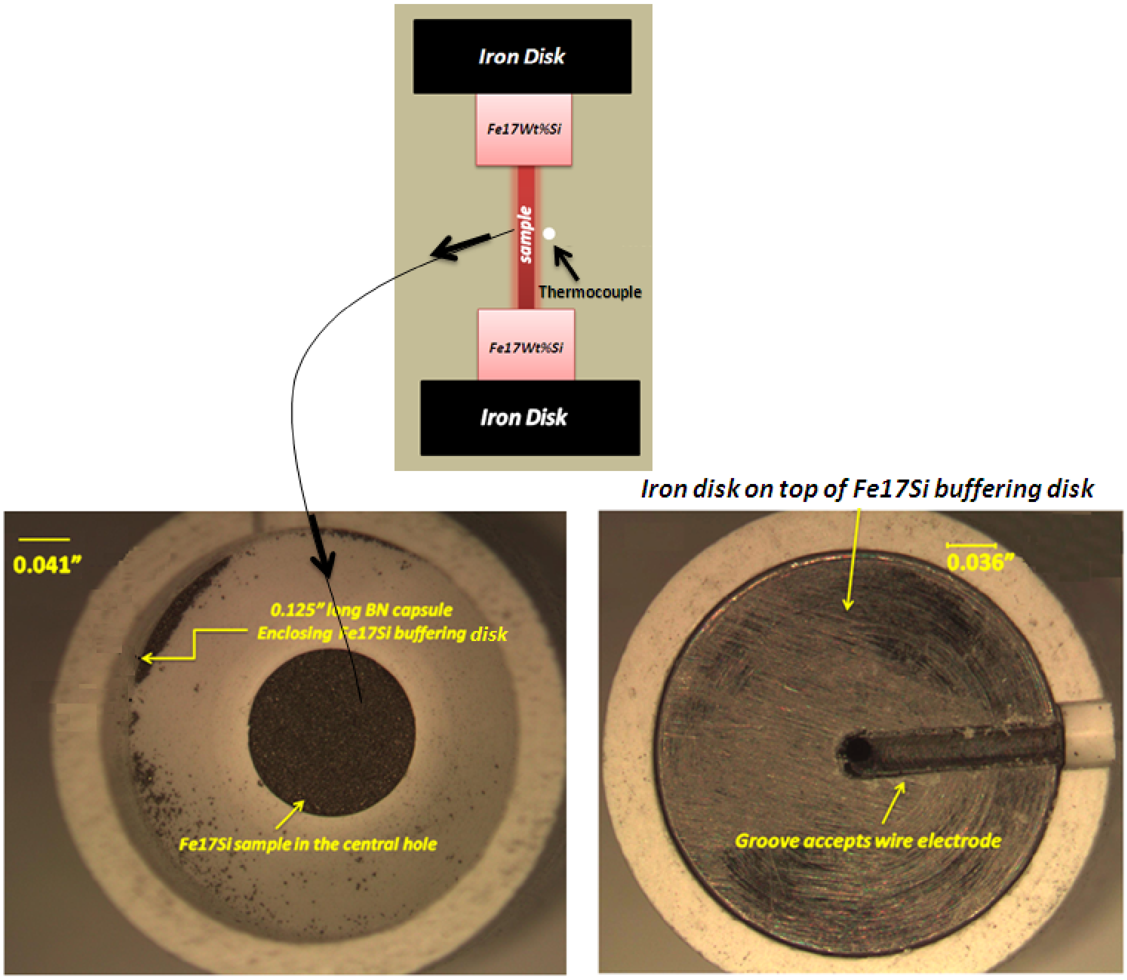

Figure 6.5 Schematic view of Fe17Si chemical buffering design.

Fe rods are in contact with Fe17Si buffering at both ends. Two experiments were tried and results are discussed in the following section. Data recording for voltage drop across the sample as well as the emf readings were carried out simultaneously with an Agilent 34972A digital voltmeter. As shown in Figures 6.6 and 6.7, EMP results on P11 and P12 respectively revealed a large amount of Fe contamination in the first while the second was almost intact and protected well against chemical contamination.

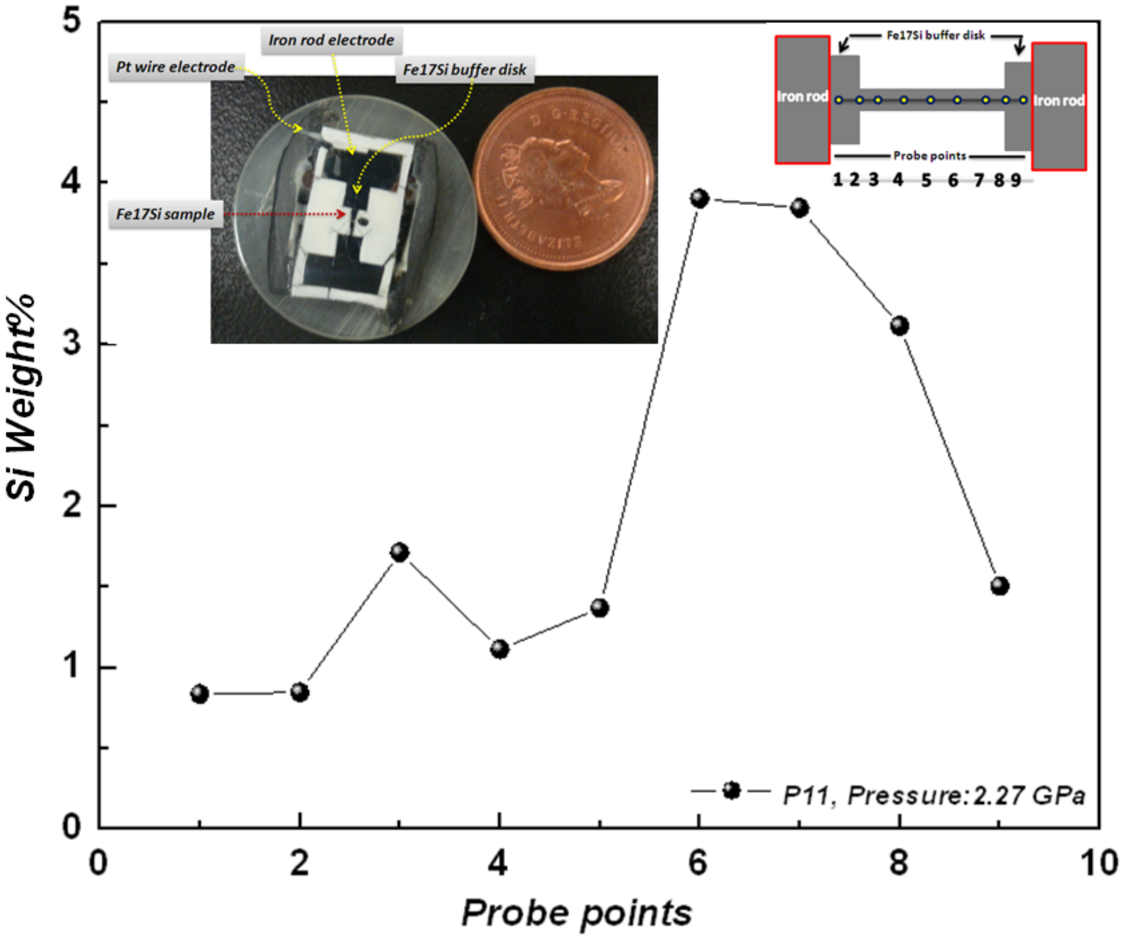

Figure 6.6 EMP results of Si concentration for P11. Probe path starts from one Fe-Si electrode and passes through sample toward the other electrode.

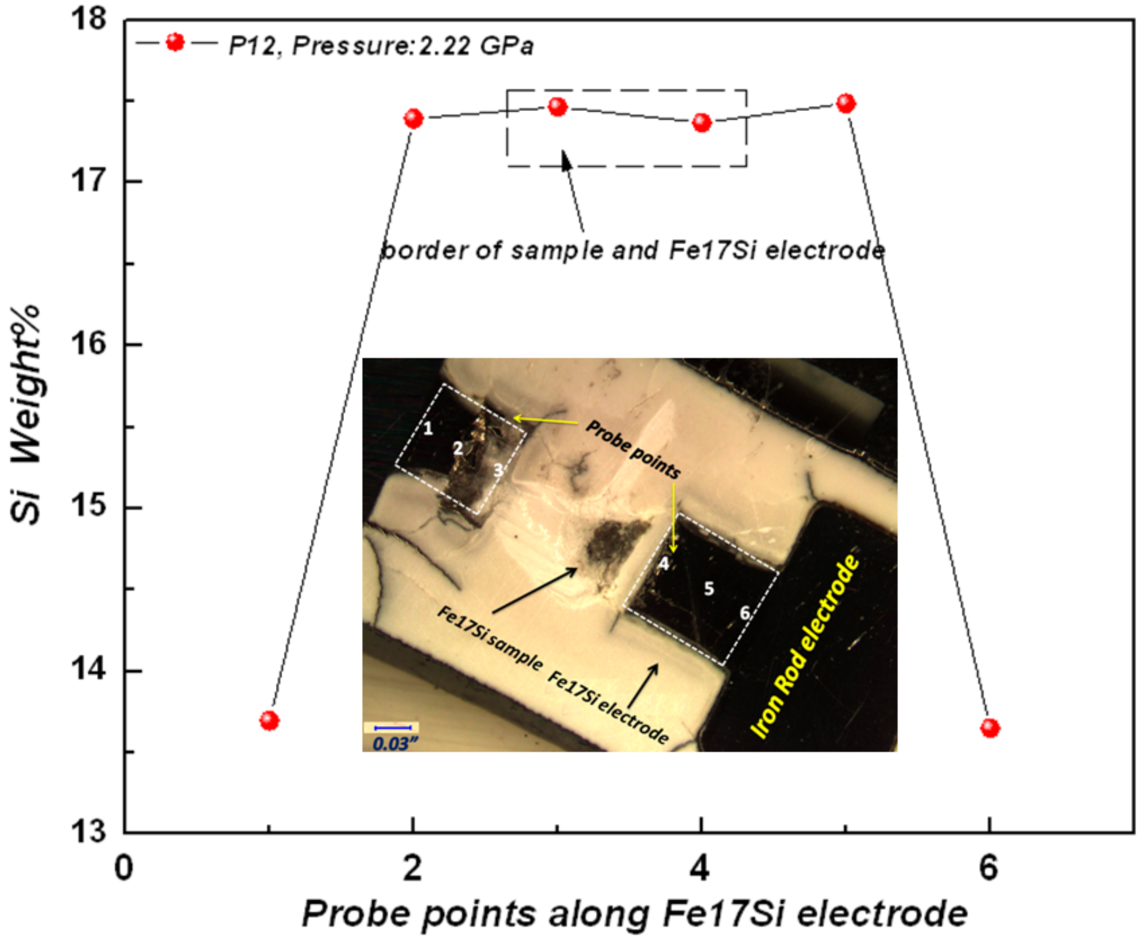

Figure 6.7 EMP results of Si concentration for P12. Probing path at both sides of the sample starts from the border of Fe and Fe-Si electrode toward the border of Fe17Si sample and Fe-Si electrode. Sample was plucked out on polishing.

Since the sample was plucked out for P12 cell, just the Fe17Si electrode area was investigated by EMP. However, the high Si concentration within both side electrodes ensures that central part containing the sample should be even in a better condition (See Table A3 and A4 in Appendix A). However, in spite of a higher heating rate for P11 as shown in Figure 6.8, contamination was more severe than for P12. This probably resulted from the fact that, although P11 had the faster heating rate, it reached much higher temperature and that can affect the diffusion process as diffusion rate increases with increasing temperature .

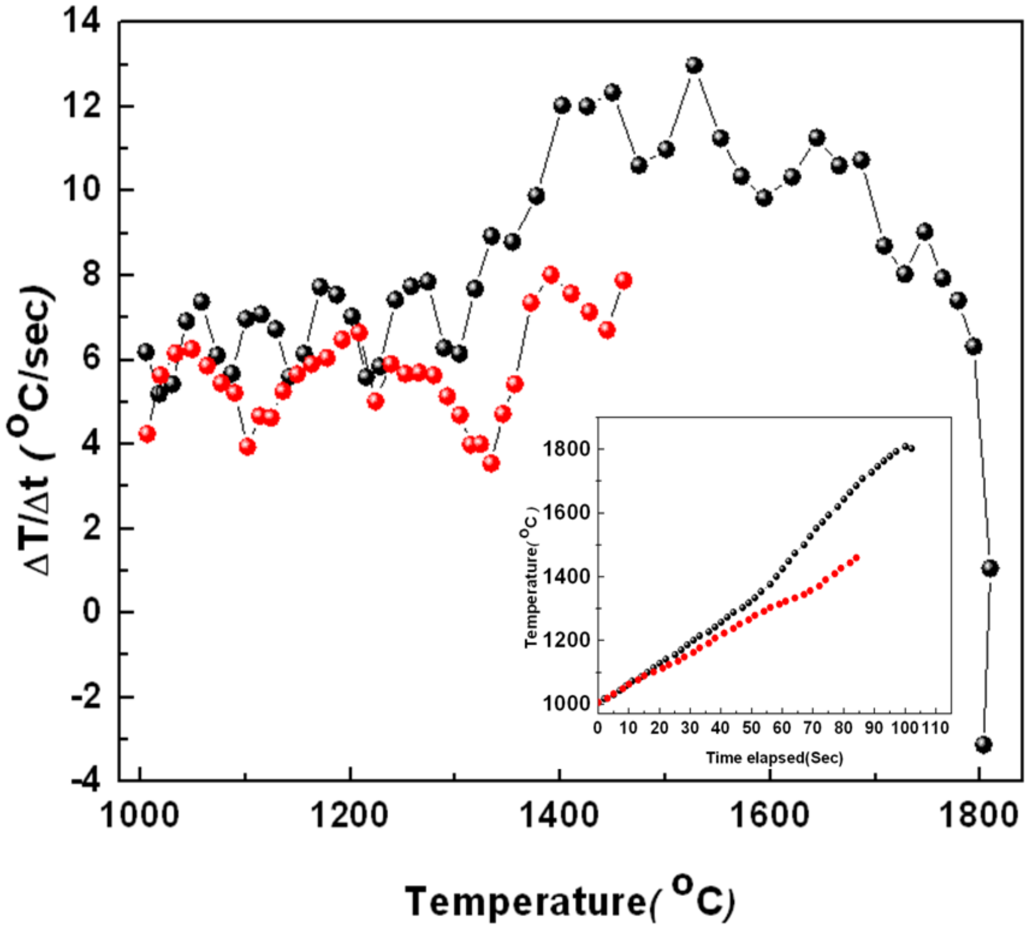

Figure 6.8 Heating rates for P11 (black circles) and P12 (red circles) runs and the insert showing time spent above 1000°C.

Figure 6.9 illustrates the reproducible but strange decreasing trend of both runs with a continuous decreasing trend at ~ 300 °C up to around 1100 °C. For both, lack of a good contact at the beginning and its probable improvement during the heating can explain a continuous drop in resistance values. It makes it clear that sample-contact quality is more critical for powder samples than for solid sample. Fe17Si chemical buffering proved to be a good design for stopping Pt and pure Fe diffusion into the sample. Results from P11 and P12 were also useful as they highlighted the importance of the maximum temperature reached during the experiment in addition to the heating rates.

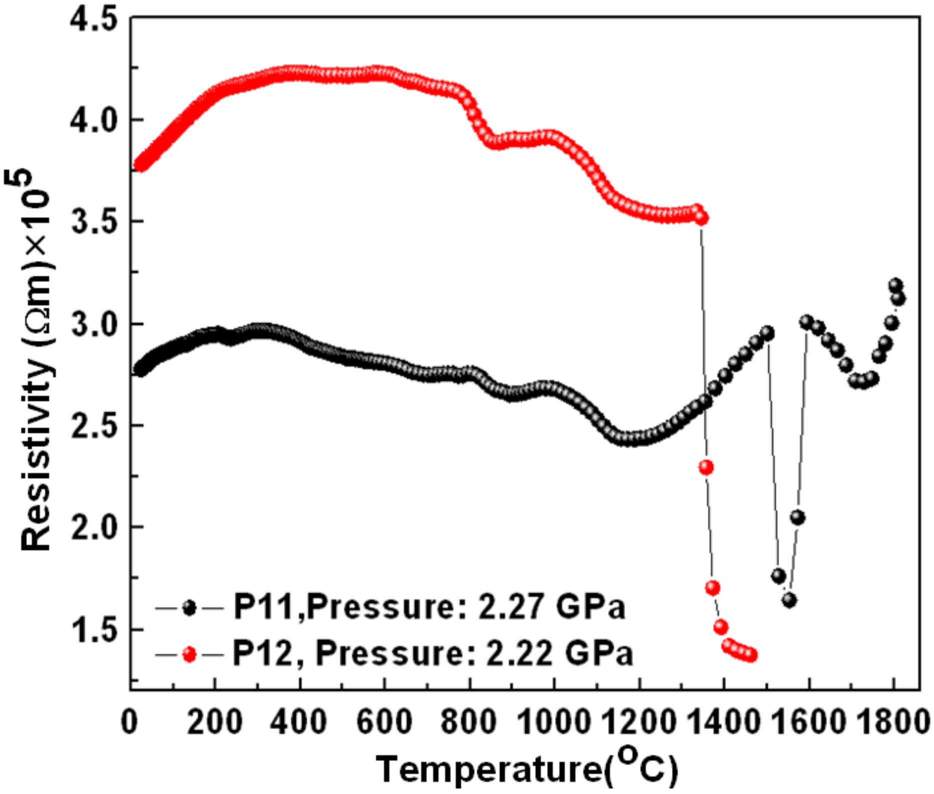

Figure 6.9 Temperature dependence of electrical resistivity for Fe17Si chemical buffering method. Resistivity scale indicates that all plotted values have already been multiplied by 10^5.

6.2.2 Type B design

The previous type A design produced irregularities in resistivity profile and the order of magnetite of resistivity was higher than expected from 1 atm studies. Therefore, it was decided to try a new design in which the wiring system exits from the interior of the cell to the anvils at the farthest distance from central hot zone area. Following that, both Pt electrode wire and thermocouple were designed to exit the cell from the same upper/lower planes relative to the centre as shown in Figure 6.10a.

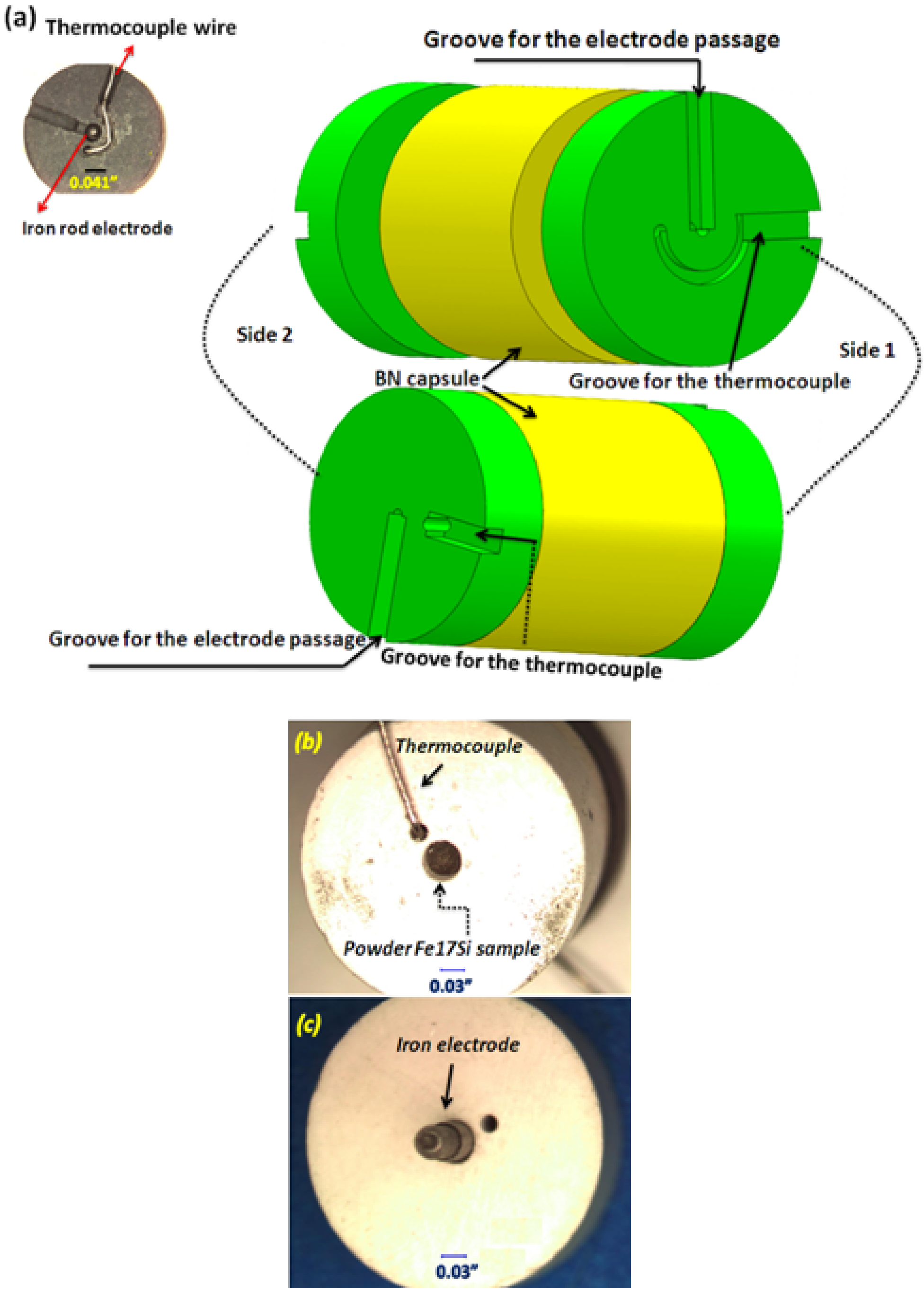

Figure 6.10 Type B design for the 1000 ton press showing (a) Pyrophyllite cap enclosing Fe rod electrode and a groove for the passage of thermocouple; (b) Location of

thermocouple and sample hole in relation to each other; (c) 0.04" thick Fe electrode sitting on top of sample hole.

Consequently, the cell benefits from less heat loss at the hot zone. The thermocouple was 0.025" from the sample as shown in Figure 6.10b. A Fe rod was kept as the electrical lead and its diameter was reduced compared to Type A experiments, in order to avoid passing the thermocouple through the Fe electrode as shown in Figure 6.10c. Two experiments, P13 and P14 were carried out with this Type B design. In experiments P13 and P14, the effects of heating rate as well as the circuit geometrical contribution were tested. EMP analysis was carried out for both P13 and P14 (Appendix A, Tables A5 and A6). From Figure 6.11 it can be readily inferred that both samples were well-protected against Fe and Pt diffusion. Heating rate information for experiment P13 and P14 is shown in Figure 6.12. The temperature dependence of electrical resistivity data are illustrated in Figure 6.13. Both P13 and P14 exhibit a large but broad signal extending from 700 to 1200°C, but with no melting signal observable around the expected melting temperature of 1312^{o}C. This time, resistivity values were smaller than in the P2n series at approximately the same pressure. Calculating the G-factor of P13 and P14, it yields a value of 2 which later will be compared with the G-factor of the entire experimental results for Fe17Si sample.

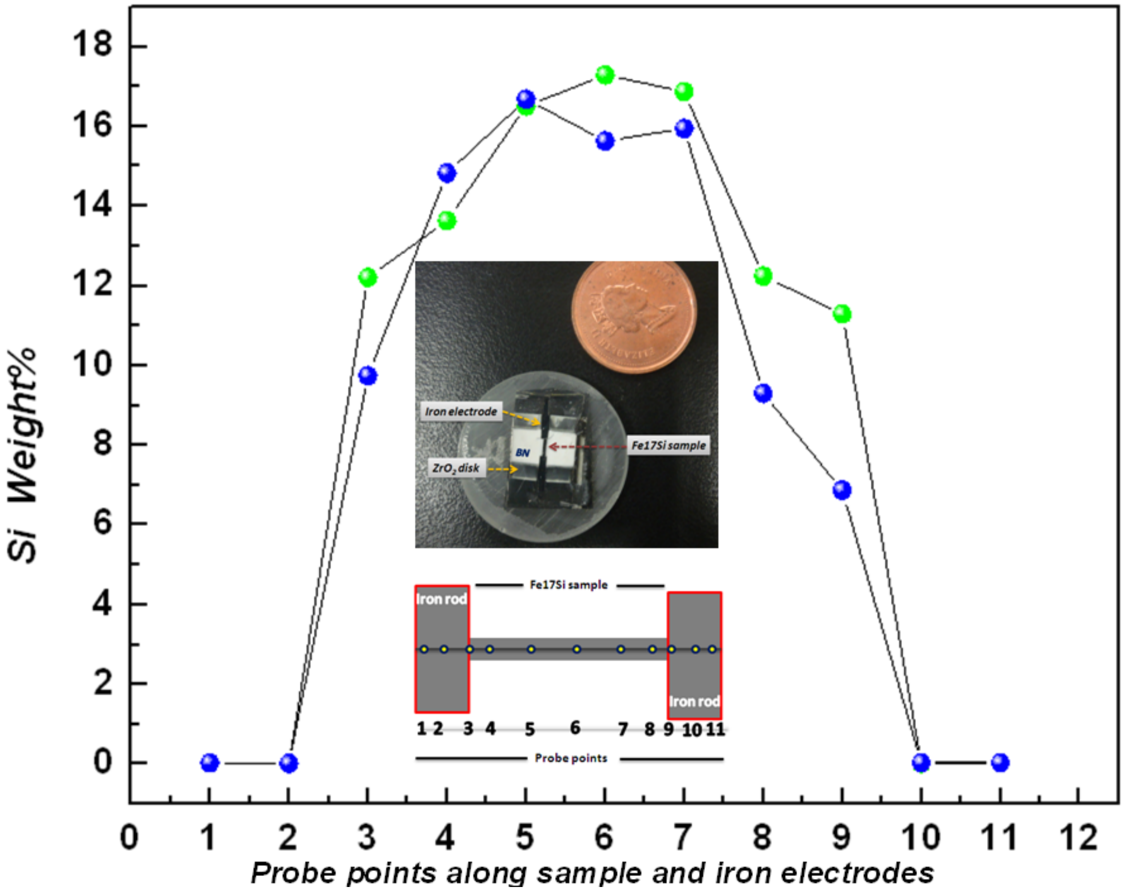

Figure 6.11 EMP results for type B design. Green circles: P13: pressure: 2.27GPa, sample length: 0.105"; blue circles: P14 pressure: 2.17 GPa sample length: 0.102". The insert illustrates a sectioned cube as well as the EMP probe path along sample and Fe electrodes for both P13 and P14 runs.

This value is compared with other experimental results from various cell designs of the current study at the end of Chapter 6. It is suggested that with almost same amount of contamination for P22, P13 and P14, lower G-factor of P13 and P14, may results in the smaller electrical resistivity values compared to P22 experiment.

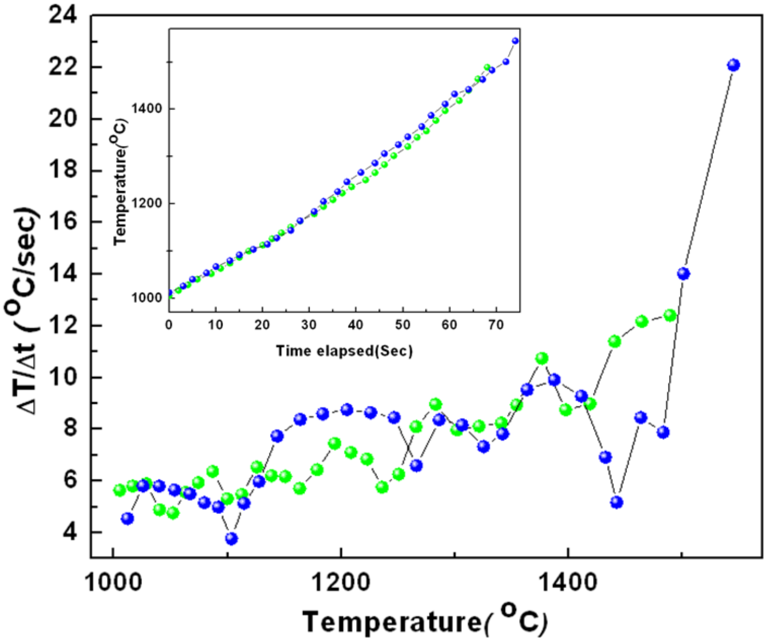

Figure 6.12 Heating rate and time spent above 1000°C for P13 and P14 experiments.

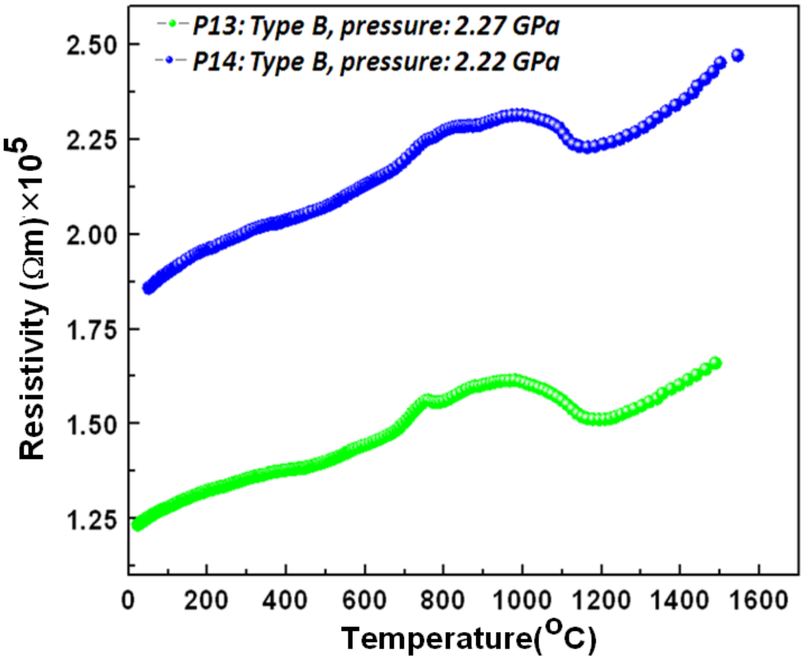

Figure 6.13 Temperature dependence of electrical resistivity of Fe17Si from P13 and P14 experiments. Resistivity scale indicates that all plotted values have already been multiplied by 10^5.

6.3 Three section design

In order to test the effect of electrode contributions to the resultant resistance signals, there was a need for an electrode, thick and short compared to the sample geometry. On the other hand, the straight contact between sample and electrode was considered to provide a much better electrical contact than previous designs in which two different electrode materials (Fe and Pt) were used with one taking an L-shape path (Figure 2.4) in order to exit from the cell. Moreover, the contact between Nb furnace and the electrodes was one of the common challenges for an L-shape electrode that should make its path through the furnace. Seeking a design devoid of the above-mentioned problems, a “three section cell” composed of three separate pyrophyllite rectangular pieces was designed as shown in Figure 6.14.

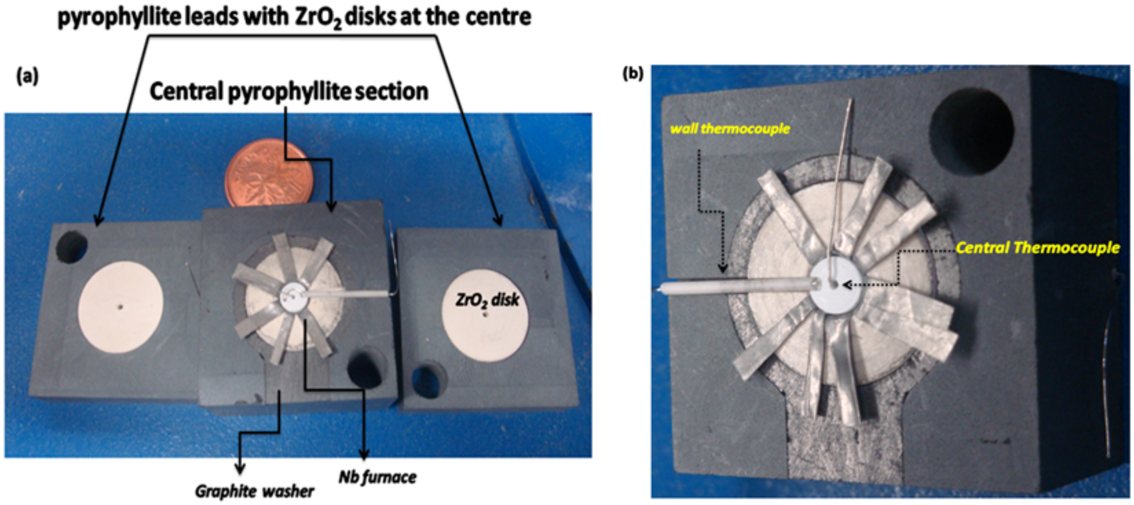

Figure 6.14 Cell cross section view for 3-section design. (a) Cell constituents; (b) Closer view of the central pyrophyllite.

The central section contains the sample and furnace and the upper and lower sections contain leads. The furnace no longer traverses the full cube but is a local heating system in the central section only encapsulated within a local ZrO_2 sleeve. A graphite washer guides the current to the Nb furnace and the thermocouple exits on both sides of the central section which requires no hole made within Nb furnace. Although progress was made with this design so that the furnace survived to high temperatures, the problem of the central plane thermocouple touching either the graphite or Nb furnace was not resolved. Figure 6.15 illustrates the cell constituents of a typical three-section design.

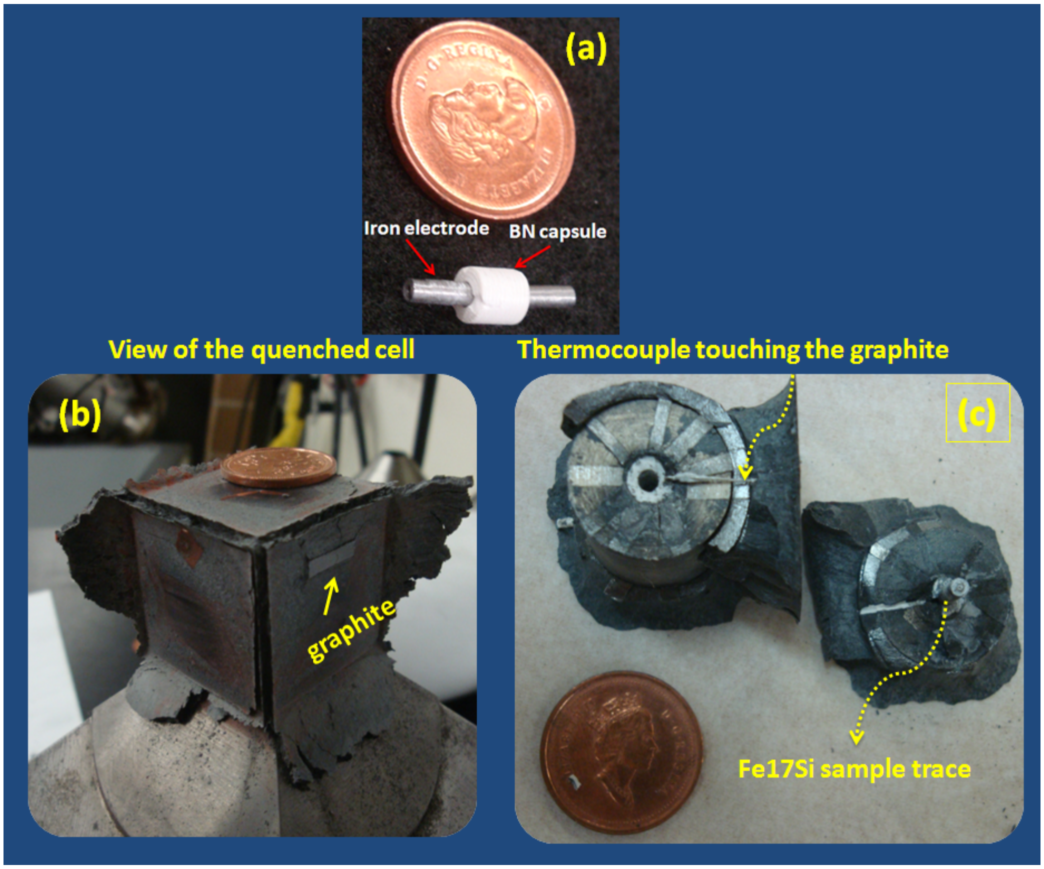

Figure 6.15 Three-section cell constituents (a) Fe electrode and BN capsule enclosed Fe17Si sample; (b) A view of the recovered quenched cell; (c) cross section of the quenched cell.

Resistance measurements are shown in Figure 6.16. That run was not successful because the thermocouple touched the graphite and the experiment was stopped accordingly.

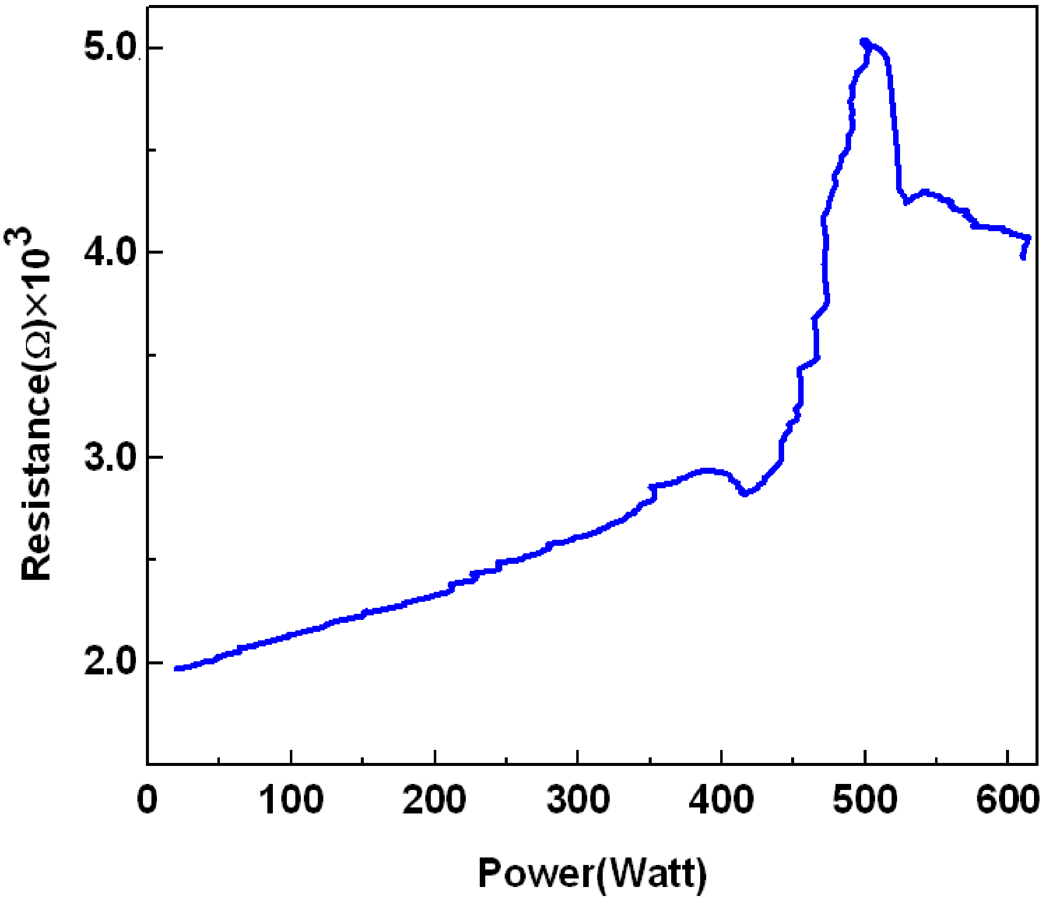

Figure 6.16 Resistance versus power for "three-section" design. Resistance scale indicates that all plotted values have already been multiplied by 10^3.

6.4 Compaction experiment

For experiments aimed at using a solid monolithic sample, a series of compaction experiments was performed in order to make a pre-compacted, well-defined shape Fe17Si alloy out of the initial powder sample. The design of compaction cell runs was of the same general characteristics as the traditional full cube cells (Figure 2.4). These experiments were called C1n as C stands for compaction, 1 for denoting 1000 ton press cell, and n is the number of experiment in the series. Fe17Si powder was well packed inside a BN capsule, compressed at 2.0GPa and maintained within the liquid state for an average of 3 minutes. Figure 6.17 shows the quenched solid Fe17Si cylinders which were later used as a sample for electrical resistivity experiments.

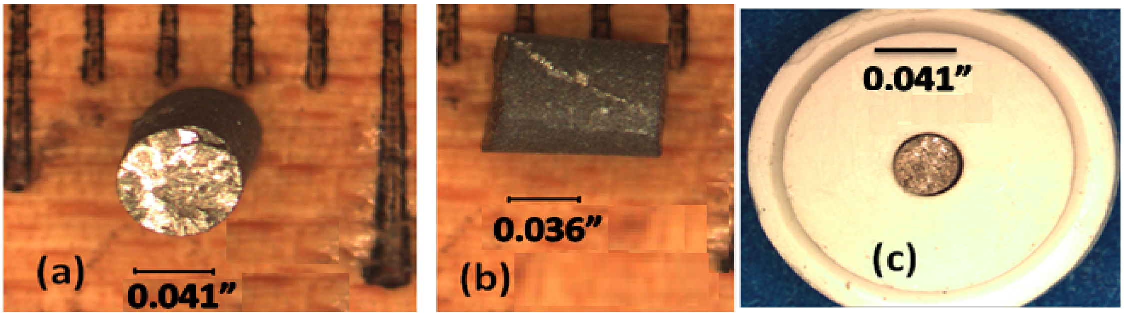

Figure 6.17 (a) and (b) Compacted sample of Fe17Si recovered from a compaction experiment; (c) recovered sample from compaction experiment is enclosed by BN capsule in preparation for an electrical resistivity experiment.

It should be noted that as the starting powder, Fe17Si was in a capsule of a length of 0.65” in order to provide enough supply for several future resistivity experiments. Low heating rates were deployed and the system was allowed to become well equilibrated as shown in Figure 6.18.

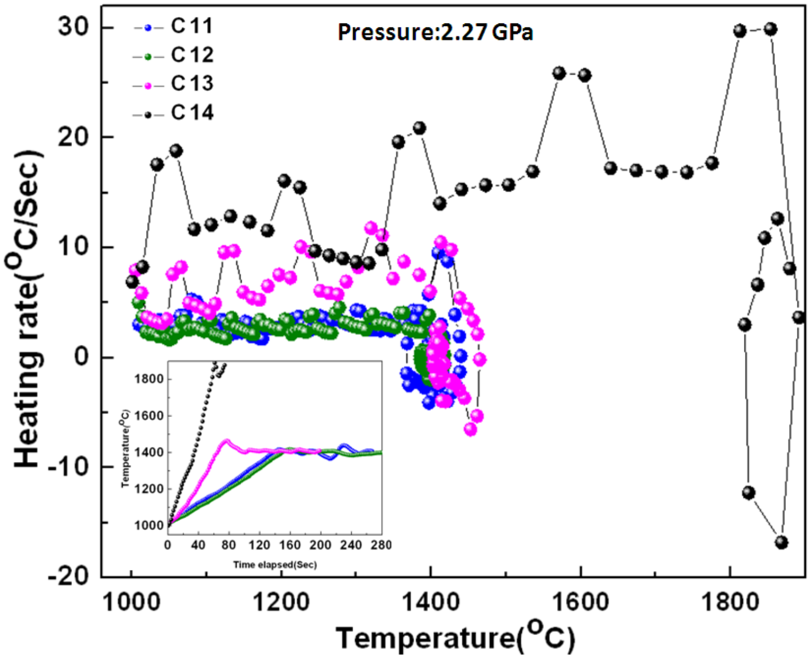

Figure 6.18 Temperature dependence of heating rates for compaction experiments.

In order to prevent the melted material from migrating and resulting in a deformed sample, a rapid quenching rate was used as shown in Figure 6.19.

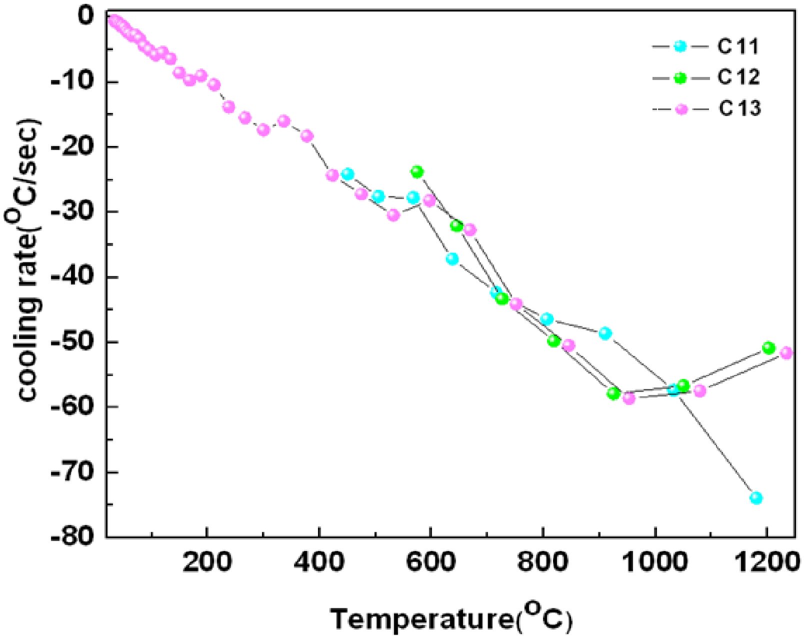

Figure 6.19 Cooling rate versus temperature for compaction experiments.

6.5 Full cube design with solid sample

Six runs were performed with solid samples which can be categorized within groups Type C and D based on modifications made and within a pressure range of 2 to 2.3 GPa. S1n notation was used to indicate S for solid sample; 1 denotes the 1000 ton press and *n* number of experiment in the series. General aspects of heating and electrical resistance measurement methods were the same as explained before in Figure 2.4. All data recording was carried out simultaneously with an Agilent 34972A digital voltmeter. Instead of using powder sample, this time a series of compaction experiments yielded solid cylindrical samples which were sectioned into disks for use in electrical resistivity cells.

6.5.1 Cell design for Type C and D

Two major designs shown in Figures 6.20 and 6.21 were tested which led to substantial differences in the quality of electrical resistivity data.

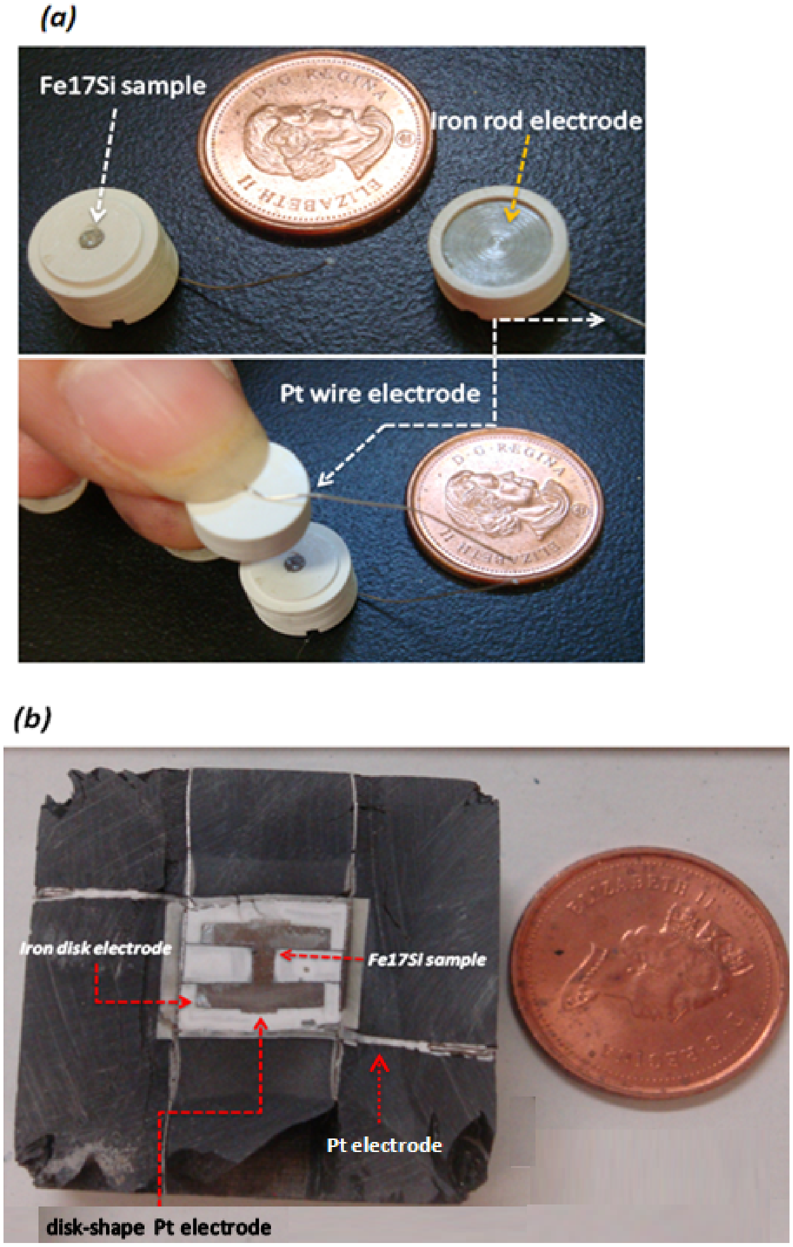

Figure 6.20 Type C design (*a*) cell assembling process; (*b*) plane view of the quenched and sectioned cell for S13 run.

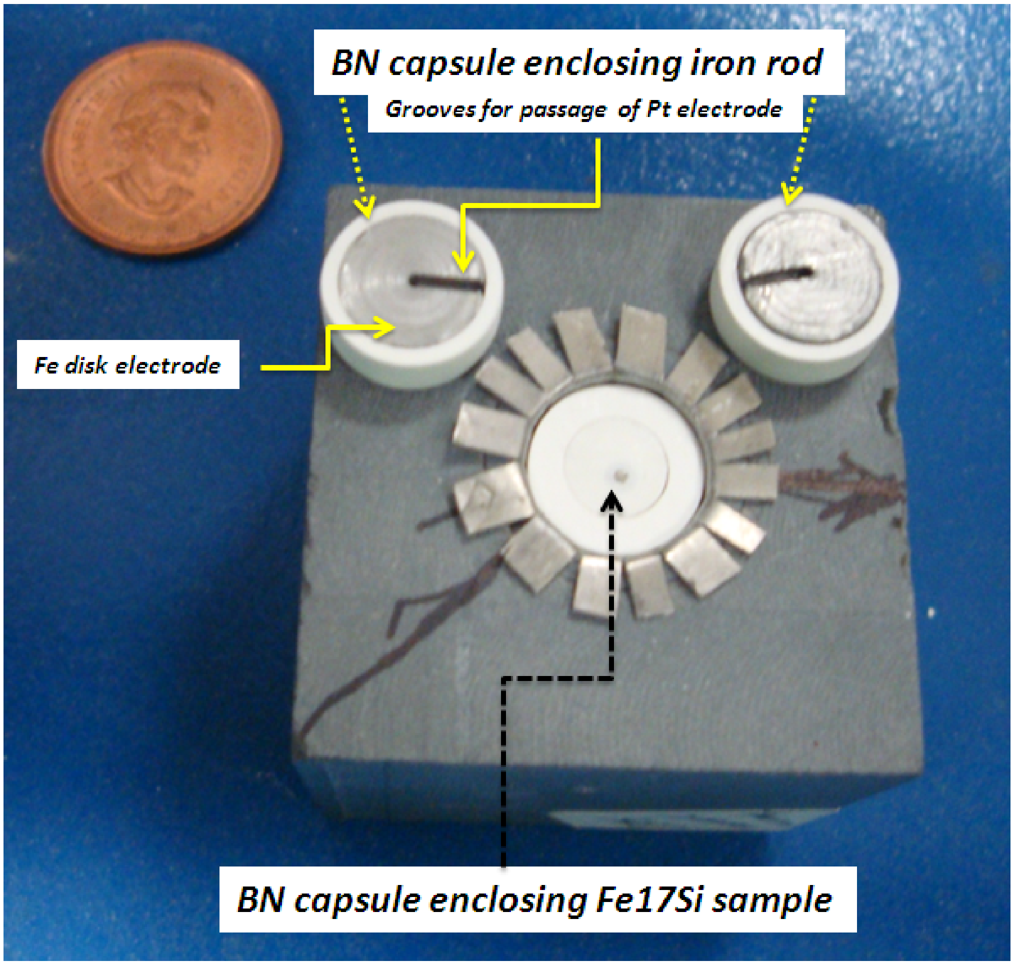

Figure 6.21 Cell constituents for Type D cell.

In Type C design (S11 to S14), a Pt wire with a disk end shape was connected to a Fe disk of typical thickness 0.05" which itself was enclosed within a BN cup. The Pt wire exits the cell through a groove made on top of the BN cup. However, in Type D design (S15 and S16), Pt wire passed through the Fe disk only half way and from the other side it sat on top of the Fe disk instead of BN cover. This modification changes the effective length of Pt wire contributed in the circuit electrical resistance and its contribution is greater in Type C than Type D design. In both types of design, the sample is in direct contact with Fe disk.

6.5.2 Results and discussion

Electrical resistivity trends for type C and D are shown in Figures 6.22 and 6.23. A variety of behaviors is noticed from S11 to S16.

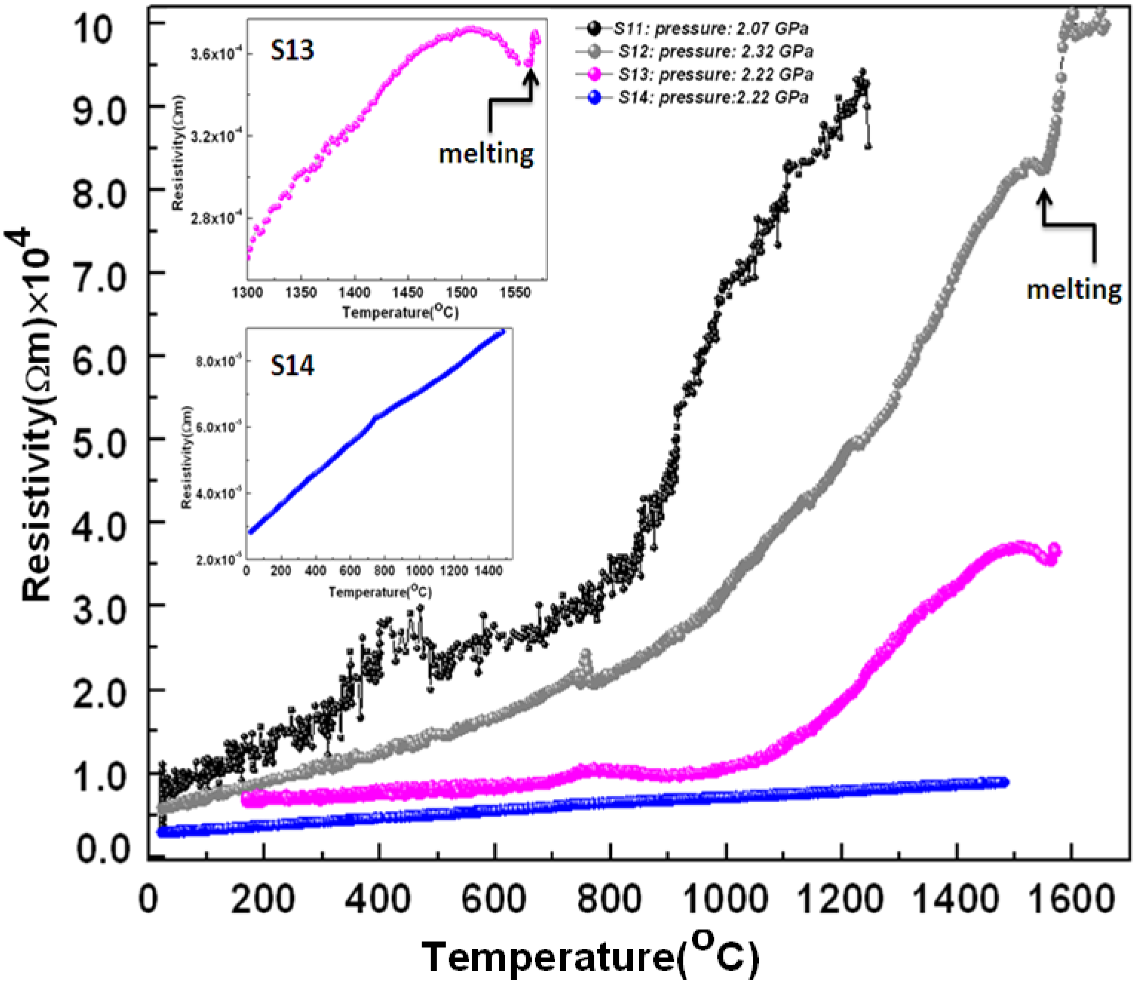

Figure 6.22 Temperature dependence of electrical resistivity for Type C design. The insert illustrates the S13 and S14 resistivity results. Resistivity scale indicates that all plotted values have already been multiplied by 10^4.

As is clear from the plotted results, there is a continuous decreasing resistivity trend from S11 to S16 for the room temperature values up to one order of magnitude difference between S11 and S16. However, the feature worth drawing attention to is the very pronounced peak around 800°C in almost all of them with the exception of S11 where it appears around 400°C. Above 800°C, resistivity values show a very different pattern. S12 and S13 resistivity values are increasing with a very steep slope and have a Fe-like melting signal between 1550°C to 1560°C. However, S14 resistivity values keep increasing in an almost monotonic fashion with temperature, without exhibiting any noticeable melting signature but the recovered sample showed evidence of melting.

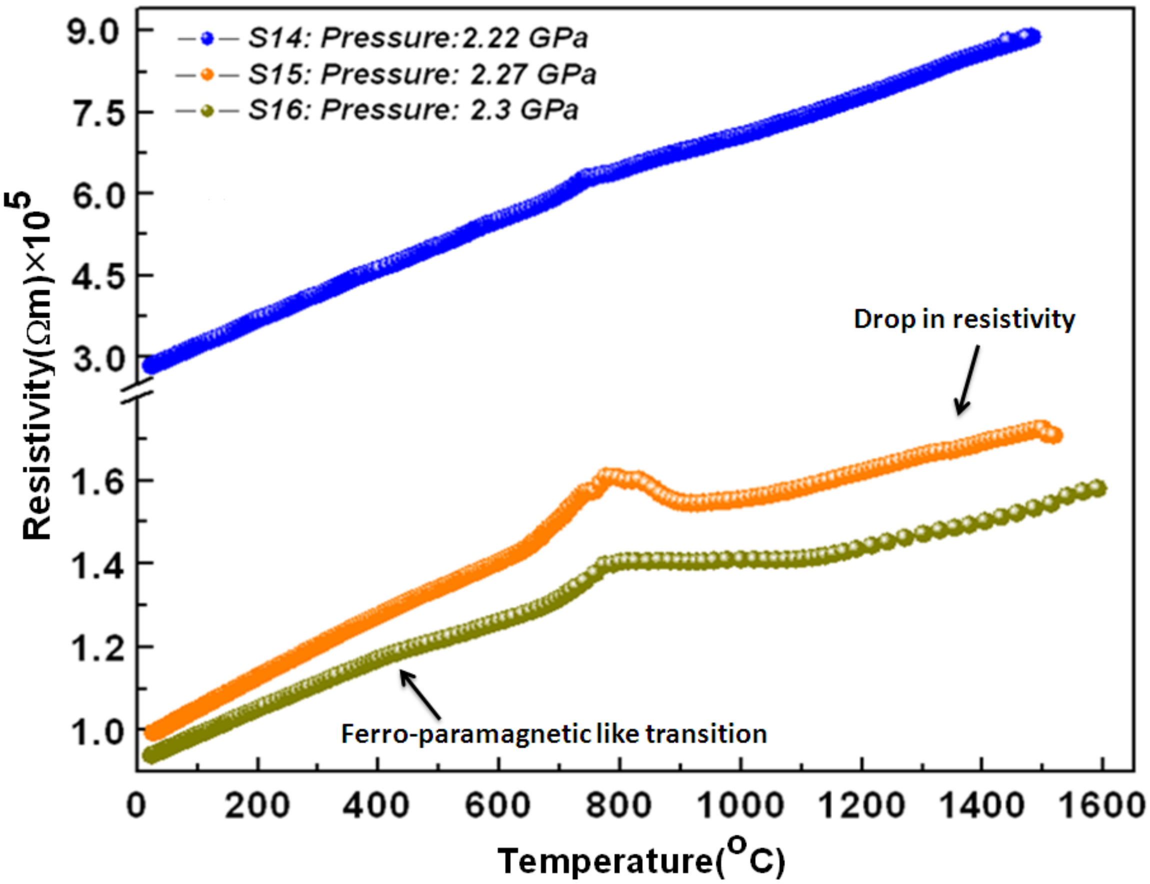

Figure 6.23 Type D experimental results of S15 and S16 with a comparison with S14 (Type C) electrical resistivity. Resistivity scale indicates that all plotted values have already been multiplied by 10^5.

S15 and S16 show almost identical trends to S14 except they have a clear slope change before the 800°C anomaly which appears to be a Fe-like demagnetization signal. The S16 kink at~400 °C is the clearest one for all S1n runs. Another significant feature specific to S15 and S16 is that, *ρ*(*T*) values show a kink with a drop for S15 and a slight slope change for S16 around of 1335 to 1354°C. This kink is more obvious in the dρ/dT plot in Figure 6.24.

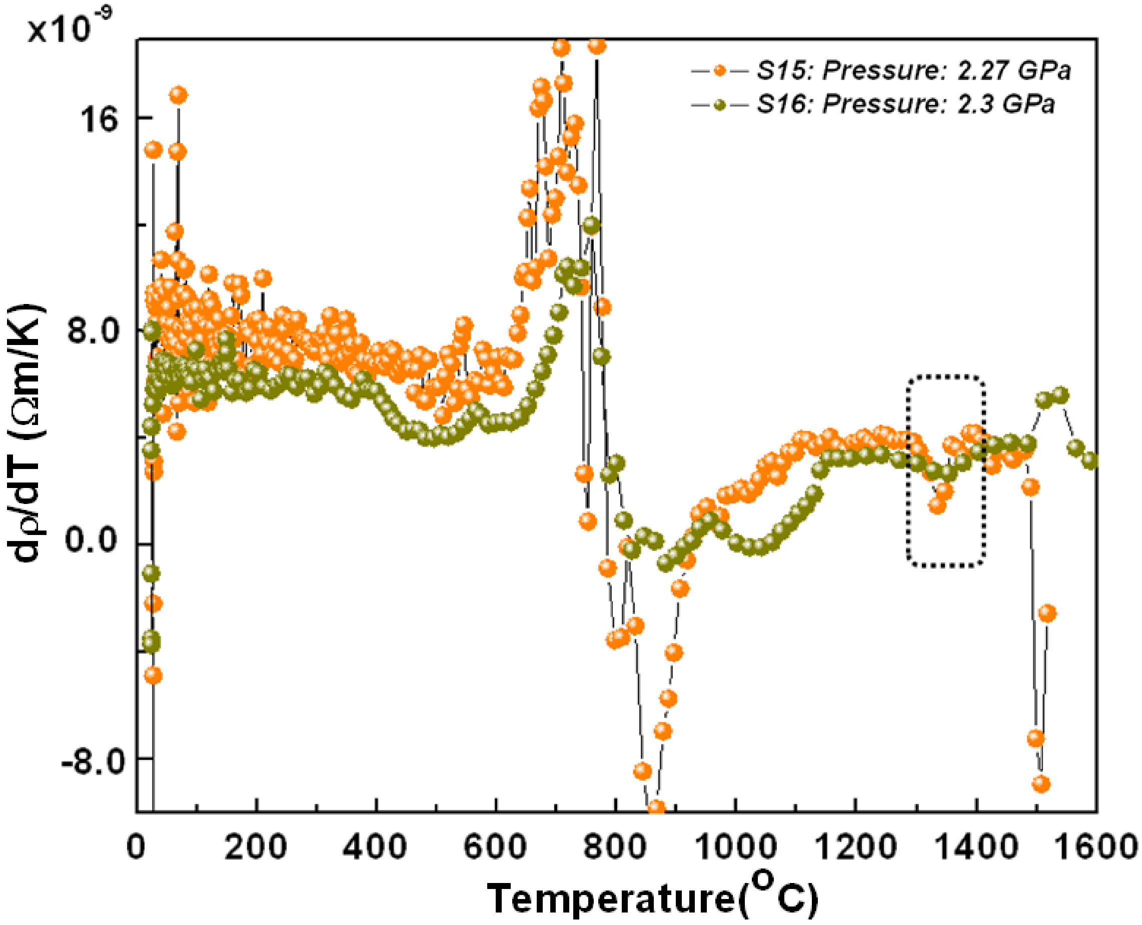

Figure 6.24 First derivative of resistivity of Fe17Si against temperature for S15 and S16 experiments. The slope anomaly around the expected melting temperature is obvious inside the dashed box.

6.5.2.1 Chemical contamination

From each of the Type C and D groups, one recovered sample was selected to be analyzed by EMP (S13 and S15). As the results in Figure 6.25 as well as in Table A7 in Appendix A show, S13 suffers from Fe contamination which leaves the quenched sample as an Fe- rich FeSi system with 4-5wt%Pt.

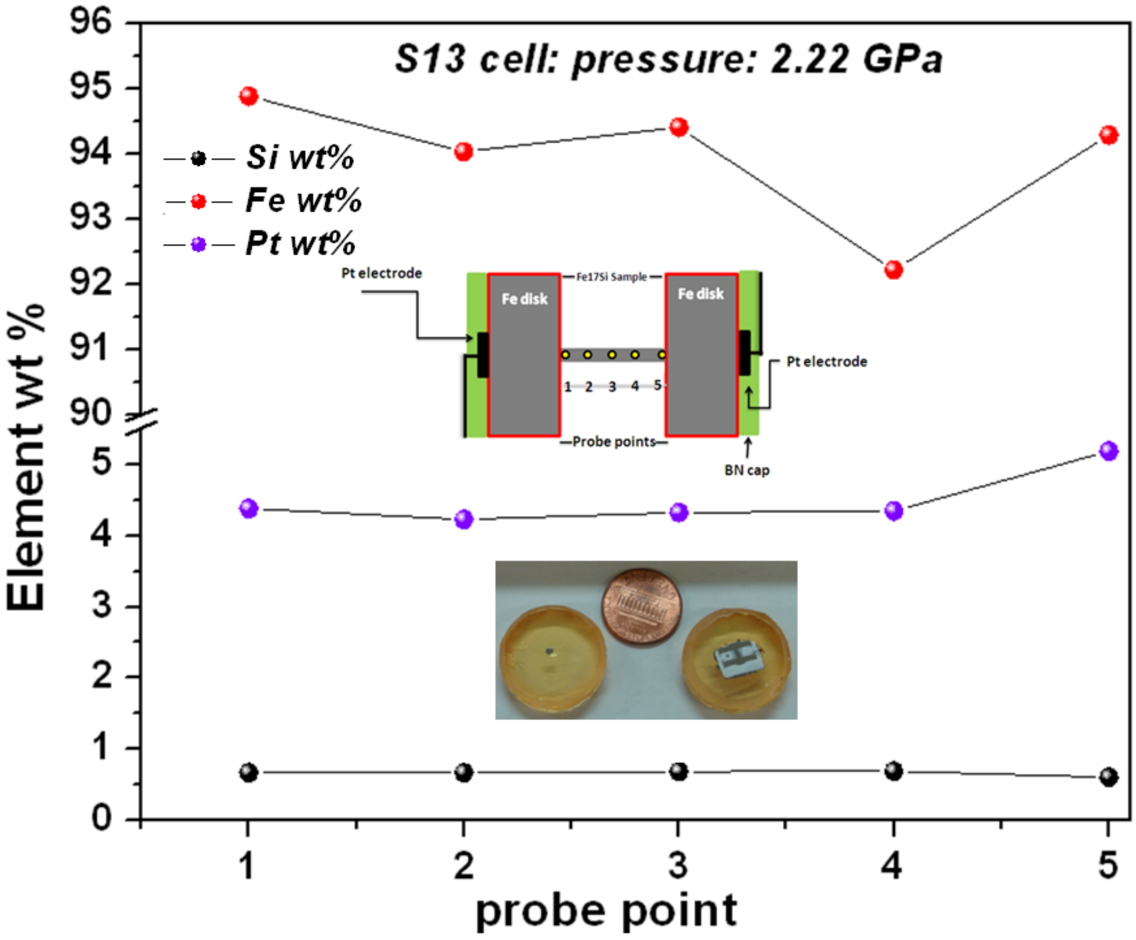

Figure 6.25 EMP results for S13 (Type C design).

According to Figure 6.26 and also Table A8 in Appendix A, S15 appears to have been well protected against electrode material diffusion.

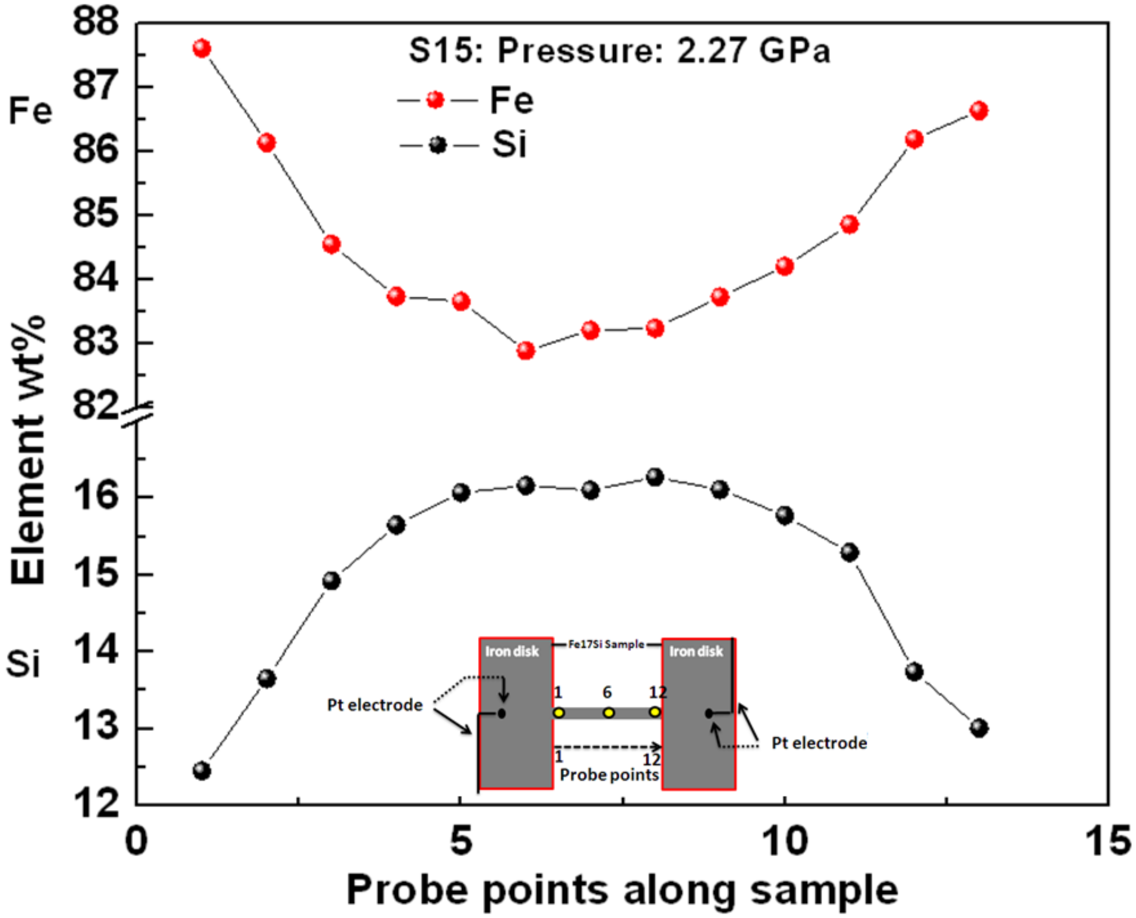

Figure 6.26 EMP results for S15 (Type D design).

Figure 6.27 illustrates the difference between the heating rate of contaminated S13 with an average value of 1°C/sec and relatively chemically clean S15 sample with an average heating rate of 5°C/sec. However, there are still some puzzling features regarding the difference in resistivity order among chemically contaminated and less contaminated cells at high temperature that need to be addressed.

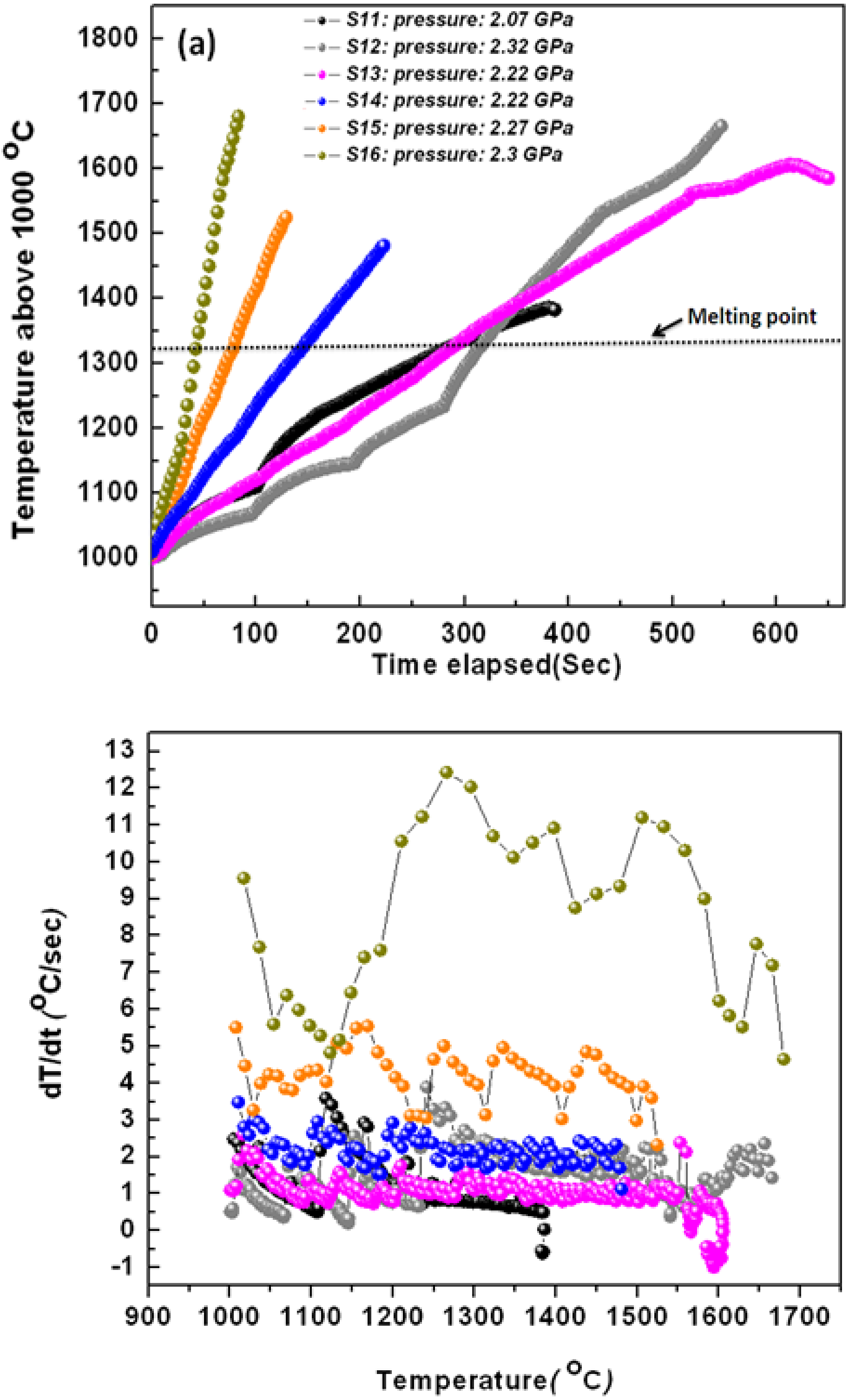

Figure 6.27 Comparisons between Type C and D cells for (a) time spent above 1000°C, and (b) heating rates.

6.5.2.2 Circuit geometrical contribution

In order to resolve the above mentioned puzzling behavior of $\rho(T)$ trends, a detailed consideration was made for the geometrical characteristics of samples in Type C and D (Table 6.2). Calculating the G-factor, as described in Chapter 4, for all S1n experiments gives a quantitative assessment of the effect of electrodes on the recorded electrical resistance. The G factor for S13 differs from that of S15 and S16 by a significant amount ($G_{S13}/G_{S16} \sim 36$). This can explain the higher values of $\rho(T)$ for S13. The S14 run is expected to have higher Fe contamination than S15 and S16 according to its heating rate, but it still shows higher $\rho(\mathrm{T})$ values by a factor of 3 at both low and high temperature. The ratio of G factors G_{S14}/G_{S15} appears to cause the significant difference between $\rho(T)$ values of S14, S15 and S16. Therefore, it can be concluded that even with a fast heating rate, and low contamination, geometrical characteristics of the electrical circuit inside the cell play a very crucial role in masking the real electrical resistivity values as well as their temperature dependence.

Table 6.2 Summary of geometrical factors for S1n samples in the 1000 ton press.

	Design Exp.	Pressure (GPa)	G-factor at room T	Resistivity (Ωm)
Type C	S11	2.07	22.4	1.12×10^{-4}
	S12	2.32	26.0	9.00×10^{-5}
	S13	2.22	19.3	6.90×10^{-5}
	S14	2.22	14.0	3.70×10^{-5}
Type D	S15	2.27	0.66	1.13×10^{-5}
	S16	2.30	0.54	1.05×10^{-5}

6.6 Full cube, solid, lateral sample design

Notation L1n (*n*: 1 to 5) is applied to each of five experiments using a “lateral design” in the 1000 ton press. Looking for a design devoid of any small diameter wire contribution to the electrical circuit, a “lateral design” was tested. Pt was excluded from the system as an electrode material because Pt contaminates the sample and makes a ternary system of Fe-Si-Pt which is a less-investigated and therefore challenging chemical system for which to make corrections. Whereas, Fe electrode may “contaminate” the system by reducing the Si content, it does not add a new chemical component to the system. In the “lateral design”, two thick horizontal (with respect to the vertical axis of the Nb furnace) Fe rods (0.05” in diameter) make contact with a horizontal solid Fe17Si sample. Both the sample and Fe rod are shielded against any contact with the Nb furnace by BN sleeves as shown in Figure 6.28. This way the entire length of sample is placed within the central plane and the problem of any thermal gradient along the vertical axis of the furnace will be minimized. However, at the same time, it is recognized that the thick Fe rod can act as a heat sink at the central plane for setting up a temperature gradient along the horizontal axis of the Fe sample system. A very fast heating rate was needed to mitigate against this.

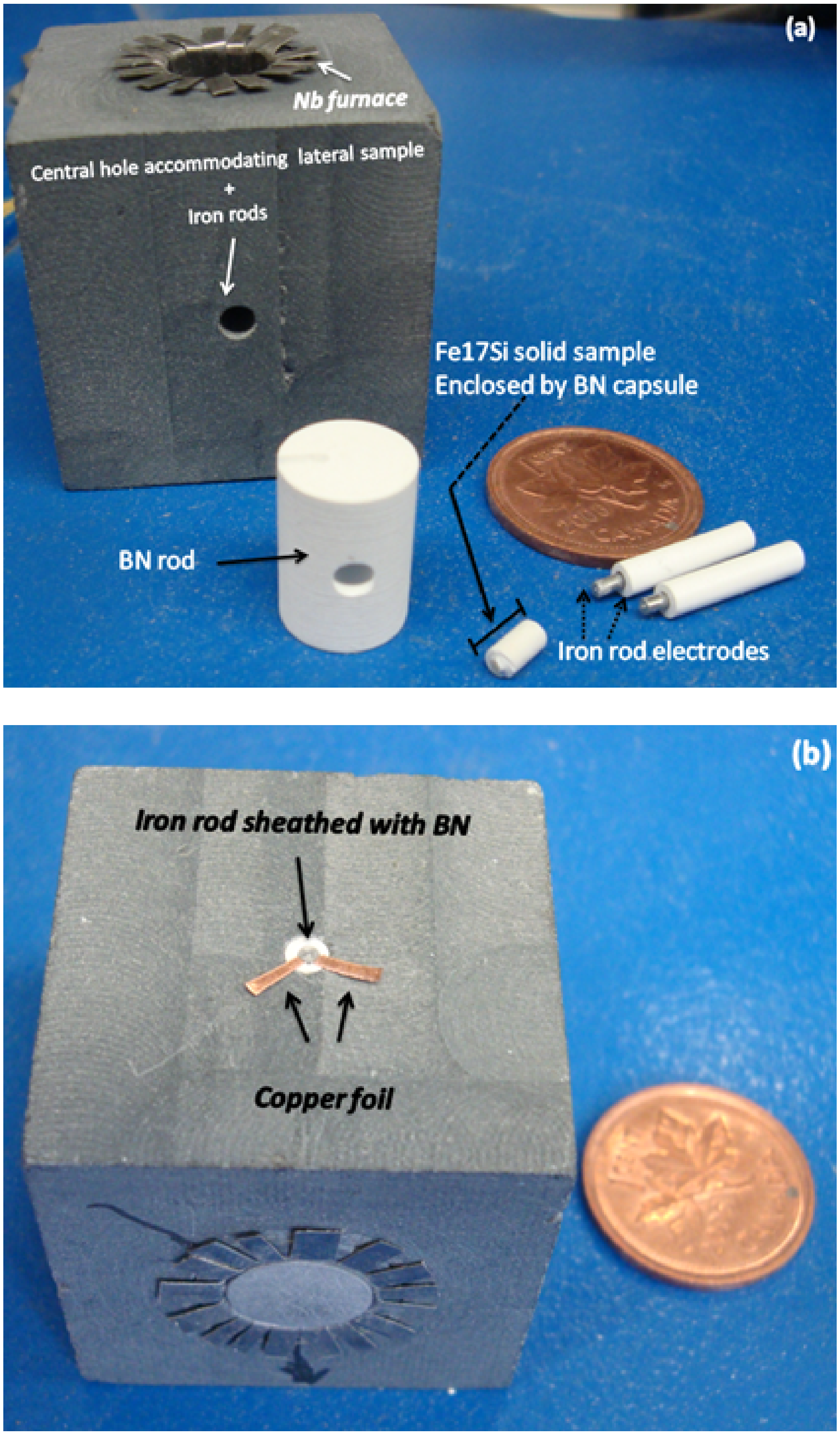

Figure 6.28 Lateral design cell: (a) constituents before assembling; (b) view of the assembled cell.

6.6.1 Chemical contamination and heating rate

Figure 6.29 illustrates a comparison of heating rates of L1n experiments with all previous S1n runs and it proved that this design was the most successful in terms of heating rates.

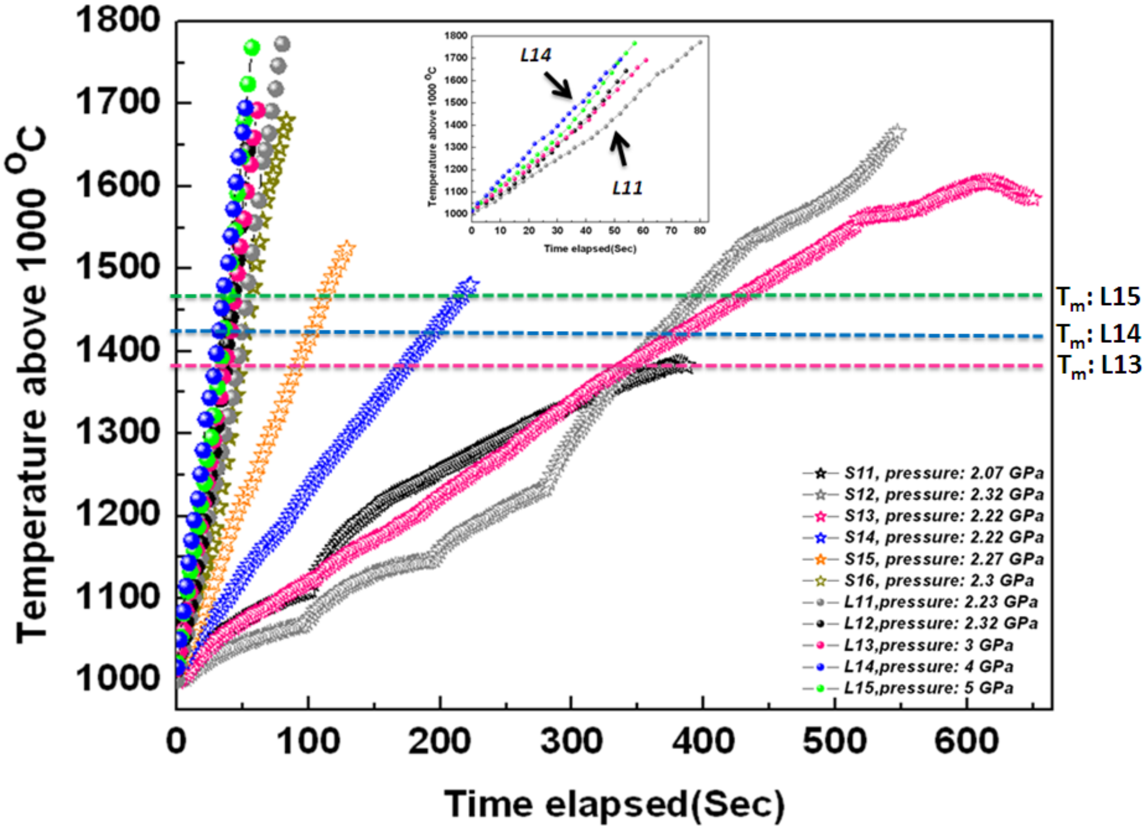

Figure 6.29 Time spent above 1000°C. A comparison between L1n and S1n experiments. The insert illustrates a magnified view of the heating rate of L1n series.

From the EMP results shown in Appendix A, Tables A9-11, and also from Figure 6.30 it was clear that except for the L11 run, which had a migration of Si into pure Fe to the extent that it left 10-12wt% Si within the quenched sample, the rest are relatively well protected against chemical contamination. The low heating rate and high temperature of L11 made it the most susceptible to contamination.

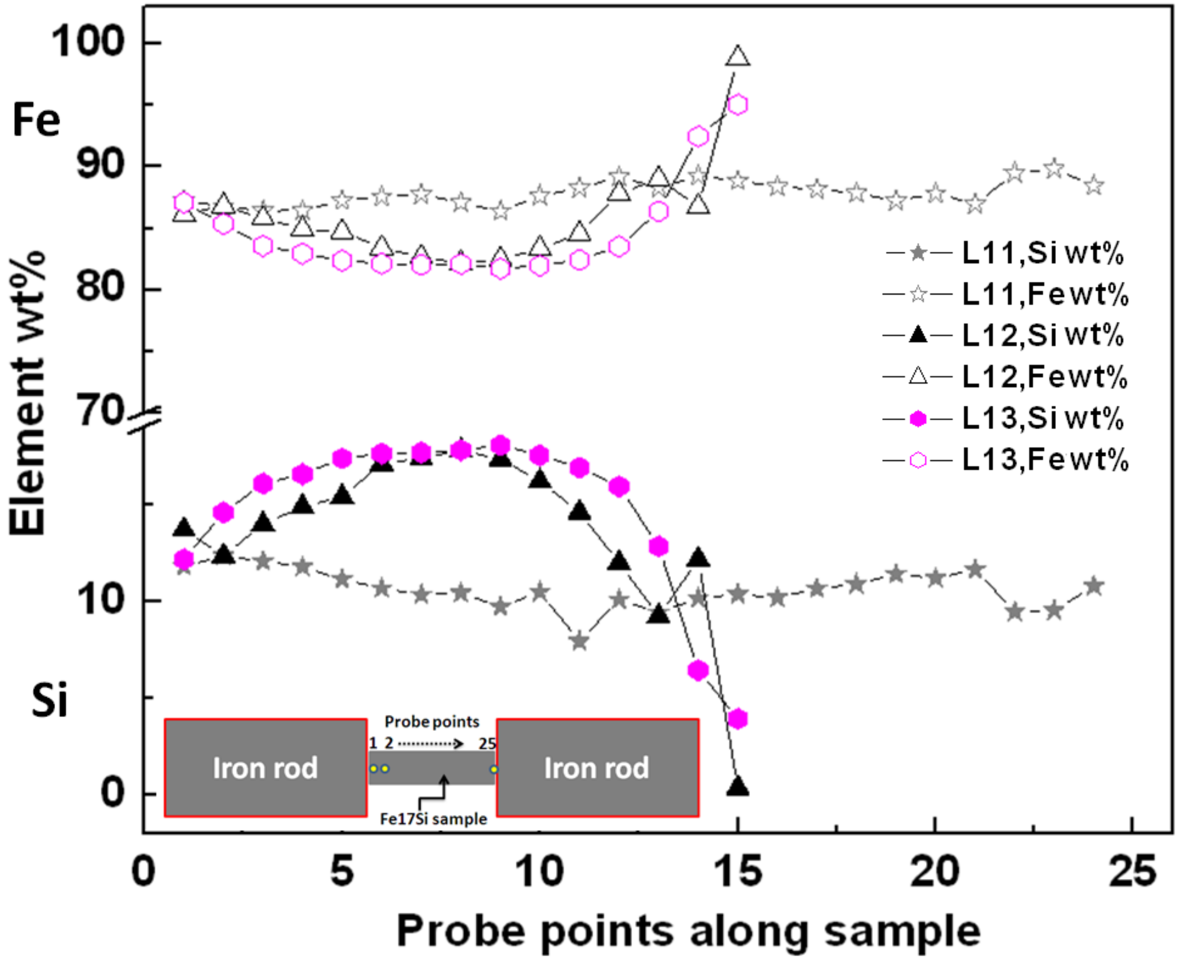

Figure 6.30 EMP results for L11, L12 and L13 experiments.

6.6.2 G-factor value

Table 6.3 illustrates the G-factor values for L1n series.

Table 6.3 G-factor summary for L1n series.

Design Exp.	Pressure (GPa)	G-factor at room T
L11	2.23	0.012
L12	2.32	0.05
L13	3	0.067
L14	4	0.048
L15	5	0.038

In view of the reduced contribution of the electrode resistances, the G-factors from all experiments (P2n, P1n, and S1n and L1n series) are collected in Figure 6.31.

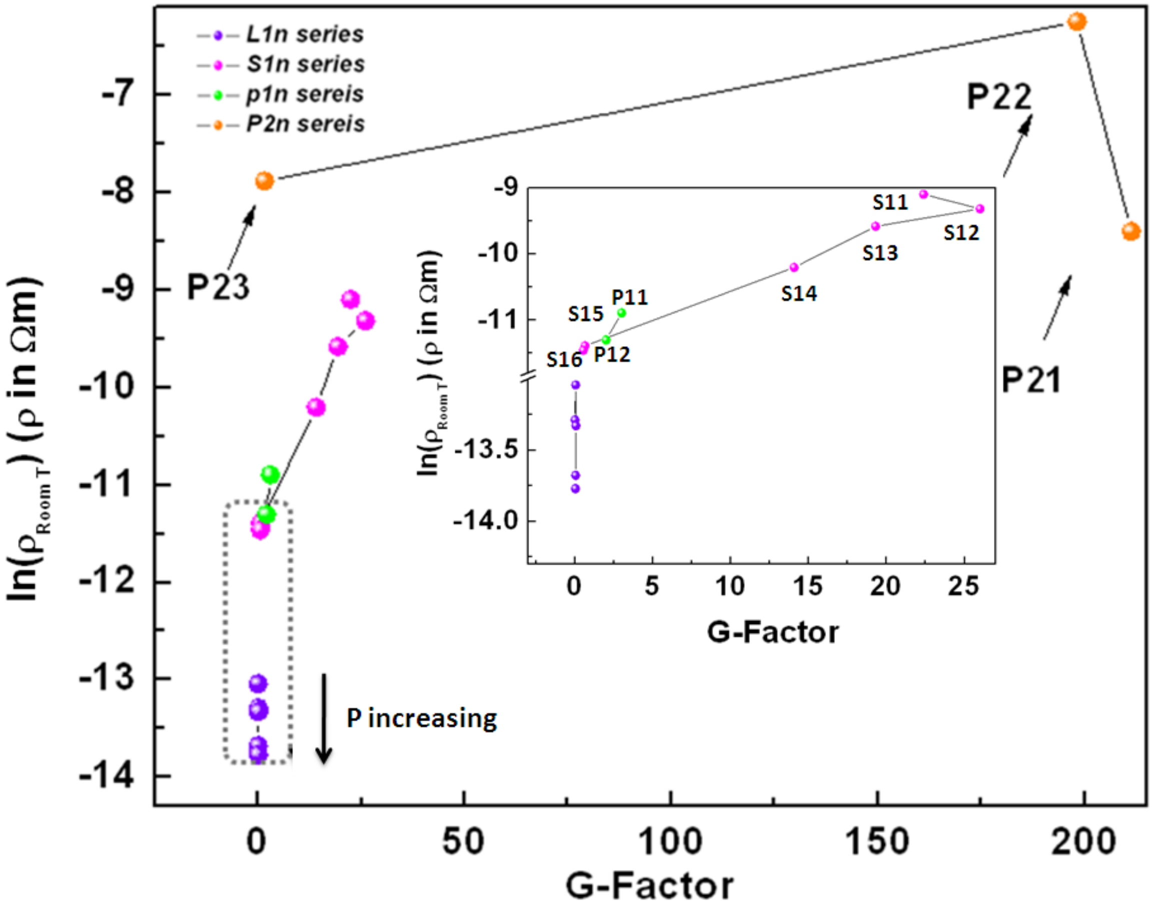

Figure 6.31 G-factor comparisons for all Fe-Si designs within the present study. Dashed box indicates the designs with approximately the same degree of low contamination. The insert gives a magnified view for S1n, P1n and L1n series. The insert illustrates the G-factor values in terms of pressure for L1n series.

From this figure, it is obvious that the *G* factor has a strong and direct relation to the room temperature resistivity for all experiments. More importantly, the "lateral design" has proven to be the most successful one to decrease the contribution of electrode resistance to the measured resistance values. The dashed box in Figure 6.31a includes ln$\rho(T)$ data from experiments with different designs but according to the EMP analysis, they all have very similar chemical composition of high Fe and very low (<0.1wt%) to no

Pt contamination from electrodes into Fe17Si sample. Therefore, having approximately the same composition, *G* factor has made a significant difference in the order of measured electrical resistivities with the L1n series showing the lowest resistivity among all and the most trustworthy signal associated with Fe-Si sample.

6.6.3 Electrical resistance correction process for L1n series

In order to isolate the resistance signal from the sample in the centre of the lateral design, a three-step correction was applied as follows:

1. Using the same "lateral design", a separate experiment with one continuous long piece of Fe was carried out at 2.23 GPa (L16). The temperature dependence of electrical resistance for L16 is shown in Figure 6.32.

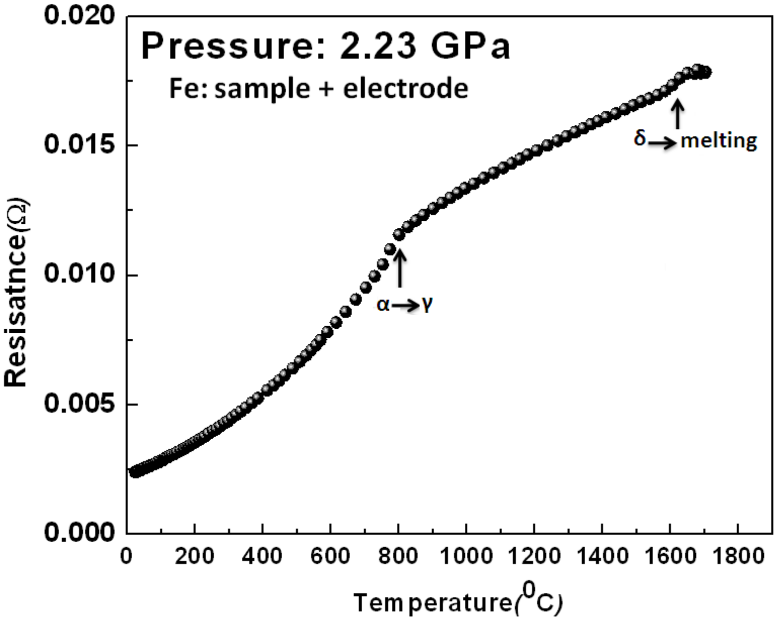

Figure 6.32 Temperature dependence of resistance for Fe in experiment L16.

2. Using pure Fe resistivity curve at 2.48 GPa as reference data (Secco and Schloessin, 1989), the electrical resistance contributions of inside-furnace,

hot zone Fe electrode, (Figure 6.33), was calculated for all L1n series experiments.

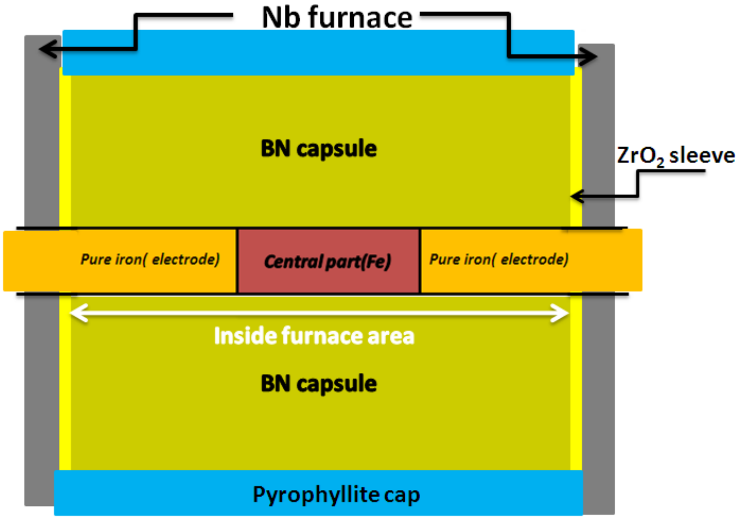

Figure 6.33 Schematic illustration of the inside furnace area for L1n experiments.

3. Following step two, the effect of electrode resistance contribution from the hot zone (inside-furnace) was calculated for the L16 experiment. This made it possible to estimate the cold zone Fe electrode resistance. For each of the L1n series runs, hot (inside-furnace) and cold (outside furnace) zone electrode contributions were calculated accordingly and the total electrode resistance was subtracted from the actual measurements. Therefore, the remaining value is, to a good approximation, the resistance signal stemming solely from the Fe17Si sample in the centre of the cube. As an example, Figure 6.34 illustrates the successive corrections applied on run L11.

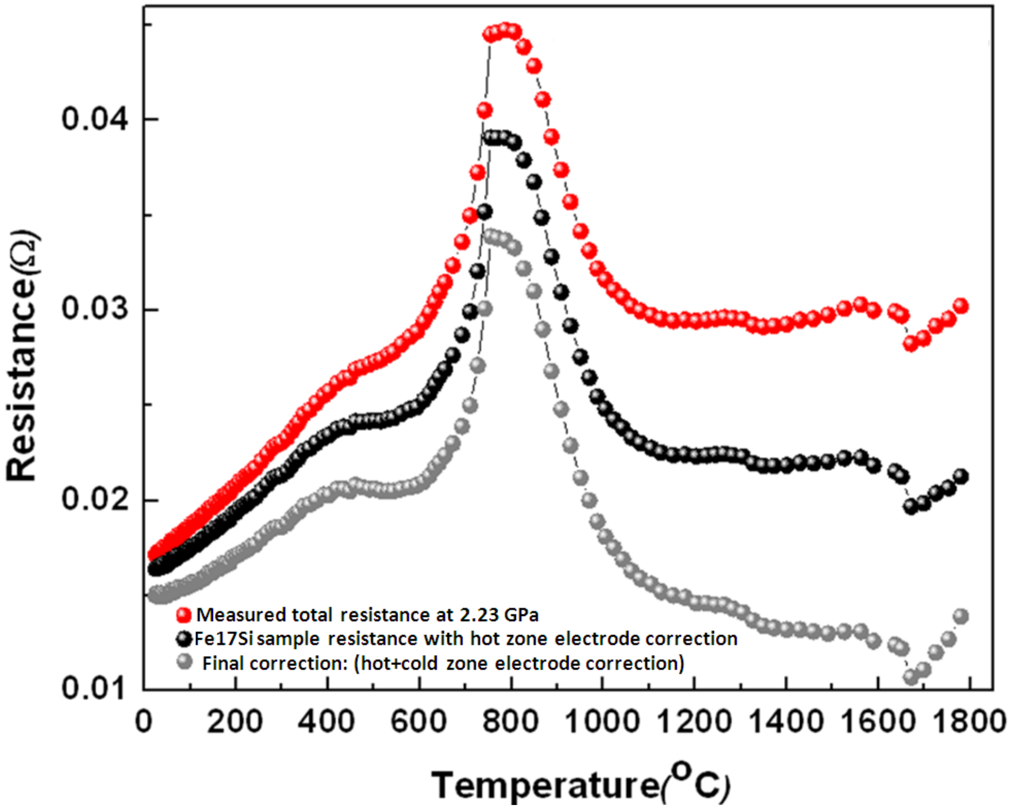

Figure 6.34 The Fe electrode correction result for run L11.

6.6.4 Electrical resistivity results and discussion

All $\rho(T)$ plots at pressures from 2.23 GPa to 5 GPa illustrated in Figure 6.35, were corrected for the effect of Fe electrode contribution as described above.

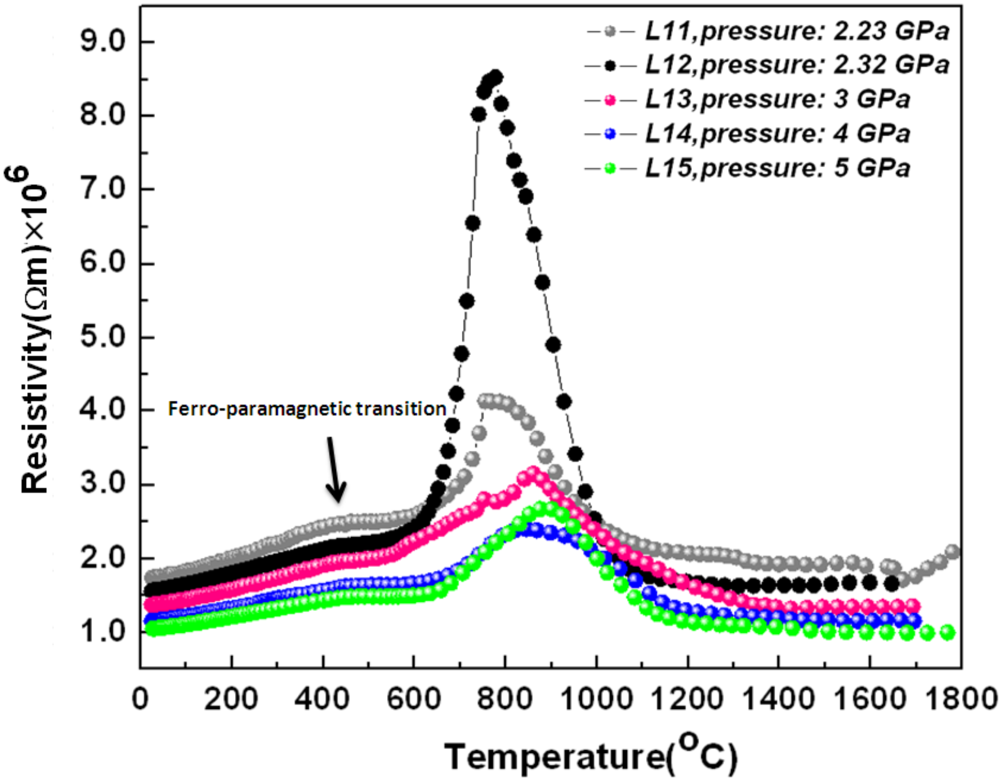

Figure 6.35 Temperature dependence of electrical resistivity of Fe17Si for corrected L1n series. Resistivity scale indicates that all plotted values have already been multiplied by 10^6.

The behavior and the order of $\rho(T)$ data are very different from previous experiments (P2n, P1n, and S1n). At least three main slope anomalies are recognizable: i) a Fe-like ferromagnetic-paramagnetic transition at 400-500°C; ii) a peak around 800-900°C and, iii) a sharp drop (L11 and L15) or smaller drop in resistivity (L12, L13 and L14) around the expected melting temperature at the corresponding pressures. Each of these features will be discussed individually in a more detail.

6.6.4.1 Room temperature resistivity values of L1n experiments

Attempts were made to summarize the very scarce available data on high pressure electrical resistivity measurements for Fe-Si alloys in order to make comparison between them and the present research values at room temperature. The results are illustrated in Figure 6.36.

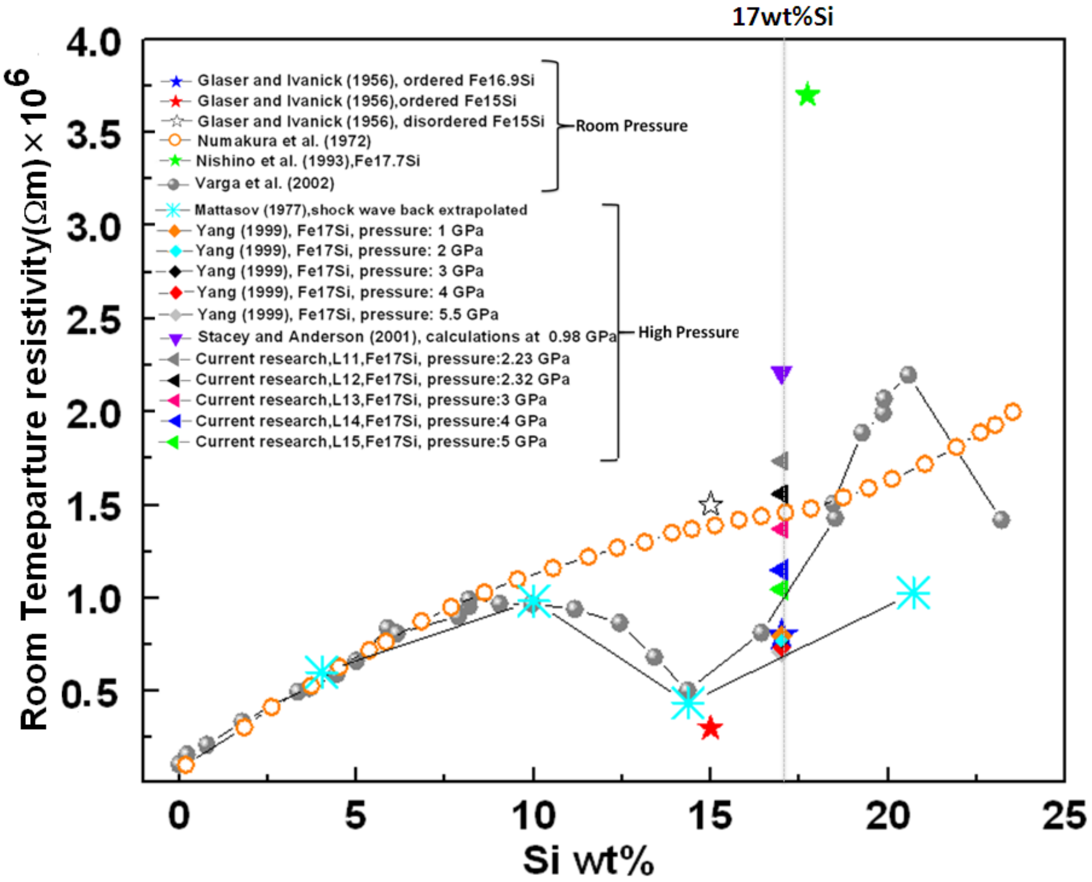

Figure 6.36 Dependence of room temperature electrical resistivity of Fe silicon alloys on Si wt% concentration. Resistivity scale indicates that all plotted values have already been multiplied by 10^6.

Pressure is believed to have a suppressing effect on the resistivity values for Fe alloys. This feature is clearly shown for Fe17Si in Figure 6.37. The L1n room temperature values line up in a descending trend with pressure. Experimental results at 1 GPa to 5 GPa by Yang (1999) also exhibit the same decreasing trend with pressure as shown in Figure 6.37.

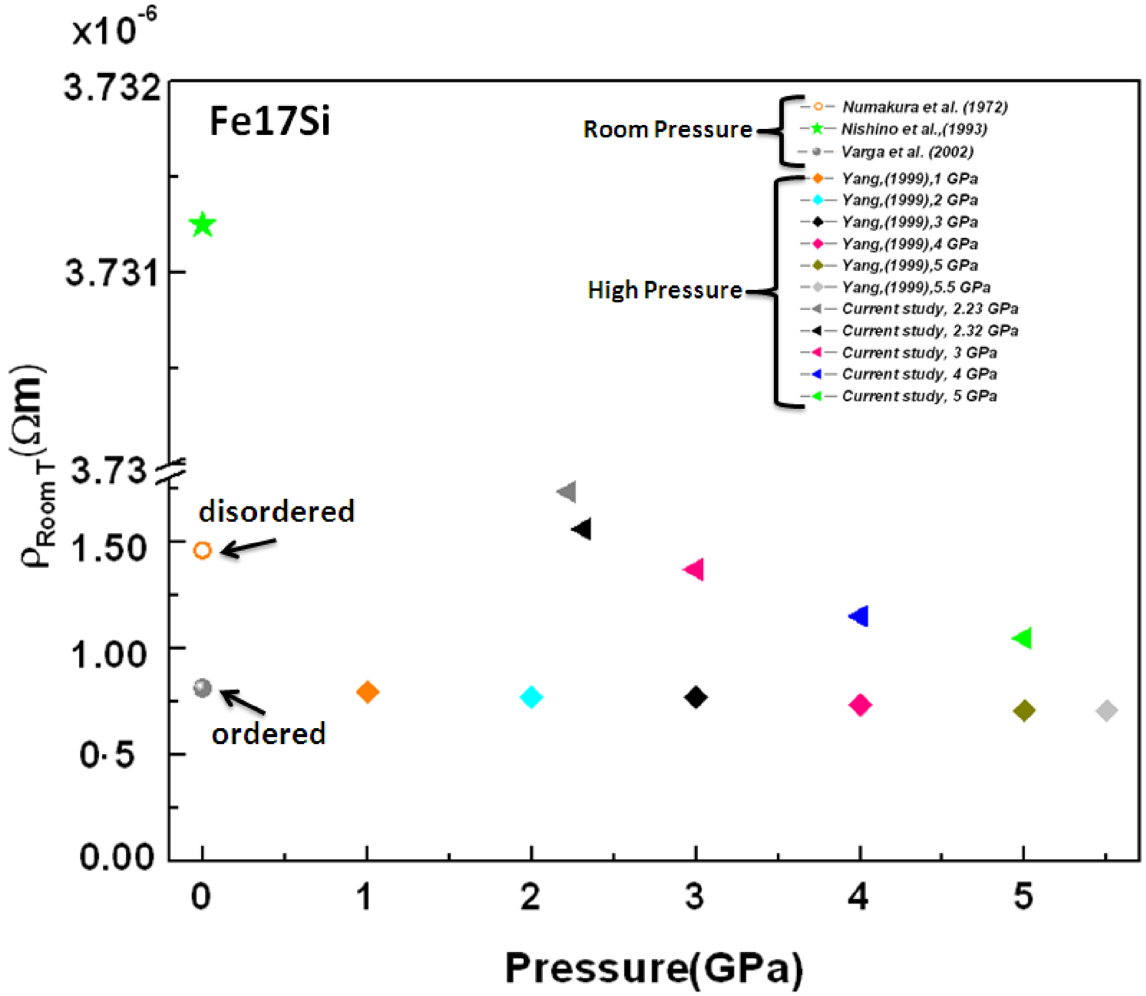

Figure 6.37 Summary of pressure dependence of electrical resistivity of Fe17Si at room temperature from literature as well as the current study data.

It should be noted that, Yang (1999) values are very close to the room pressure ordered resistivity data which is similar to the 5 GPa data point in the present study. Strictly speaking, Yang (1999) high pressure data points plot below the room pressure ordered values, while most of the values measured in this study plot closer to the disordered room temperature values except for the 5 GPa datum. Considering the above mentioned discussion in addition to the high quenching rate that was used for the sample preparation within the present work (60-70^{o}C/sec) , it seems reasonable to conclude that all samples in the current study were mostly disordered and consequently of higher resistivity value compared to Yang (1999) data. Room P, T results of electrical resistivity of 17.7wt%Si from Nishino et al. (1993) is also much higher than what has been suggested by Numakura and Tsugawa (1972) for disordered Fe-Si. The cooling method in Nishino et al. (1993) research seems to be slow cooling. Therefore, it is unclear as to why their room temperature electrical resistivity value is so high.

Mooij (1973) predicted that for any metallic system, there is correlation between the electrical resistivity and TCR values. Metallic systems undergo saturation within a universal range of 1.5-2 Ωm, and the TCR values change sign from positive to negative through a zero cross-over point. Figure 6.38 shows the trend defined by many metallic systems. Room temperature TCR data at high pressures from the current study are also plotted in Figure 6.38. The high pressure data resistivity values ranges from 1.2×10^{-6} to1.5×10^{-6} Ωm. This is noteworthy that the high pressure TCR data changes sign at exactly the same resistivity region as do the many metallic systems in the Mooij (1973) data. There are several features of this plot that need explanation. The Mooij (1973) data represent many different metallic compositions and so the resistivity values vary accordingly to composition effects and scattering mechanisms due to structure and impurity scattering. The change in phonon scattering due to thermal fluctuations of the atom is contained in the TCR value, both magnitude and sign. The cross over from

TCR>0 to TCR<0 is thought to be due to a saturation effect caused by a decrease in the electron mean free path from a length Λ greater than the interatomic spacing a_o, to a length approximately equal to the interatomic spacing respectively. The regime where TCR<0 may have similarity with of an electron hopping mechanism of conduction, where thermal fluctuations assist the motion of "quasi-localized" electrons. Regardless of whether or not there is a change in conduction mechanism, and if so what mechanism is, it is interesting to note that, to the author's knowledge, this is the first report of a cross over in TCR sign caused by pressure as discussed within the resistivity saturation model. In terms of the Ioffe-Regel criteria where saturation is achieved where $\Lambda \sim a_o$, the effect of pressure on reduction of ao appears to be a lowering of the resistivity value at which saturation can be reached.

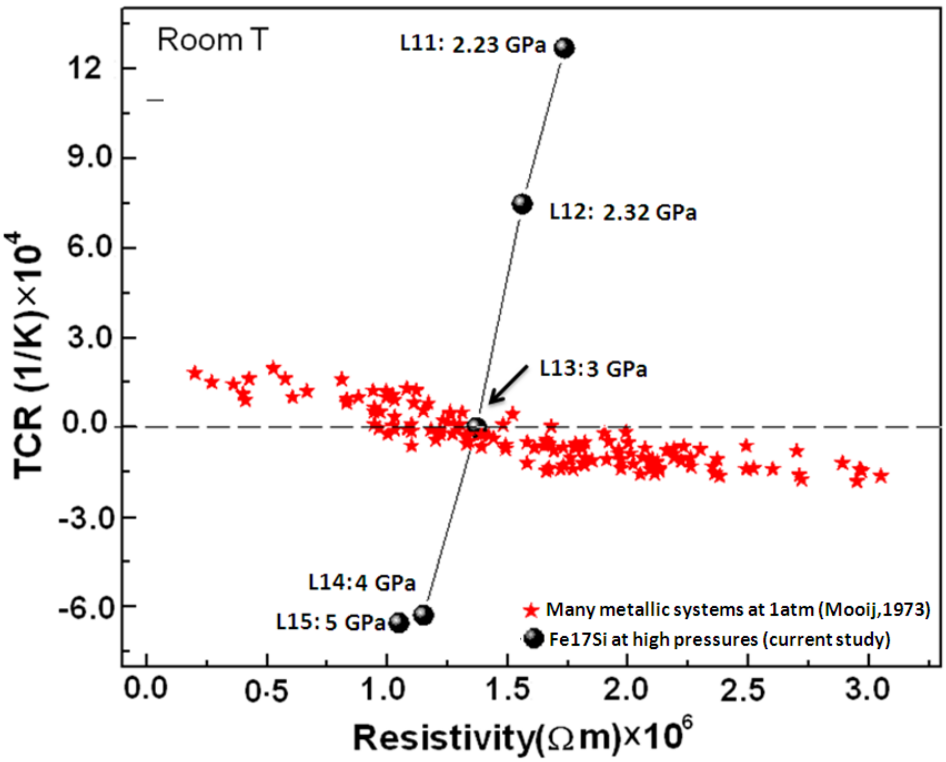

Figure 6.38 Correlation between TCR and electrical resistivity at room temperature for many different metals and metallic alloys at 1 atm (Mooij, 1973) and for Fe17Si at high pressures (this study). TCR scale indicates that all plotted values have already been multiplied by 10^4.

6.6.5 Magnetic transition

It has been established that Fe-Si alloys show ferromagnetic properties up to 33 wt% Si (ordered ε-phase) (Numakura and Tsugawa, 1972). The ferro-paramagnetic transformation temperature at room pressure, drops from 780°C for pure Fe to 500°C for an ordered state of Fe_3Si at 15wt% Si and remains at 500°C for Si concentration exceeding 15wt%. As one of the few studies on high Si composition Fe alloys, Nishino et al. (1993) reported the magnetic transition shifts towards lower temperature values as the Si concentration increases from 3.65 wt% to 25 wt% as shown in Figure 6.39.

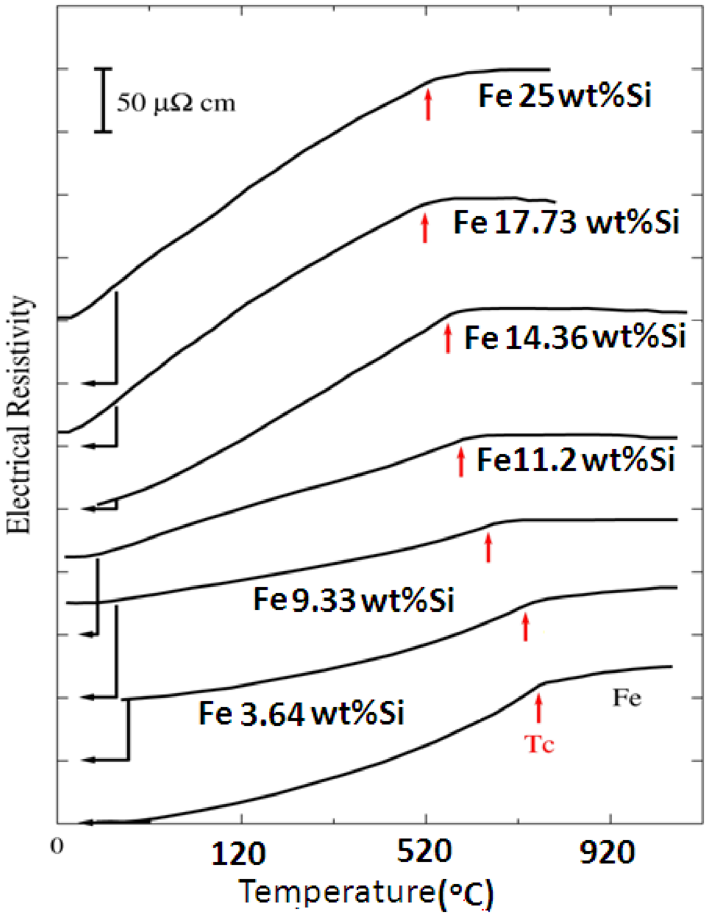

Figure 6.39 The Curie temperatures (Tc) for a range of Si compositions (after Nishino et al. 1993).

Examining the $\rho(T)$ plots for the L1n series, a magnetic transition is very clear at temperatures 435°C for L11 to 460°C for L15 as shown in Figure 6.40. It confirms that the transition temperatures show a positive pressure dependency going from low pressure to higher pressures.

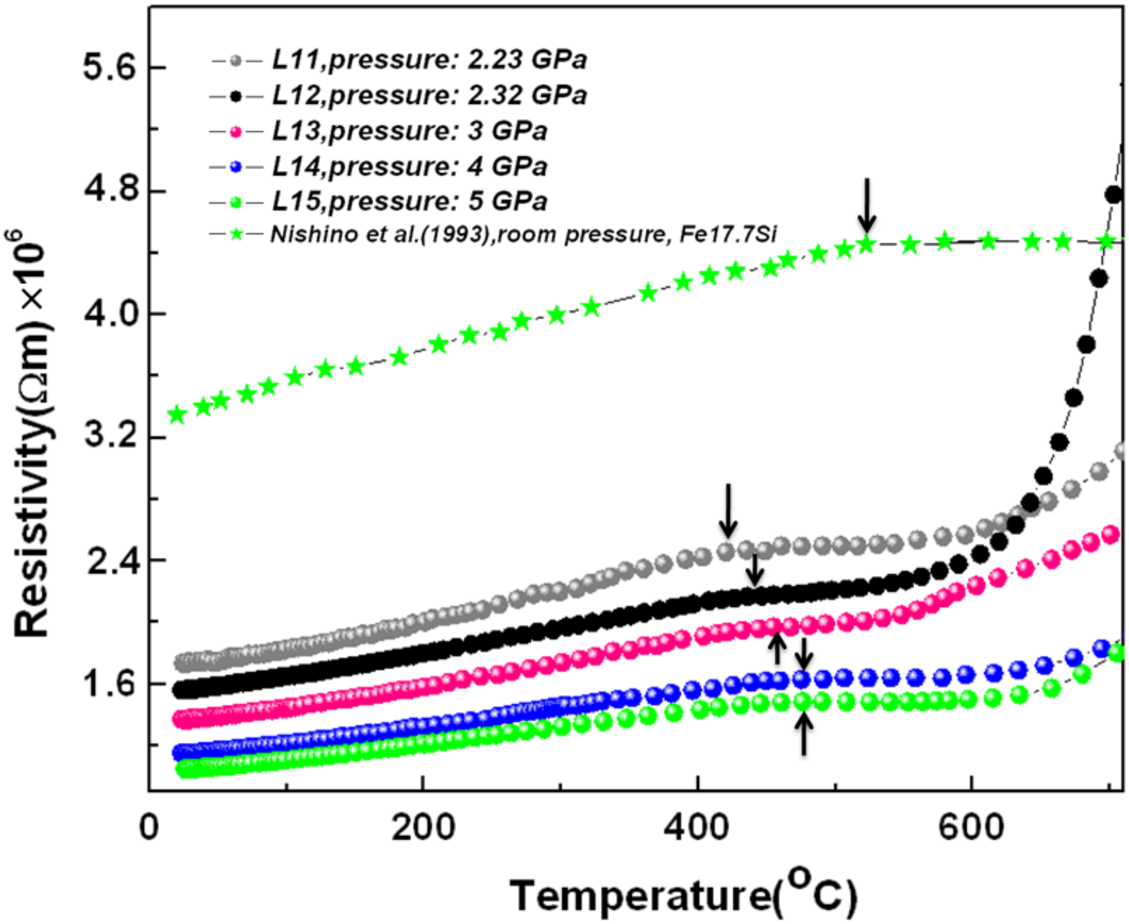

Figure 6.40 The electrical resistivity temperature dependence at magnetic transition, indicated by the arrows, for L1n series. Resistivity scale indicates that all plotted values have already been multiplied by 10^6.

6.6.5.1 Order-disorder phase change

The rapid increase in electrical resistivity following the magnetic transition is one of the striking features of $\rho(T)$ data as is shown in Figure 6.35. The magnitude of these peaks appears to be inversely dependent on pressure as shown in Figure 6.41. However, L11 and L12 results make it challenging to draw an exact conclusion. In order to characterize this anomaly with its peak moving from approximately 755°C at 2.23 GPa to 875°C at 5

GPa (the insert in Figure 6.41), it is necessary to investigate the high pressure-temperature phase diagram of Fe17Si alloy.

As was discussed in Chapter 5, close to 17.7wt% Si, the phase diagram gets very complicated and lacks sufficient data at high pressure. Inspecting the phase diagram of Fe-Si in Figure 5.1 under ambient pressure condition, for Fe17Si, it suggests transitions from $\alpha_{1+}\varepsilon$, $\alpha_{1+}\eta$ and α_1 structure as one moves from room temperature up to melting temperature. Pressure can shift the phase regions in a certain direction or change its extent which can add to the complexity of the phase identification.

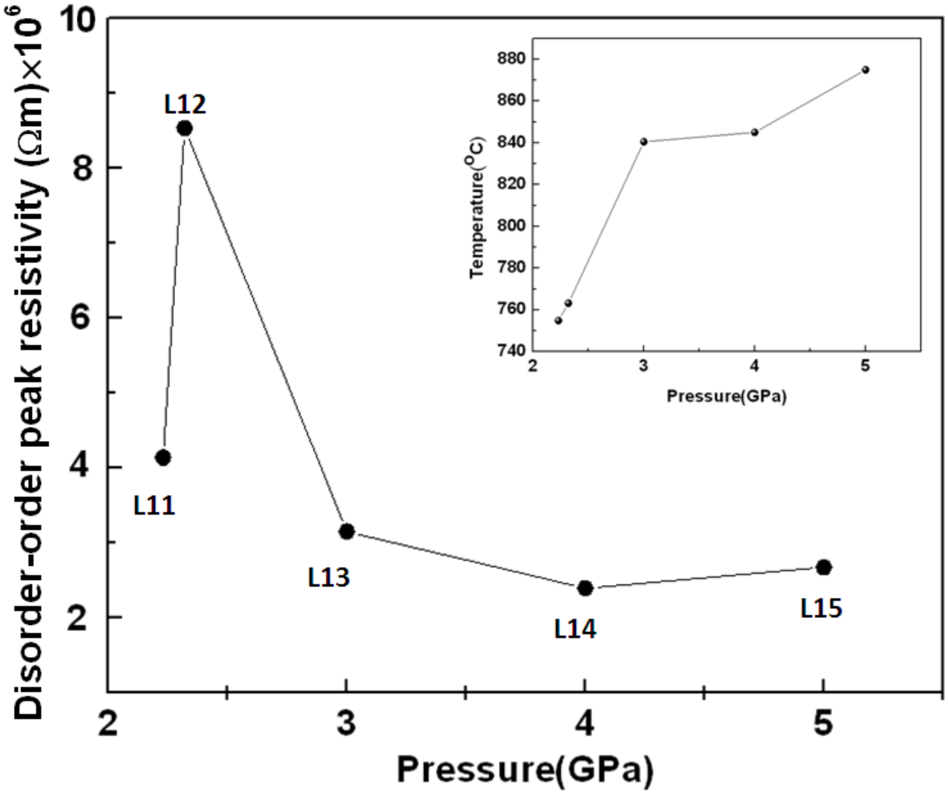

Figure 6.41 Pressure dependence of disorder-order peak resistivity values for L1n series. The insert illustrates the pressure dependence of the disorder-order temperature. Resistivity scale indicates that all plotted values have already been multiplied by 10^6.

No data are available in the literature on the effect of these plausible successive phase transitions on the electrical resistivity behavior. However, Baum et al. (1967) reported a similar anomaly in their study without discussing the source of the peak anomaly. Glaser and Ivanick (1956) have studied temperature dependence of $\rho(T)$ for Fe15Si and Fe16.9Si alloys at room pressure with an expectation to see an electrical resistivity peak at suggested order-disorder phase transition at 1120 ^{o}C , above the magnetic transition. However, they suggested that the closeness of transition temperature to the melting temperature of the alloys hindered observation of an anomaly specific to an order-disorder transition. Ruiz et al. (2005) also reported high electrical resistivity anomalies around 900 ^{o}C for Fe-Si alloys over 5.6wt%Si due to order-disorder transition. Taking guide from the above-mentioned studies and considering the possible effects of pressure on the phase diagram of Fe17Si alloy, the systematic electrical resistivity variation following the magnetic transition for L1n series is suggested to be the manifestation of structural phase change for Fe17Si alloy toward a disordered structure. As no in situ structural probing was employed, no conclusive comment can be made regarding the exact nature of this specific anomaly. The negative TCR values following the anomaly can be explained if Fe17Si enters an ordered phase which persists up to the melting. Baum et al. (1967) linked the negative TCR before melting to the covalent bond between Fe and Si in the solid which is broken at high temperatures and decreases the resistivity. On the other hand, the TCR sign change at the disorder-order like peak can be linked to the Mooij (1973) theory. If that is the case, then another interesting feature with a pressure-saturation origin is recognized. However, if saturation applies here, then the universality of the saturation is challenged according to the present data which is in agreement with Varga et al. (2002).

6.6.6 Melting transition

The melting temperature of L1n series is compared with Yang and Secco (1999) in Figure 6.42.

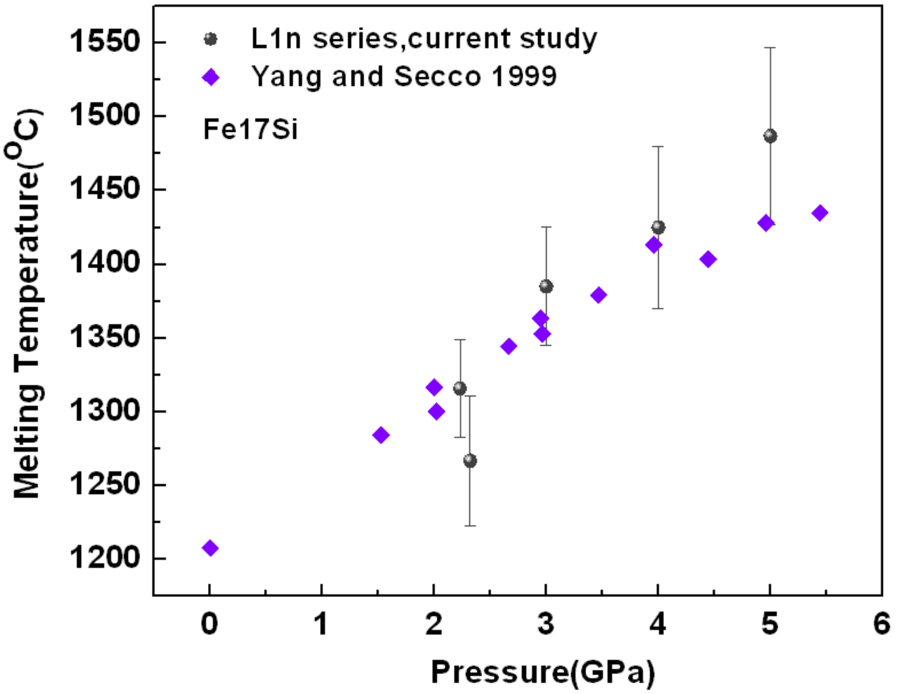

Figure 6.42 Comparison between melting temperature of L1n series and Yang and Secco (1999).

Within the error bars of the current study, the melting boundary data are in agreement with Yang and Secco (1999). As the most important part of the current research, the melting transition signals for L1n experiments are presented in the following. Looking at the expected melting transition regions of the resistivity plots, their characteristics are substantially different from melting signals in the previous P2n, P1n and S1n experiments, and also from those reported by Yang and Secco (1999). Resistivity values exhibit an obvious drop at the melting point as shown in Figure 6.43. Table 6.4 shows a summary of the characteristics of L1n series and compares $d\rho_{solid}/d\rho_{liquid}$ values. It is interesting that even L11 which was the most contaminated run, shows pronounced drop in resistivity at the melting. However, as it is not clear at what exact temperature the contamination has started, no comment can be made on that.

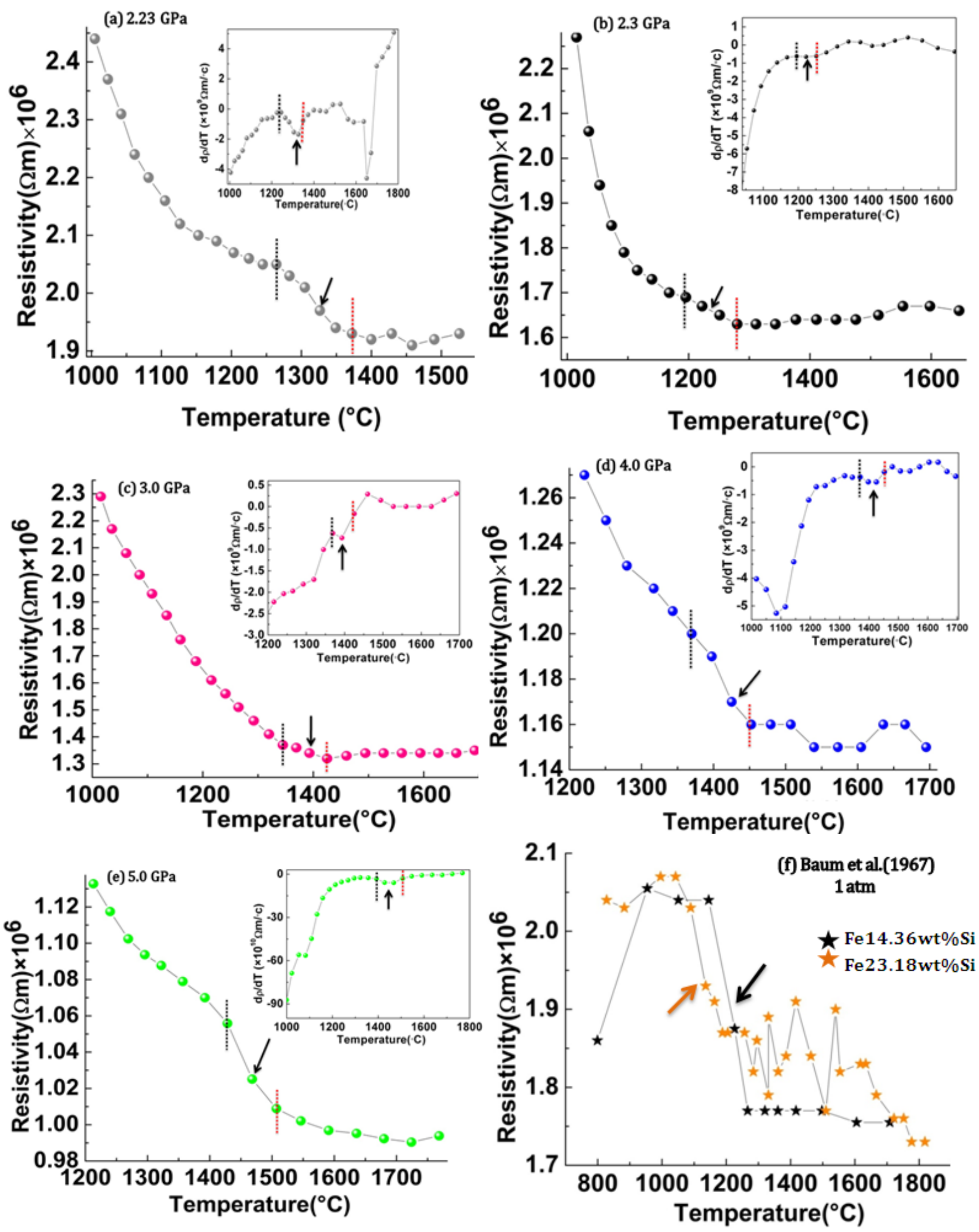

Figure 6.43 (a) to (e) Melting transition for L1n experiments shown in electrical resistivity versus temperature for Fe17Si; (f) resistivity values at 1 atm from Baum et al. (1967). Resistivity scale indicates that all plotted values have already been multiplied by 106. The inserts are first derivatives of resistivity with respect to temperature (already

multiplied by 109) versus temperature which clearly shows the melting signal as a local minimum.

Table 6.4 Main characteristics of L1n experiments at melting. Values in parentheses are Yang's (1999) corresponding melting temperatures.

Exp.	Pressure (GPa)	ρ at melting ($10^{-6}\ \Omega$m)	$\rho_{solid}/\rho_{liquid}$	Melting temperature (^{o}C)
L11	2.23	1.73	1.05	1316±33 *(2 GPa:1312)*
L12	2.32	1.67	1.04	1267±44
L13	3	1.37	1.03	1397±30 *(1366)*
L14	4	1.2	1.04	1425±55 *(4.5 GPa:1385)*
L15	5	1.06	1.05	1487±60 *(1423)*

The phenomenon of resistivity drop on melting was reported by Baum et al. (1967) for room pressure experiments on Fe-Si alloys as shown in Figure 6.44. Baum and his colleagues reported electrical resistivity values for Fe-Si alloys between 800^{o}C to 1700^{o}C at different compositions including 14.36 and 28 wt%Si which are the two closest compositions to the 17wt%Si composition under investigation here.

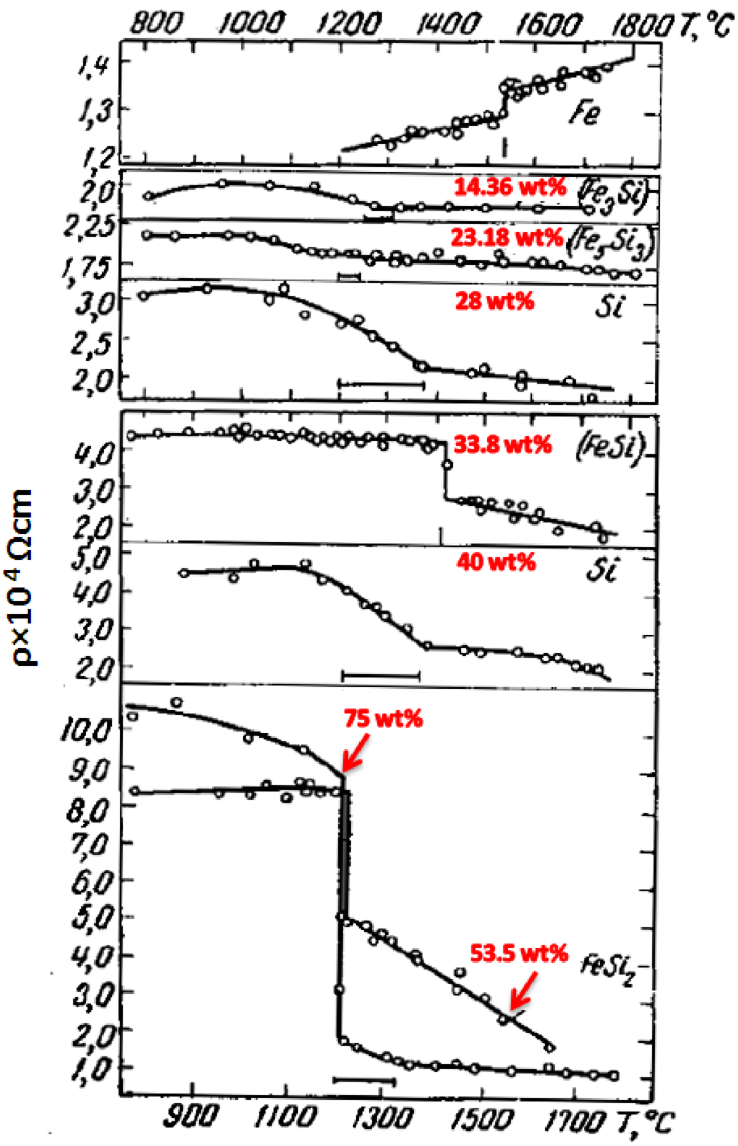

Figure 6.44 Effect of temperature on the resistivity of Fe silicon alloys at 1 atm (after Baum et al., 1967). The numbers in red are Si content in wt%.

TCR values were all negative close to melting for all of the reported composition values including 14.36 and 28wt%Si. Also, except for Fe14.36Si which did not undergo any discontinuous change in resistivity during the process of melting, for the rest of compositions, electrical resistivity falls and this decrease is systematically greater as the composition increases. Within the melt, the slope of (dρ/dT) was zero for 14.36 wt%Si and slightly negative for 28wt%Si. Although the short range structure of liquid Fe-Si is still under debate (Spektor et al. 1974; Sanloup et al. 2004; Gu et al. 2004), but studies suggest that the covalent bond between Fe and Si in the solid is broken at high temperatures (Baum et al., 1967) and that will release Fe bound electrons which consequently decreases the resistivity. Figure 6.45, illustrates the high temperature electrical resistivity behavior of L1n series compared to Baum et al. (1967) data for room pressure Fe14.38Si and Fe23.18Si alloys. Except for L11 high temperature values, the rest of L1n series plots are located lower than Baum et al. (1967) which accords with the expectation of high pressure resistivity values to be lower than room pressure results. It should be noted that, most of the studies on liquid structure of Fe-Si are carried out at room pressure and there is a need for structural investigations at Fe-Si liquid state under high pressures. One of the tools to study the behavior of liquid Fe17Si as a function of temperature and pressure is by the TCR and PCR values which are discussed in the following. These coefficients may offer further insight about molten Fe17Si alloy but also from the geophysical point of view, will have an importance in relates to the Earth's core heat budget discussion.

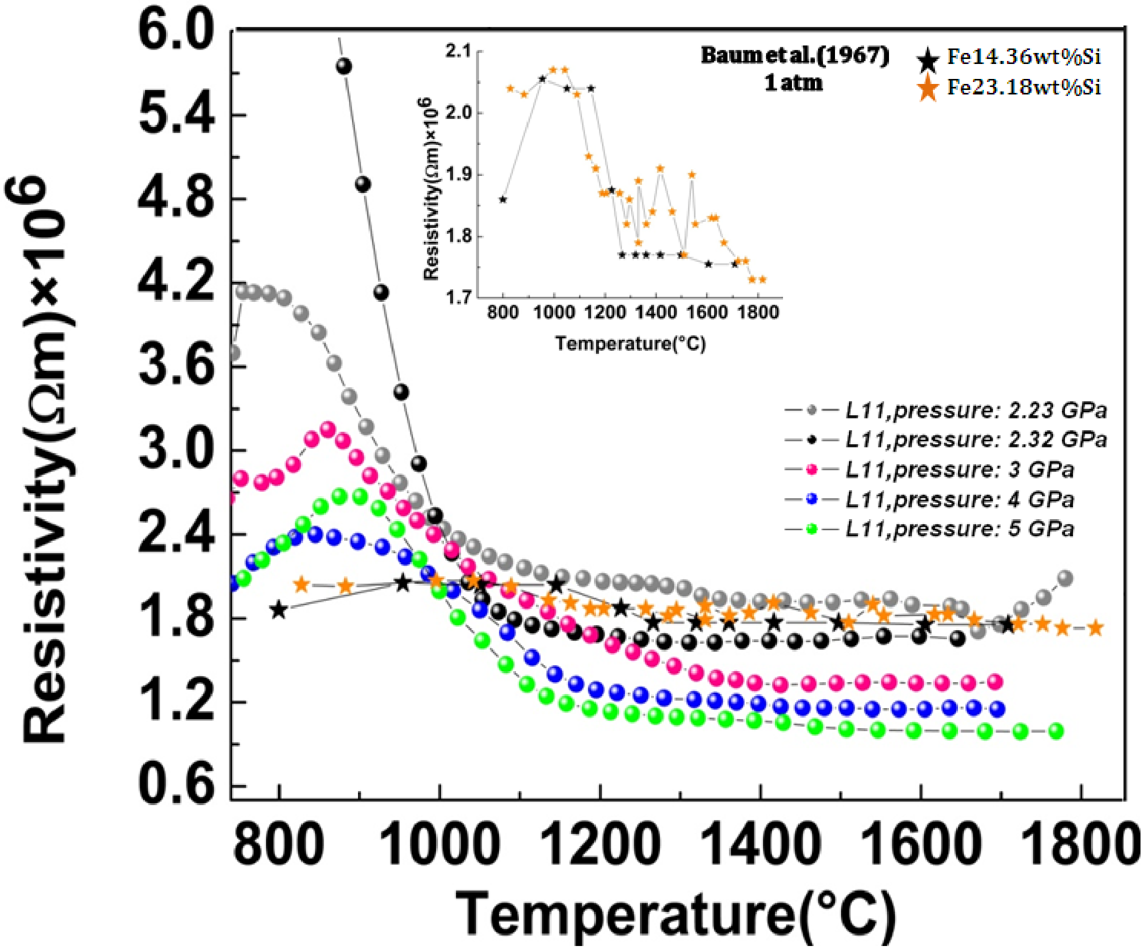

Figure 6.45 High temperature electrical resistivity values for L1n series compared to Fe23.28wt%Si values from Baum et al. (1967). The insert is the magnified plot of Baum's data. Resistivity scale indicates that all plotted values have already been multiplied by 10^6.

6.6.7 TCR values of Fe17Si in the liquid state

L1n experiments revealed that the TCR values are negative at the melting boundary as shown in Figure 6.46. For most of the L1n experiments though a slight increase occurs beyond the melting transition within the liquid. It should be noted that, even after melting occurs, experiments at higher pressure have a greater range of temperature with negative TCR values. Two groups of TCRs can be calculated:

- Group 1: For points during the melting process
- Group2: For liquid points after completion of melting

This has implications when it comes to extrapolating the resistivity values to higher pressure and temperatures which will be discussed in the following sections.

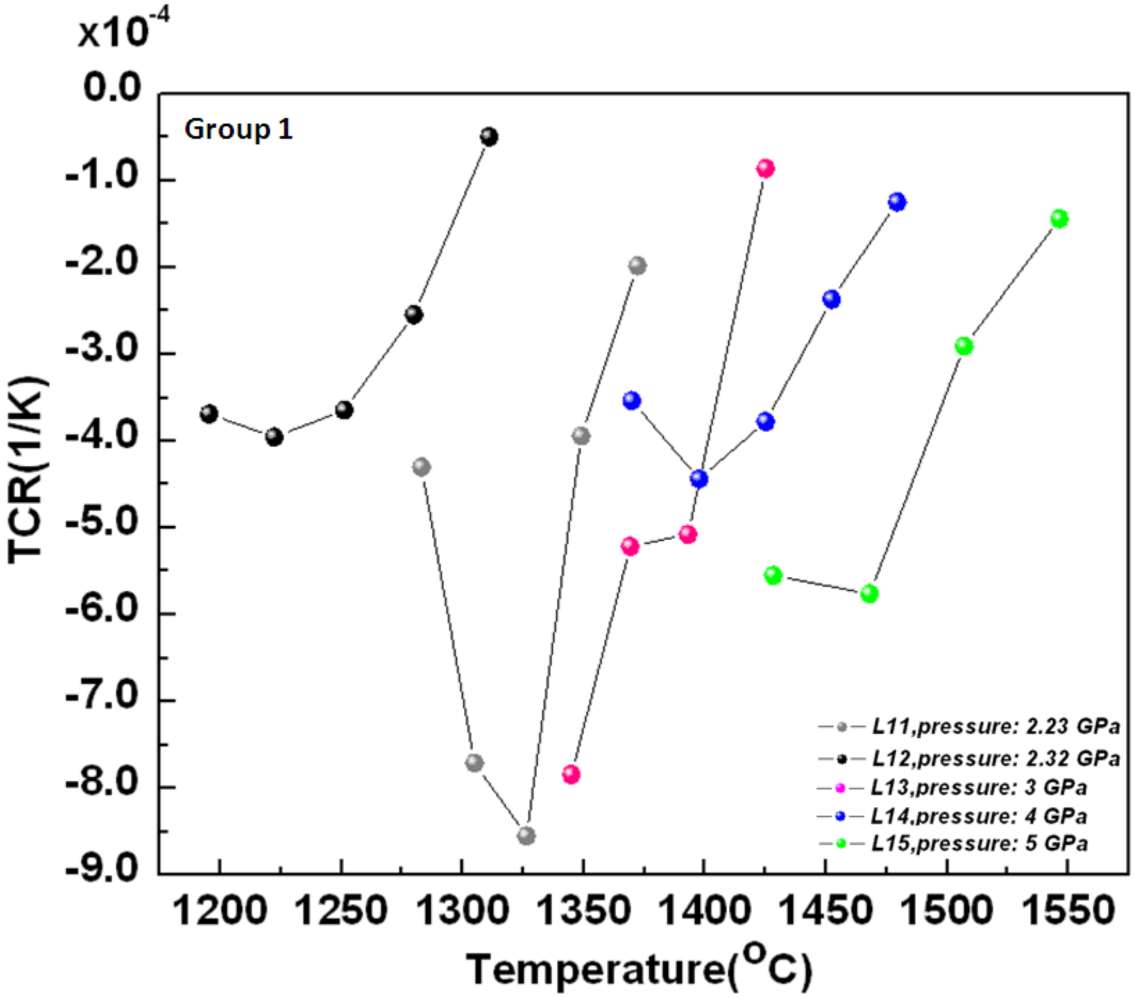

Figure 6.46 Temperature dependence of TCR values for L1n series during the melting process (Group1).

Contrary to Yang (1999) TCR values of 3.4×10^{-3} K^{-1}, the resultant Group 1 TCR values for L1n series exhibit variation with pressure with an average of $-4\times10^{-4} \pm 1.6\times10^{-4}$ K^{-1} as shown in Figure 6.46.

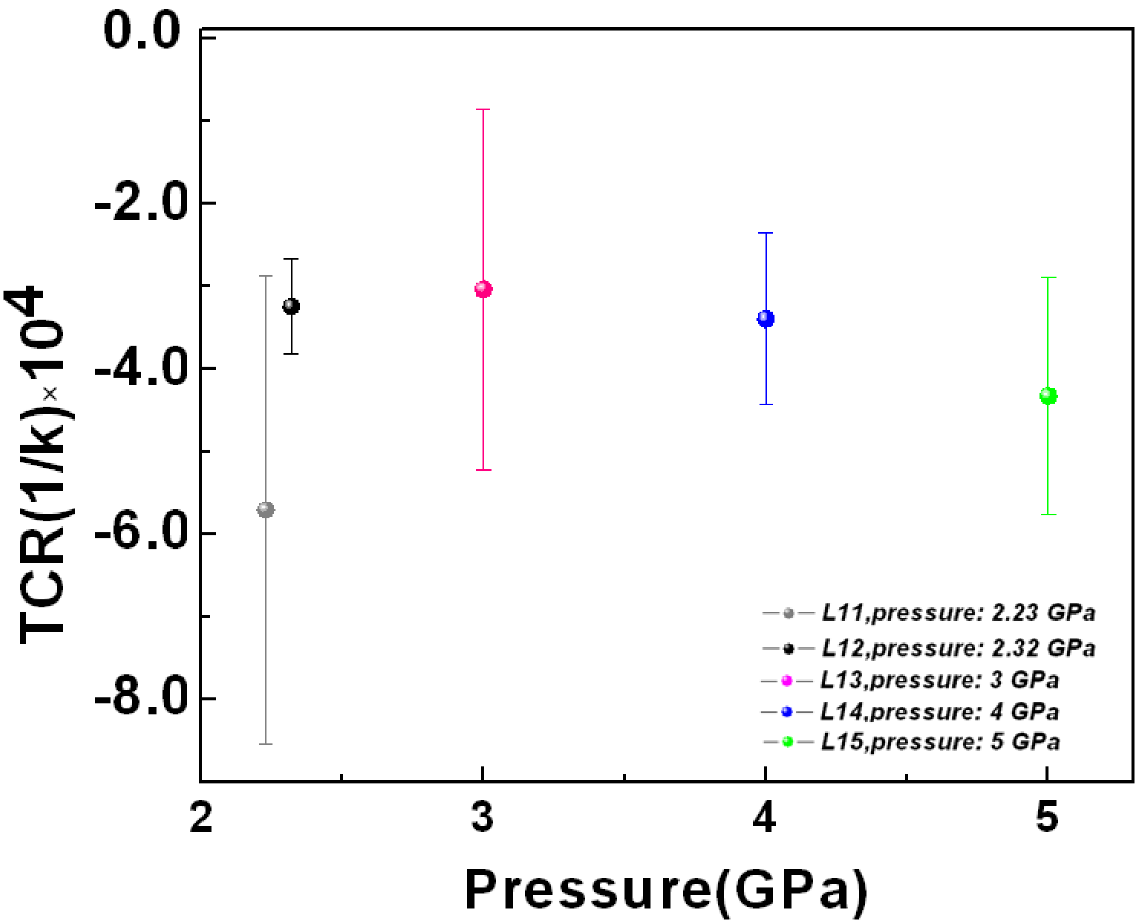

Figure 6.47 Pressure dependence of TCR values at the melting boundary.

No strong pressure dependence for TCR is recognizable for Group1. However, it is clear that Yang (1999) TCR values are all positive while TCR values of Group1 of the present study are all negative which is in complete agreement with Baum et al. (1967). Figure 6.47 illustrates the temperature dependence of TCR values for Group 2 data set in which L11 is excluded because of the higher contamination compared to the rest of L1n experiments. The values show more correlation with pressure and there is a transition from positive TCR to negative TCR values at 3 GPa. Figure 6.48 illustrates the pressure dependence of TCR values for Group2.

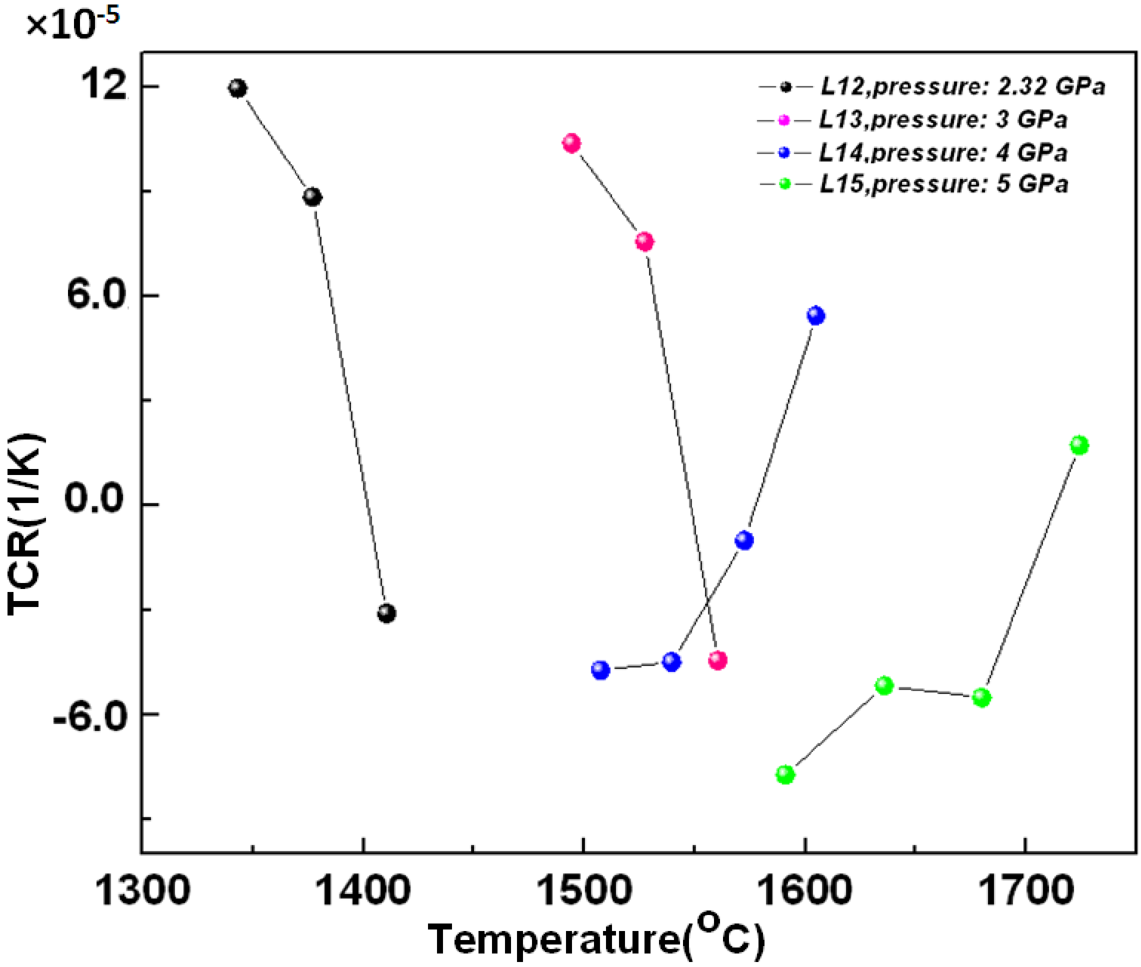

Figure 6.48 Temperature dependence of TCR values for Group2 liquid points.

Contrary to Group1, TCR values from Group2, exhibit a strong negative pressure dependence up to 5 GPa. The TCR sign changes from positive to negative at 3 GPa may have an important implication for short range structural change of Fe17Si within the liquid state which remains to be tested with further studies.

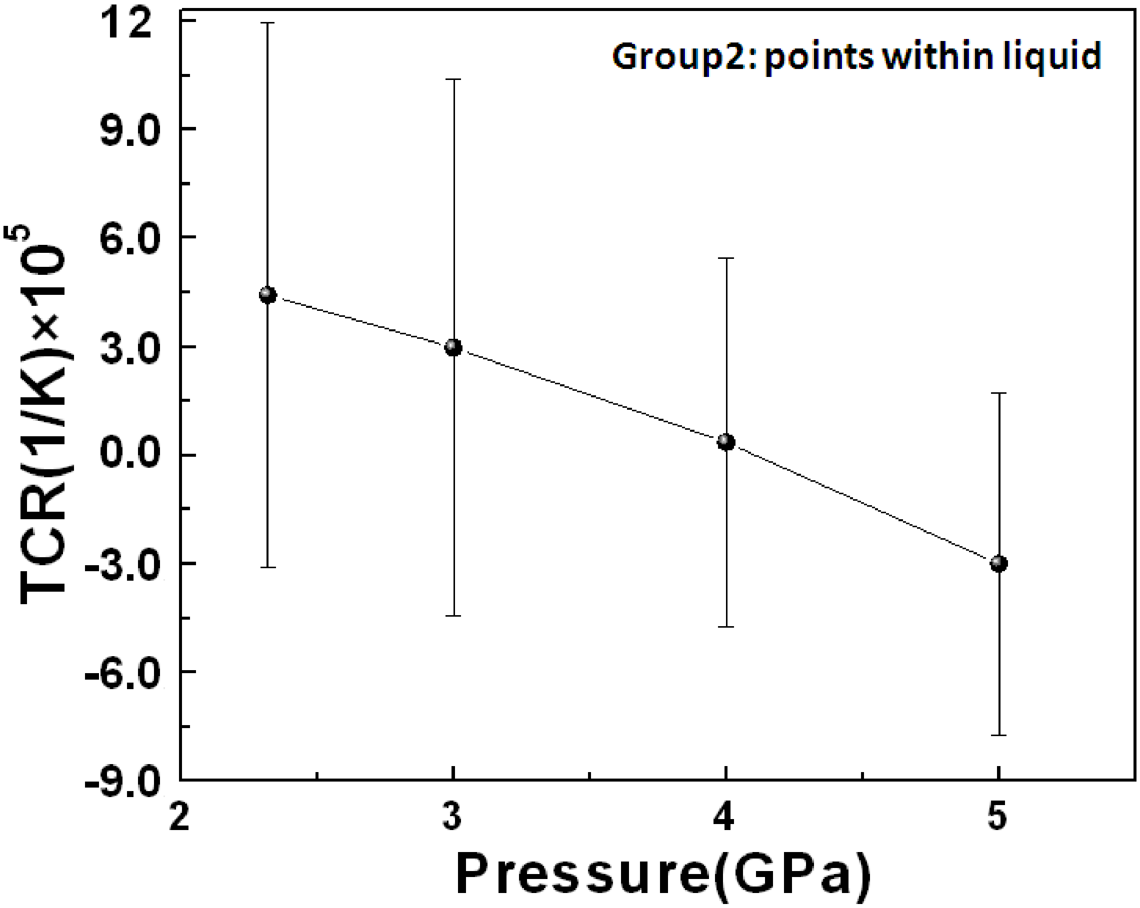

Figure 6.49 Pressure dependence of TCR values for Group2. TCR scale indicates that all plotted values have already been multiplied by 10^5.

6.6.7.1 PCR values at room temperature and within the liquid state

The ρ(P) values at the melting boundary are plotted in Figure 6.50 with a comparison with liquid resistivities for Fe17Si and pure Fe from Yang (1999). From Figure 6.50 it is clear that the melting boundary resistivities decrease by increasing pressure. L11 is excluded because of the higher level of contamination. Two different fitting approaches were considered to obtain PCR values: a linear fitting which yields a PCR value of -0.18 GPa^{-1} which is higher than Yang's value by a factor of 2.1. However, it should be noted that Yang's melting point PCR value presented in Figure 6.50 was calculated within a limited pressure range (1.4-2.6 GPa) as compared to the present study (2.23-5 GPa) which makes the comparison limited. On the other hand, it seems that ln(ρ) values follow a decaying trend as a function of pressure rather than a linear trend so that the initial strong dependence of ln(ρ) values on pressure appears to be mitigated at higher pressures. The implications of fitting functions on the geophysical interpretations are discussed later. The negative PCR value for Fe17Si suggests metallic behavior but there is no similarity in magnitude of PCR with that of pure Fe within the 2-5 GPa pressure range which has a value of -3.17×10^{-4} GPa^{-1} as reported by Secco and Schloessin (1989).

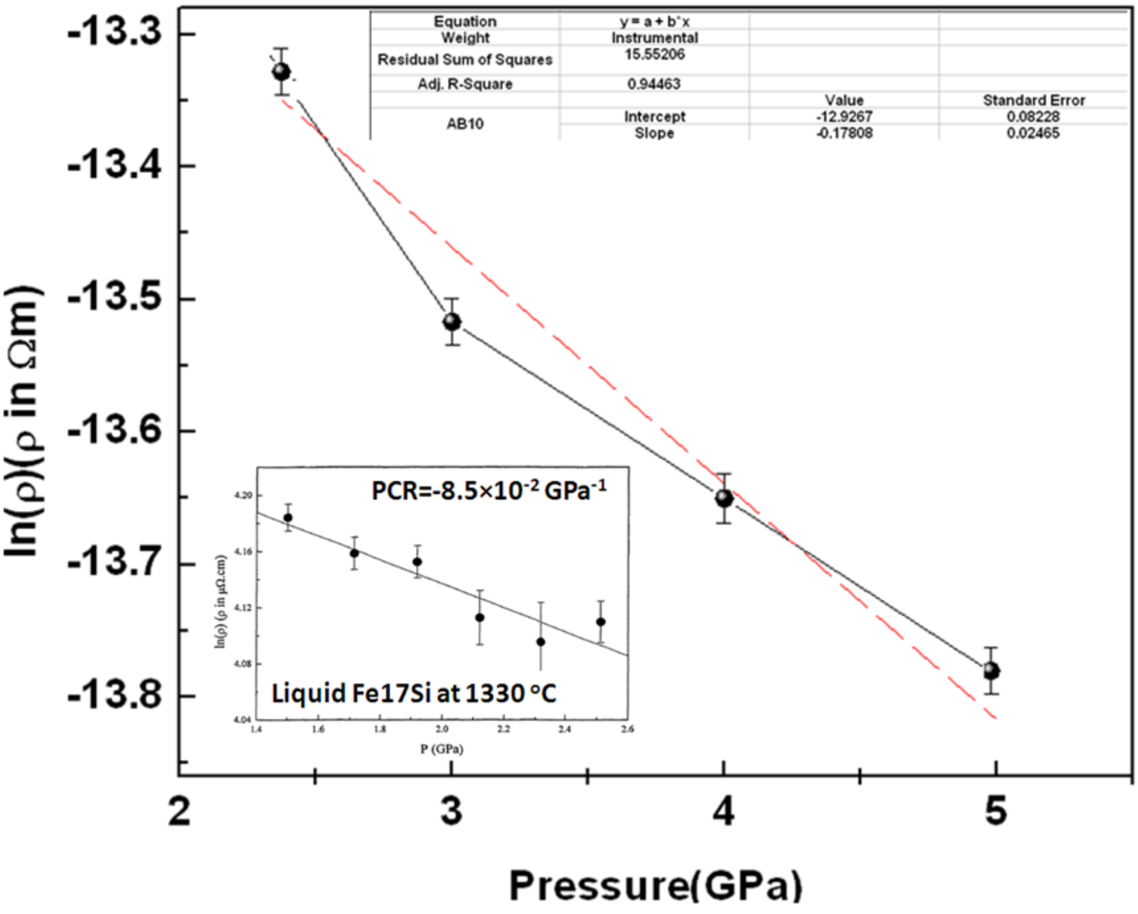

Equation	y = a + b*x		
Weight	Instrumental		
Residual Sum of Squares	15.55206		
Adj. R-Square	0.94463		
		Value	Standard Error
AB10	Intercept	-12.9267	0.08228
	Slope	-0.17808	0.02465

PCR=-8.5×10^{-2} GPa^{-1}

Liquid Fe17Si at 1330 °C

Figure 6.50 Pressure dependence of electrical resistivity of L1n series at the melting boundary. The insert shows the PCR values from Yang and Secco (1999).

Therefore, it suggests that liquids in pure Fe and Fe17Si system do not respond to compression in a same way within the pressure range of 2-5 GPa. It should be noted that from a close inspection of the experimental procedure employed by Yang (1999), and also from repeating some of his designs within the current research, it is believed that the major source of discrepancy stems from the G-factor effect. Specially, Yang (1999) data likely had a very high electrode material contribution to the measured electrical resistivities. These could have not only masked the decrease in resistivity at the melting point but also may have affected the magnitude of electrical resistivity values to be as high as 10^{-4} Ωm.

6.6.7.2 Electrical resistivity of Fe17Si and pure Fe liquid

A comparison of resistivity values for liquid Fe17Si and liquid Fe from this study and those for liquid Fe from Secco and Schloessin (1989) is shown in Figure 6.51. As indicated in this figure, at almost the same pressure of 2 GPa, the effect of adding 17wt% Si changes pure Fe resistivity by a factor of 1.4. However, as the pressure increases, this difference gets smaller and surprisingly, the resistivity values for Fe from Secco and Schloessin (1989) at 5.26 GPa approximately coincides with the resistivity values for Fe17Si at 5 GPa. Therefore, it seems at higher pressure, the electrical resistivity of Fe17Si approaches that of pure Fe. However, there is a need for higher pressure experiments to assess what happens at higher pressures.

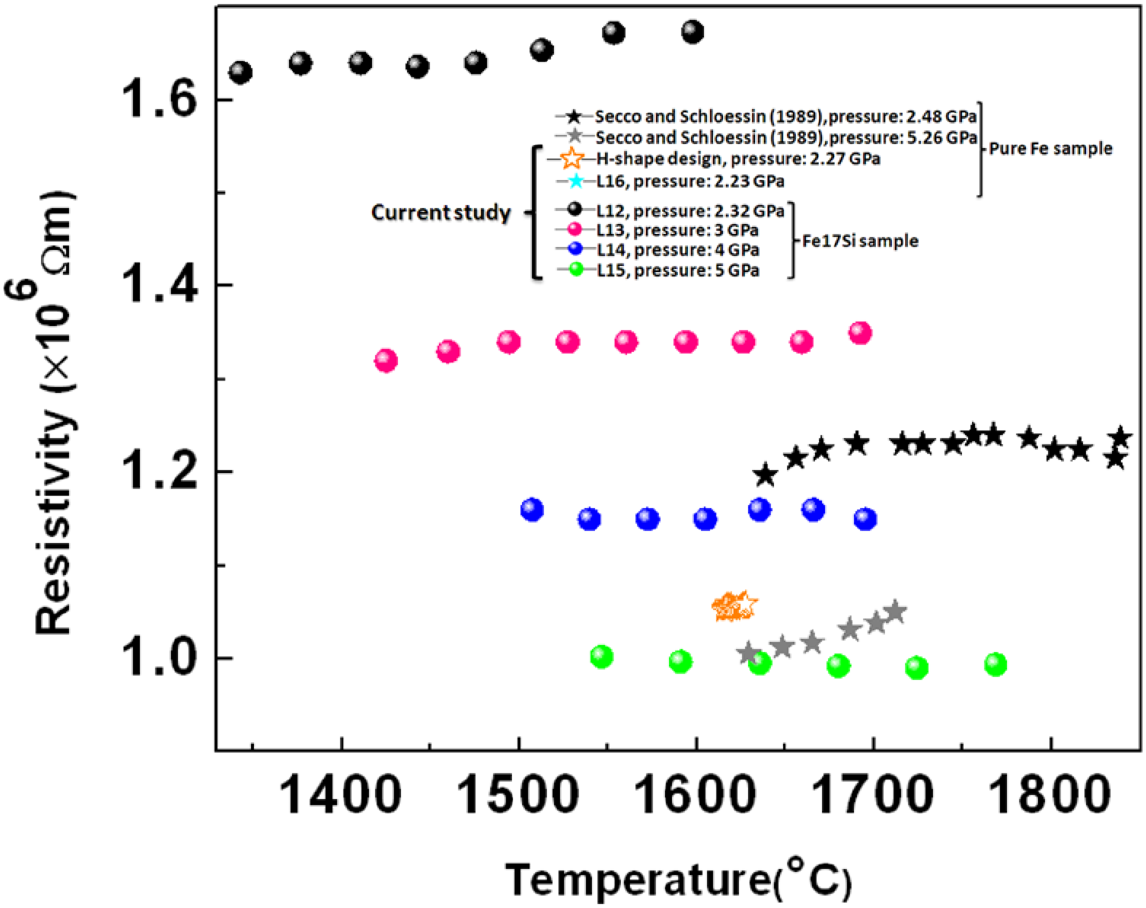

Figure 6.51 Comparison of T-dependence of resistivity of liquid Fe17Si and pure Fe of the present study and pure Fe from Secco and Schloessin (1989) at 2.48 and 5.26 GPa. Resistivity scale indicates that all plotted values have already been multiplied by 10^6.

6.7 Geophysical implications

Electrical resistivity of Fe-Si alloys may provide an independent way of assessing the validity of Si as a light element alloying in the Earth's core. Since the first estimation of the electrical resistivity of the Earth's core of 1.0×10^{-6} Ωm (Elsasser, 1946), theoretical as well as experimental studies have been done on electrical resistivity of pure Fe or its alloys with Si. The lack of understanding of interactions between the effects of temperature, pressure and impurities puts the extrapolations on uncertain ground.

Although, any suggested value for the electrical resistivity of Fe alloy and its inverse, electrical conductivity should meet the constraints that are imposed by dynamo sustainability and also the thermal budget of the Earth's core. The latter is much more sensitive to electrical resistivity than the former. That is, the dynamo could withstand a factor of two variation in the electrical resistivity of the core, but the associated thermal conductivity would have large consequences for the core heat flow. There is no common agreement on resistivity values under core conditions. However, two groups can be distinguished based on high or low resistivity values suggested for the Earth's core as summarized in Tables 6.5 and 6.6.

Table 6.5 Electrical resistivity values in the high resistivity group

Reference	**Pressure (GPa)**	**Resistivity (Ωm)**	**Sample**	**Method**
Secco and Schloessin (1989)	136	1.50×10^{-6}	Pure Fe	Electrical resistivity measurement up to 7 GPa
Bi et al. (2002)	208	1.31×10^{-6}	Pure Fe	Shock wave
Stacey and Loper (2007)	136	4.65×10^{-6}	Fe-10.7wt%Ni-14.35wt%Si	Extrapolation from Mattasov (1977) data
Stacey and Loper (2007)	330	3.62×10^{-6}	Fe-10.7wt%Ni-14.35wt%Si	Extrapolation from Mattasov (1977) data

Table 6.6 Electrical resistivity values in the low resistivity group.

Reference	**Pressure (GPa)**	**Resistivity (Ωm)**	**Sample**	**Method**
Keeler and Mitchell (1969)	140	1.00×10^{-6}	Pure Fe	Shock wave
Keeler and Royce (1971)	140	6.80×10^{-7}	Pure Fe	Shock wave
Mattasov (1977)	140	8.51×10^{-7}	Fe- 4wt%Si	Shock wave
Mattasov (1977)	140	1.15×10^{-6}	Fe- 14wt%Si	Shock wave
Mattasov (1977)	140	1.50×10^{-6}	Fe- 20wt%Si	Shock wave
Gomi et al. (2013)	140	2.90×10^{-7}	Fe-2wt%Si	DAC*+ extrapolation
Gomi et al. (2013)	140	1.00×10^{-6}	Fe-12wt%Si	DAC+ extrapolation
Pozzo et al. (2012)	330	6.25×10^{-7}	Pure Fe	First principle calculation
Pozzo et al. (2012)	136	7.14×10^{-7}	Pure Fe	First principle calculation
Pozzo et al. (2013)	136	7.70×10^{-7}	Fe-8wt%O-10wt%Si	First principle calculation
Pozzo et al. (2013)	330	9.09×10^{-7}	Fe-8wt%O-10wt%Si	First principle calculation

*DAC-Diamond anvil cell

The important fact that should be considered is the consistency and convergence of the results of low electrical resistivity value group despite the different and independent approaches that have been employed as first principle studies: (Gomi et al., 2013; de Koker et al., 2012; Pozzo et al, 2012; Pozzo et al., 2013) and shock wave experiments: (Keeler and Mitchell, 1969; Keeler and Royce, 1971; Mattasov, 1977). The key point that connects these works to each other is the concept of electrical resistivity saturation phenomena that was not considered in previous studies. This has profound implications for electrical and thermal conductivity characteristics of the Earth's core (Hirose et al., 2013). The saturation of resistivity by application of temperature makes resistivity values at high T to depart from the regular linear possible dependence of resistivity with temperature as was considered before (Stacey and Anderson, 2001). The effect of pressure is also proven to cause the resistivity to vary as a saturated system close to CMB and ICB pressure values (Gomi et al., 2013). Shock wave electrical resistivity results of Mattasov (1977) also had exhibited a saturation behavior as all different Fe-Si samples with different Si composition, were inclined to converge at pressures comparable to the Earth's core. A compilation of data from available literature values for Fe-Si electrical resistivity shown in Figure 6.52 provides a current picture of the suggested electrical resistivity values for the core just below CMB. Introducing the results of the current study into the picture, melting boundary electrical resistivity values are plotted. In order to make any speculation about the probable behavior of Fe17Si electrical resistivity from low pressure (current study) to higher pressure (CMB), two important factors are: the phase diagram of Fe17Si and the effect of saturation of resistivity at high P and T. Taking guidance from the very recently reported phase diagram of Fe16Si (Fischer et al., 2012) as shown in Figure 5.2 and as in an insert in Figure 6.52, it suggests an order-disorder transition ($D0_3$-B2) starting around 50 GPa on the melting boundary. If one considers the affinity of short range liquid structure to the solid parent structure (Secco and Schloessin, 1989; Sanloup et al., 2000; Sanloup et al., 2011; Mirzoev and Sobolev, 2011), the order-disorder transition should be reflected on the melting boundary electrical resistivity values. As discussed before, order-disorder transitions tend to increase the electrical resistivity.

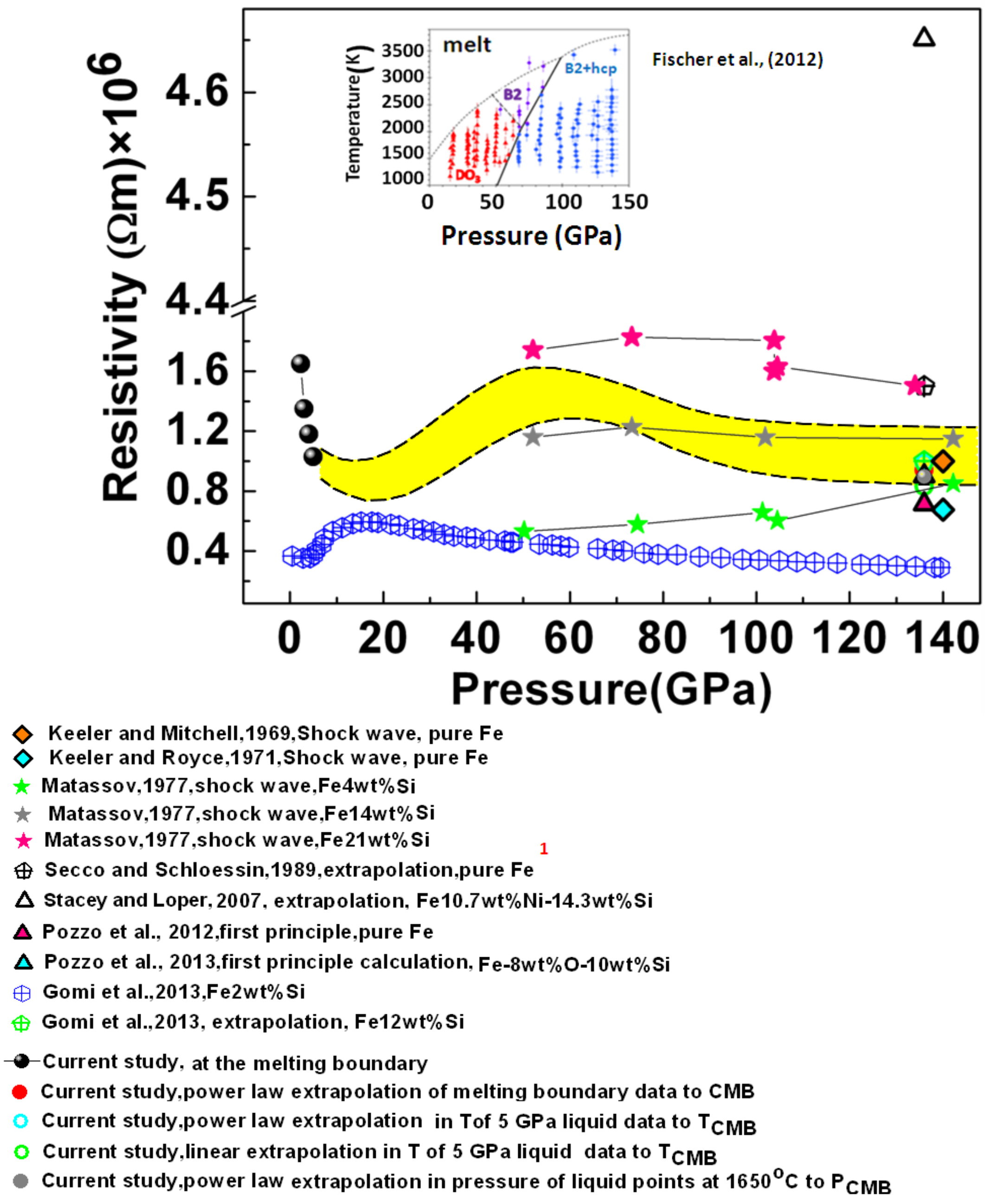

[1] They gave physical argument to support a CMB value. This is why it is not a true extrapolation.

Figure 6.52 Comparisons of electrical resistivity values up to core pressure. The arrows point to possible phase transitions at 50 and 100 GPa for Fe17Si alloy. The yellow band is explained in the text. Resistivity scale indicates that all plotted values have already been multiplied by 10^6.

Therefore, one may expect similar electrical resistivity anomaly beginning around the order-disorder transition for Fe17Si alloy along its melting boundary. On the other hand, pressure-induced resistivity saturation is expected to play a leading role in the resistivity trend after the completion of the order-disorder transition, while, temperature-induced electrical resistivity saturation should affect the resistivity trend along the melting boundary. At this point, two guides have been considered for assessing the electrical resistivities of Fe17Si at CMB conditions. First, if one considers the Mattasov (1977) resistivity values at the CMB as reference data, values for Fe17Si resistivities should lie somewhere between the 14 and 20 wt%Si data sets. Also values for Fe17Si should be located above Gomi et al. (2013) electrical resistivity values for Fe2Si. The second guide stems from the PCR and TCR behavior of L1n series as was discussed before. These characteristics suggest not only a negative TCR value at the melting boundary for all pressure ranges within the current study, but turning to negative TCR values within the liquid state as the pressure increases above 3 GPa. With L15 experiment having the minimum TCR value within the liquid among all experimental data, the melting boundary results at all pressure ranges between 2.3 to 5 GPa and liquid data of all pressure ranges at the fixed temperature of 1650 ^{o}C, five different methods were considered in order to estimate the resistivity values at the CMB as follows:

1. Linear fitting to melting boundary resistivity values
2. Power law (exponential decaying function: $(A\exp(-x/t)+y_0)$) fitting to the melting boundary resistivity values
3. Power law extrapolation in pressure of liquid points at constant temperature of 1650 ^{o}C
4. Linear extrapolation in temperature of 5 GPa liquid data to T_{CMB}

5. Power law extrapolation in temperature of 5 GPa liquid data to T_{CMB}

Figure 6.53 illustrates the comparison between power law extrapolation and linear extrapolation of melting boundary results. As it is shown in the figure, power law fitting provides significantly a better fit than linear method. Therefore, power law fitting was considered for extrapolating melting boundary results to the core. For the same reason, power law fitting was considered to extrapolate in pressure for liquid points at the fix temperature of 1650 ^{o}C. Linear temperature extrapolation of L15 at 5 GPa to the CMB temperature yields a very low negative slope, -6.3×10^{-11} Ωm/^{o}C which suggests that electrical resistivity diminish gradually within the saturation model. Extrapolated values from all methods are listed in Table 6.7. It is interesting to note that different extrapolation methods give reasonably similar core resistivity values. The extrapolated values lie within the recently suggested low electrical resistivity estimates at CMB as shown in Figure 6.52.

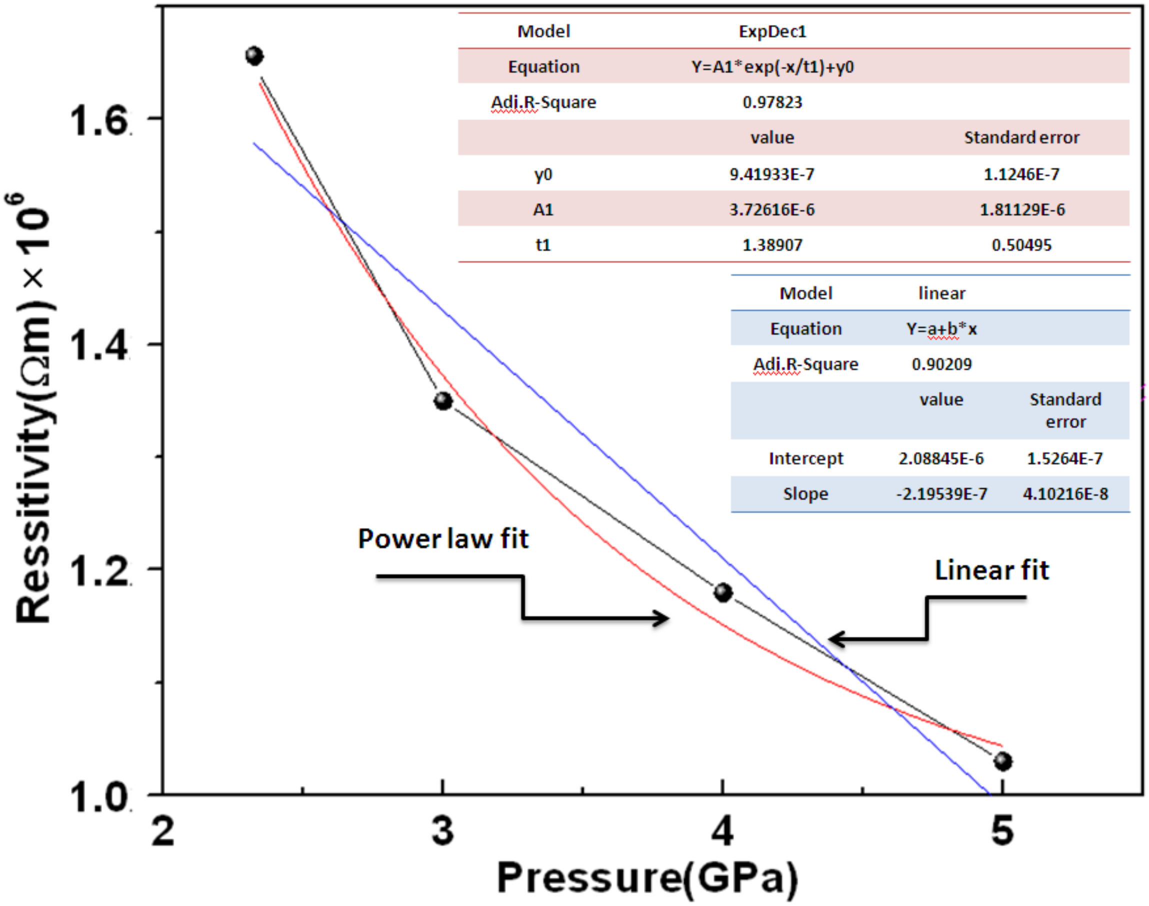

Model	ExpDec1	
Equation	Y=A1*exp(-x/t1)+y0	
Adj.R-Square	0.97823	
	value	Standard error
y0	9.41933E-7	1.1246E-7
A1	3.72616E-6	1.81129E-6
t1	1.38907	0.50495

Model	linear	
Equation	Y=a+b*x	
Adj.R-Square	0.90209	
	value	Standard error
Intercept	2.08845E-6	1.5264E-7
Slope	-2.19539E-7	4.10216E-8

Figure 6.53 Power law fitting and linear fitting to resistivity data at the melting boundary for L1n series. Resistivity scale indicates that all plotted values have already been multiplied by 10^6.

Table 6.7 Electrical resistivity extrapolation results to the Earth's core from the present study.

Method	**Estimated ρ (10^{-7} Ωm)**	**Extrapolation in**
2	9.4	Pressure and temperature
3	9	Pressure
4	8.3	Temperature
5	9.9	Temperature

Combining the probable effects of an order-disorder transition on the melting boundary, as well as saturation effects, a band for the electrical resistivity of Fe17Si to CMB conditions is drawn in Figure 6.52. The chosen width of the band is guided by the dependence on T and composition from the Mattasov (1977) data, and the resistivity dependence on P by the Mattasov (1977) and Gomi et al. (2013) data. There are still several uncertainties about the Fe17Si electrical resistivity at high pressure and temperature behavior. First, no comment can be made about the B2 to B2+hcp phase transition effects on electrical resistivity of Fe17Si as there is no study available in this. Also, it is not clear that how exactly pressure and temperature- induced saturation interact in the case of liquid Fe17Si alloy.

6.8 Thermal conductivity calculations and implications for the thermal evolution of the Earth’s core

The geodynamo power is controlled by the heat flux across the CMB (Lay et al., 2008). Estimates of CMB heat flux depend on highly debated parameters of the outer core such as electrical conductivity and thermal conductivity (Labrosse et al., 1997; Buffett et al., 2000; Gubbins et al., 2004). For a metal, these are connected through the Wiedemann-Franz law as follows:

$$k = 1/\rho \times L \times T \tag{6.1}$$

where k is the electronic thermal conductivity, ρ is the electrical resistivity, L is the Lorentz number (L = 2.44×10^{-8} WΩ/K^{2}), and T is the absolute temperature. Considering the extrapolated electrical resistivity results of the liquid data of the present results it yields a range of value for k from 103 Wm^{-1}K^{-1} to 109 Wm^{-1}K^{-1} at CMB. Employing 5 GPa liquid data from the present research, a range of values for k is obtained from 172 to

189 $Wm^{-1}K^{-1}$ at the ICB corresponding to the temperature range of 5200 K $< T_{ICB} <$ 5700 K and 112 to 124 $Wm^{-1}K^{-1}$ at the CMB corresponding to the temperature range of 3800 K $< T_{CMB} <$ 4200 K. Stacey and Anderson (2001) calculated the electronic thermal conductivity to be 43 $Wm^{-1}K^{-1}$ at the CMB and 60 $Wm^{-1}K^{-1}$ at the ICB. They proposed the total thermal conductivity at the CMB to be 46 $Wm^{-1}K^{-1}$ and 63 $Wm^{-1}K^{-1}$ at ICB. However, in 2007, on the basis of extra electrical conductivity reduction of pure Fe due to the suggested behavior of s electrons under high pressure, Stacey and Loper revised the previously reported thermal conductivity values to 28 $Wm^{-1}K^{-1}$ and 29 $Wm^{-1}K^{-1}$ at the CMB and the ICB respectively. Ab initio calculations on the electrical resistivity of Fe-Si alloys by Gomi et al. (2013) yielded different values of Earth's core thermal conductivity as 85–140 $Wm^{-1}K^{-1}$ at the CMB and 138–221 $Wm^{-1}K^{-1}$ at the ICB. Extrapolations obtained from recent diamond-anvil-cell experiments of Hirose et al. (2011) also reported a value in the range 90-130 $Wm^{-1}K^{-1}$ at the top of the outer core. These recent results are also in broad agreement with the recently reported density functional theory (DFT) calculations of the thermal conductivities for Fe, Fe-Si (8.15wt% and 14.35wt% Si), and Fe-O (8.15wt% and 14.35wt% O) liquid alloys by de Koker et al. (2012) which ranges from 100 to 230 $Wm^{-1}K^{-1}$ at the CMB. Surprisingly, Pozzo et al. (2013) also calculated high thermal conductivity values of k = 100 W $m^{-1}K^{-1}$ at the CMB and, 160 $Wm^{-1}K^{-1}$ at the ICB using ab initio calculations on two liquid iron-silicon-oxygen mixtures ($Fe_{0.82}Si_{0.10}O_{0.08}$ and $Fe_{0.79}Si_{0.08}O_{0.13}$). These recent thermal conductivity estimates are 2 to 3 times higher than those from Stacey and Anderson (2001) which have been used conventionally. The higher thermal conductivity implies high heat loss through conduction down the outer core adiabat that can substantially weaken thermal convection and reduce the power to drive a dynamo generating the magnetic field. Therefore, our

understanding of the Earth's core evolution and the geodynamo as well as the age of the Earth's inner core should be revised accordingly and demands a revision of the power requirements for the geodynamo. With respect to the problem posed for the dynamo power by the high heat flux across CMB, if a stratified layer on top of the core exists (Buffett et al., 2000), this could mitigate the high thermal conduction and reduce heat flow through the CMB. However, a paradox appears as the accumulation of the light elements within the stratified layer results from inner core crystallization and the associated chemical buoyancy. A large thermal conductivity on the other hand, imposes a high cooling rate for the core and consequently a much younger inner core (age ~ 1Gyr) (Pozzo et al, 2012) than postulated before by Labrosse et al. (2001). Therefore, it prohibits the possibility of a chemically stratified layer before the existence of the inner core (de Koker et al., 2012). On the other hand, the existence of a thermally stratified layer poses another difficulty. Pozzo et al. (2012) argue that high thermal conductivity and the associated high cooling rate, enforces a thermally stratified layer in the absence of compositional convection. This layer can become too thick and finally shuts off the dynamo action unless one introduces the possibility of another source of heat, such as, radiogenic heat, that in turns thins the thermally stratified layer. As one of the very robust consequences of high thermal conductivity, it weakens thermal convection compared to chemical convection. Therefore, in order to maintain the same dynamo power with less available thermal buoyancy, a faster core cooling rate or a higher concentration of radiogenic elements in the core or a combination of the two is required. Arguments have been made for and against the scenarios of the existence of high amount of radiogenic elements in the core or the high heat flux across the CMB (Labrosse et al., 1977; Davies, 1998; Buffet et al., 2000; Labrosse, 2003; McDonough, 2003; Nimmo et al., 2004;

Corgne et al., 2007; Davies, 2007; Gillet et al., 2011). However, one or the other should be unavoidable. High thermal conductivity has implications on the dynamics of the earth's magnetic field by affecting two important numbers: the ohmic diffusion time (the time specific to the slowest decaying dipole mode to fall by a factor of 1/ρ in the absence of a dynamo) and also the magnetic Reynolds number (R_m), which is a measure of the rate of generation of magnetic energy by a given flow field. High thermal conductivity (low electrical resistivity) lengthens the ohmic diffusion time to 50 kyr leading to an increase in the dipole decay time from 25 to 75 kyr (Pozzo et al., 2013). As one other consequence of high thermal conductivity, it increases R_m, making dynamo action possible with lower flow speeds and less power required from thermal and compositional convection (Pozzo et al., 2013). In connection with the recently proposed high thermal conductivity of the Earth's core, the obtained thermal conductivity values from the present research seem to lie within the recently proposed lower range of the new estimates of the thermal conductivity of Earth's outer core.

CHAPTER 7

7 Conclusion and Future Research

7.1 Conclusion

The electrical resistivity of solid and liquid Fe and Fe17Si was measured at 2 GPa and within the range of 2-5 GPa, respectively. Special attention was paid in the investigation of the previous challenges in resistance measurements in connection with the contaminations originating from the electrode materials and also the dominant role of the electrode resistances in the final results.

EMP analysis in addition to physical calculations made it clear that, high heating rate and circuit configuration are two key factors in order to have a resistance signal that is purely from the sample devoid of any geometrical or chemical perturbation. Taking into account these factors, it was possible for the first time to observe the electrical resistivity of Fe17Si alloy within liquid state at high pressure.

Using the resistivity results from the current research, TCR and PCR values of Fe17Si were calculated and the following corrections to the previous works on Fe17Si under high pressure were:

1. For the first time, the magnetic transition signal for Fe17Si is observed very clearly with a transition temperature that demonstrates a very slight dependence on pressure ($9^oC/GPa$).

2. Based on the present study results, for the first time it became possible to study the order-disorder-like transitions in solid Fe17Si and investigate their strong pressure dependency so that this transition shifted towards higher temperature with increasing pressure ($43.4^oC/GPa$).

3. As a new finding in the present research, it was proven that contrary to the electrical resistivity behavior of pure Fe, ρ(T) values of Fe17Si do not show any jump at the melting but exhibit a drop. This phenomenon was reported to happen at room pressure for Si concentrations between 25-60 wt% (Baum et al., 1967) and it is for the first time to report the same trend under pressure ranges from 2-5 GPa on 17wt%Si. Accordingly, calculated TCR values at the melting boundary of Fe17Si also show a negative sign in opposite to that of pure Fe. TCR values did not follow clear trend with respect to pressure as was reported before (Yang, 1999) but they show a broadly decreasing trend with much scatter. The average values of TCRs within the melting are of the order of $-4\times10^{-4} \pm 1.6\times10^{-4}\ K^{-1}$.

4. The higher the pressure, the wider will be the temperature interval that TCR values preserve the negative sign in the liquid state.

5. PCR values in liquid are negative and are strongly pressure dependent.

6. The electrical resistivity of Fe17Si in the pressure range 2-5 GPa at the melting point decreases from 1.73×10^{-6} Ωm at 2.32 GPa to 1.06×10^{-6} Ωm at 5 GPa. The resistivity values are comparable with liquid pure Fe resistivities at 5 GPa but higher than pure Fe by a factor of 1.4 at 2 GPa. It is shown that as the pressure increases, the difference in electrical resistivity between pure Fe and Fe17Si alloy decreases. If the low pressure electrical resistivity behavior is considered valid at higher pressures, Si is considered as a strong potential candidate for the Earth's core which can satisfy geodynamo sustainability requirements. However, as there are not enough data for other light elements, no comparison can be made between electrical resistivity of Fe-Si alloys and alloys with other light elements in order to validate or weaken the possibility of the presence of Si as a light alloying element in the core.

7. Linearly extrapolated resistivity values based on the data from the highest pressure attained in the current study (5GPa) to the CMB have yielded a range of 8.16×10^{-7}Ωm to 8.41×10^{-7}Ωm and power law extrapolation of liquid data electrical resistivities yielded a range of 9×10^{-7}Ωm to 9.4×10^{-7}Ωm . These are in a very close agreement to the reported resistivity values in recent reported calculations, which ultimately leads to the conclusion that the thermal conductivities of the Earth's core are 2 to 3 times higher than what was thought before.

7.2 Future research

On the basis of the current research the following suggestions are proposed:

- In terms of high pressure cell design, the circuit contribution to resistivity measurement of FeSi alloys is much more serious and challenging than in the case of pure Fe. This is the case because of the decrement of the ρ(T) of FeSi alloys within the melt which can be very easily masked by the resistance contribution of the rest of the circuit. It was tried to make this contribution as small as possible for the current study in which a two wire method was deployed. However, as for the future experiments, using a four wire method is strongly recommended which would avoid the need for corrections required for the 2-wire method.
- Considering Pt as an ideal electrode for high pressure - temperature studies, there is still a serious need for having electrical resistivity information of Pt behavior specifically under high pressure so that its contribution to the sample resistivity can be known.
- Regarding the electrical resistivity results that were inferred from the current study, a higher range of pressure should be covered in order to get a more realistic and clear picture about PCR and TCR changes with the pressure. This could have a profound impact on the validity of the currently suggested electrical resistivity extrapolated values.
- Also, for having a more realistic picture of the Earth's core electrical resistivity, other than binary alloying system of Fe-Si, there is a serious need of investigating electrical resistivities of ternary alloying systems of Fe-Si-X ,with X being chosen from the potential light element candidates for the Earth's core such as S,O,C and H.

References

Alfé, D., Gillan, M. J., Price, G. D. (2002a). Ab initio chemical potentials of solid and liquid solutions and the chemistry of the Earth's core. J. Chem. Phys. 116, 7127-36.

Alfé, D., Gillan, M. J., Price, G. D. (2002b). Composition and temperature of the Earth's core constrained by combining ab initio calculations and seismic data. Earth Planet. Sc. Lett. 195, 91-98.

Allègre, C. J., Poirier, J. P., Humler, E., Hofman, A. (1995). The chemical composition of the Earth. Earth Planet. Sc. Lett. 134, 515-526.

Allen, P. B. (1980). Superconductivity in d- and f-band Metals. Edited by H. Suhl and M. B. Maple (Academic, New York), 291-304.

Anderson, O.L. (1986). Properties of Fe at the Earth's core conditions. Geophys. J. Roy. Astr . S. 84, 561-579.

Anderson, W.W., and Ahrens, T.J. (1994). An equation of state for liquid iron and implications for the Earth's core, J. Geophys. Res., 99, 4273-4284.

Antonangeli, D., Siebert, J., Badro, J., Farber, D.L., Fiquet,G., Morard,G., Ryerson,F.J. (2010). Composition of the Earth's inner core from high pressure sound velocity measurements in Fe-Ni-Si alloys. Earth Planet Sc. Lett. 295, 292-296.

Asahara, Y., Frost, D.J., Rubie, D.C. (2007). Partitioning of FeO between magnesiowürstite and liquid Fe at high pressures and temperatures: implications for the composition of the Earth's outer core. Earth Planet. Sc. Lett. 257, 435-449.

Asanuma, H., Ohtani, E., Akai, T., Terasaki, H., Kamada, S., Hirao, N., Sata, N., Ohishi, Y. (2008). Phase relations of Fe-Si alloy up to core conditions: implications for the Earth inner core. Geophys. Res. Lett. 35, L1 2307.

Backlund, M.G. (1961). An experimental investigation of the electrical and thermal conductivity of Fe and some dilute Fe alloys at temperatures above 100°K. J Phys Chem Solids. 20 (1), 1-16.

Badding, J.V., Hemley, R.J., Mao, H.K. (1991). High-pressure chemistry of hydrogen in metals: In situ study of Fe hydride. Science 253, 421-424.

Badro, J., Fiquet, G., Guyot, F., Gregoryanz, E., Occelli, F., Antonangeli, D., d'Astuto, M. (2007). Effect of light elements on the sound velocity of solid Fe: implications for the composition of Earth's core. Earth Planet. Sc. Lett. 254, 233-238.

Bannikh, O.A., Budberg, P.B., Alisova, S.P. (1986). Phase equilibrium diagrams of the binary and multicomponent systems on the Base of Fe, Metallurgiya, Moscow, 429.

Baum, B.A., Gel'd, P.V., Tyagunov, G.V. (1967). Resistivity of ferrosilicon alloys in the temperature range 800-1700 ^{o}C. Phys. Metals and Metallog, 24 (1), 181-184 USSR English Transl.

Bi, Y., Tan, H., Jing, F.Q. (2002). Electrical conductivity of Fe under shock compression up to 200 GPa. J. Phys. Condens. Matter, 14, 10849-10854.

Birch, F. (1952). Elasticity and constitution of the Earth interior. J. Geophys. Res. 57, 227-86.

Bohnenkamp, U., Sandström, R. Grimvall, G. (2002). Electrical resistivity of steels and face-centered-cubic Fe. J. Appl. Phys. 92, 4402-4406.

Boness, D.A., Brown J.M., McMahan A.K. (1986). The electronic thermodynamics of Fe under Earth core conditions, Phys. Earth Planet. Inter., 42, 227-240.

Bridgman, P.W. (1957). Effects of pressure on binary alloys, V and VI. Proc. Am. Acad. Arts Sci. 84, 131-216.

Brosh, E., Makov, G., Shneck, R.Z. (2009). Thermodynamic analysis of high-pressure phase equilibria in Fe–Si alloys, implications for the inner-core. Phys. Earth Plan Int. 172, 289-298.

Buffett, B., Garnero, E., Jeanloz, R. (2000). Sediments at the top of Earth's core. Science, 290, 1338-1342.

Bukowinski, M.S.T. (1976). On the electronic structure of Fe at core pressures. Physics of the Earth and Planetary Interiors, 13, 57-66.

Bundy, F.P. (1961). The effects of pressure on emf of thermocouples. J. Appl. Phys., 32(3), 483-488.

Cava, R.D., Botta, W.J., Kiminami, C.S., Olzon-Dionysio, M., Souza, S.D., Jorge, Jr., A.M., Bolfarini, C. (2011). Ordered phases and texture in spray-formed Fe-5 wt%Si. Journal of Alloys and Compounds, 509, 260-264.

Chen, B., Gao, L., Funakoshi, K., Li, J. (2007). Thermal expansion of Fe-rich alloys and implications for the Earth's core. Proc. Nat. Acad. Sci. U.S.A 104 (22), 9163-9167.

Ciurzyfiska, W., Zbroszczyk, J., Olszewski, J., Frackowiak, J., Narita, K. (1994). Order-disorder effect on magnetic properties of rapidly quenched Fe-6.5%Si alloy. J. Magn.Magn. Mater. 133, 351-353.

Ciurzyńska, W.H. (1998). Magnetic susceptibility disaccommodation and Mössbauer studies of high silicon–Fe alloy obtained by different methods. Journal of Magnetism and Magnetic Materials. 188(3), 346-352.

Corgne, A., Keshav, S., Fei, Y.W., McDonough, W.F. (2007). How much potassium is in the Earth's core? New insights from partitioning experiments. Earth Planet. Sc. Lett. 256, 567-576.

Corgne, A., Siebert, J., Badro, J. (2009). Oxygen as a light element: A solution to single-stage core formation. Earth Planet. Sc. Lett. 288, 108-114.

Corson, M.G. (1928). The constitution of the Fe-silicon alloys, particularly in connection with the properties of corrosion-resisting alloys of this composition. Trans. Am. Inst. Min. Met. Eng. 80, 75.

Côté A.S.,Vôcadlo, L., Brodholt, J.P.(2008). Light elements in the core: effects of impurities on the phase diagram of iron. Geophys. Res. Lett. 35(5), L05306.

Cusack, N.E. (1963). The electronic properties of liquid metals. Rept. Progr. Phys., 26, 361-409.

Dasgupta, R., Buono, A., Whelan, G. Walker, D. (2009). High pressure melting relations in Fe–C–S systems: implications for formation, evolution, and structure of metallic cores in planetary. Geochimica et Cosmochimica Acta., 73(21), 6678-6691.

Davies, G. (1998). Topography: a robust constraint on mantle fluxes. Chem. Geol., 145, 479-489.

Davies, G. (2007). Mantle regulation of core cooling: a geodynamo without core radioactivity? Phys. Earth Planet. Inter. 160, 215-229.

de Koker, N., Steinle-Neumann, G., Vlcek, V. (2012). Electrical resistivity and thermal conductivity of liquid Fe alloys at high P and T, and heat flux in Earth’s core. Proc. Natl Acad. Sci., 109, 4070-4073.

Deng, L., Seagle, C., Fei, Y., Shahar, A. (2013). High pressure and temperature electrical resistivity of Fe and implications for planetary cores. Geophys. Res. Lett. 40, 33.

Dobson, D.P., Crichton, W.A., Bouvier, P., Vocadlo, L., Wood, I.G. (2003). The equation of state of CsCl-structured FeSi to 40 GPa: implications for silicon in the Earth's core. Geophys. Res. Lett., 30.

Domenicali , C.A., Otter, F.A. (1955). Thermoelectric power and electrical resistivity of dilute alloys of silicon in copper, nickle and Fe. J. Appl. Phys., 26, 377.

Drake, M.J. Righter, K. (2002). Determining the composition of the Earth. Nature, 416, 39-44.

Elsasser, W.M., Isenberg, I. (1949). Electronic phase transition in Fe at extreme pressures. Phys. Rev., 76, 469.

Fischer, R.A., Campbell, A.J., Caracas, R., Reaman, D.M., Dera, P., and Prakapenka, V.B. (2012). Equation of state and phase diagram of Fe-16Si alloy as candidate component of Earth’s core. Earth and Planetary Science Letters., 357, 268-276.

Fisk, Z., Webb, G.W. (1976). Saturation of the high-temperature normal-state electrical resistivity of superconductors. Phys. Rev. Lett., 36, 1084.

Fitoussi, C., Bourdon, B., Kleine, T., Oberli, F., Reynolds, B.C. (2009). Si isotope systematics of meteorites and terrestrial peridotites: implications for Mg/Si fractionation in the solar nebula and for Si in the Earth’s core. Earth Planet. Sci. Lett., 287, 77-85.

Fu, H.D., Zhang, Z.H., Yang, Q., Xie, J.X. (2011). Effects of precipitated phase and order degree on bending properties of an Fe-6.5 wt%Si alloy with columnar grains. Journal of Materials Research., 26, 1711-1718.

Fukai, Y. (1984). The Fe-water reaction and the evolution of the Earth. Nature. 308, 174-175.

Funtikov, A.I. (2007). Shock compression of Fe–silicon alloys with reference to the possible concentration of silicon in the Earth’s core. Izvestiya. Phys. Solid Earth., 43, 554-558.

Gardiner, R.B., Stacey, F.D. (1971). Electrical resistivity of the core. Phys. Earth Planet. Int., 4, 406-410.

Garg, A.B., Vijayakumar, V., Godwal, B.K. (2004). Electrical resistance measurements in a diamond anvil cell to 40 GPa on ytterbium. Rev. Sci. Instrum., 75, 2475.

Gessmann, C.K., Wood, B. J., Rubie, D.C., Kilburn, M.R. (2001). Solubility of silicon in liquid metal at high pressure: Implications for the composition of the Earth's core. Earth Planet. Sci. Lett., 184(2), 367-376.

Gillet, N., Schaeffer, N., Jault, D. (2011). Rationale and geophysical evidence for quasi-geostrophic rapid dynamics within the Earth's outer core. Phys. Earth Planet. Inter., 187, 380-390.

Glaser, F. W., Ivanick, W. (1956). Study of the Fe-Si order-disorder transformation. J. Met., 8, 1290.

Gomi,H., Ohta,K., Hirose,K., Labrosse,S., Caracas,R., Verstraete,M.J., Hernlund,J.W. (2013). The high conductivity of iron and thermal evolution of the Earth’s core. Physics of the Earth and Planetary Interiors., 224, 88-103.

Gu,T.K., Qin, J.Y., Xu,C.Y. and Bian, X.F. (2004). Structural, bonding, and dynamical properties of liquid Fe-Si alloys: An *ab initio* molecular-dynamics simulation. Phys. Rev. B., 70, 144204.

Gubbins, D., Alfe`, D., Masters, T. G., Price, D. (2004). Gross thermodynamics of 2-component core convection. Geophys. J. Int., 157, 1407-1414.

Gunnarsson, O., Calandra, M., Han, J.E. (2003). Colloquium: Saturation of electrical resistivity. Rev. Mod. Phys., 75, 1085.

Guyot, F., Zhang, J., Martinez, I., Matas J., Ricard, Y., Javoy, M. (1997). P-V-T measurements of Fe silicide (e-FeSi)-Implications for silicate-metal interactions in the early Earth. Eur. J. Mineral., 9, 277-285.

Hansen, M. (1958), Constitution of binary alloys, 2nd edn. New York: McGraw-Hill.

Hillgren, V.J, Gessmann, C.K, Li, J. (2000). An experimental perspective on the light element in Earth's core. Origin of the earth and moon. edited by R.M. Canup and K. Righter and 69 collaborating authors. Tucson: University of Arizona Press., 245-263

Hirao, N., Ohtani, E., Kondo, T., Kikegawa, T. (2004). Equation of state of Fe-silicon alloys to megabar pressure. Phys. Chem. Miner., 31, 329-336.

Hirose, K., Gomi, H., Ohta, K., Labrosse, S., Hernlund, J. (2011). The high conductivity of Fe and thermal evolution of the Earth’s core. Mineral. Mag., 75, 1027.

Hirose, K., Labrosse, S., Hernlund, J. (2013). Composition and state of the core. Annual Review of Earth and Planetary Sciences., 41, 657-691.

Hirschmann, M.M., Dasgupta, R. (2009).The H/C ratios of Earth’s near-surface and deep reservoirs, and consequences for deep Earth volatile cycles. Chem. Geol., 262, 4-16.

Hultgren, R.P., Desai, D., Hawkins, D.T., Gleiser, M., Kelley, K.K. (1973). Selected values of the thermodynamic properties of binary alloys. P. 871, John Wiley and Sons, N.Y.

Iota, V., Klepeis, J.P., Yoo, C., Lang, J., Haskel, D., Srajer, G. (2007). Electronic structure and magnetism in compressed 3*d* transition metals. Appl. Phys. Lett., 90, 042505.

Isaev, E.I., Skorodumova, N.V., Ahuja, R., Vekilov, Y.K., Johansson, B. (2007). Dynamical stability of Fe-H in the Earth's mantle and core regions. Proc Nat Acad Sci USA., 104, 9168-9171.

Ito, E., Morooka, K. (1995). Reactions between molten Fe and silicate melts at high pressure: Implications for the chemical evolution of Earth's core. J. Geophys. Res., 100, 5901-5910.

Javoy, M. (1995). The integral enstatite chondrite model of the Earth. Geophys. Res. Lett., 22, 2219-2222.

Jeanloz, R. (1990). The nature of the Earth's core, Annu. Rev. Earth Planet. Sci., 18, 357-386.

Keeler, R.N., Mitchell, A.C. (1969). Electrical conductivity, demagnetization, and the high-pressure phase transition in shock-compressed Fe. Solid State Communications., 7, 271-274.

Keeler, R.N., Royce, E.B. (1971). Physics of high energy density. (eds Caldirola, P. and Knoepfel, H.) 106-125 Proc. Int. Sch. Phys. Enrico Fermi., 48.

Kilburn, M.R., Wood, B. J. (1997). Metal-silicate partitioning and the incompatibility of S and Si during core formation. Earth Planet. Sci. Lett., 152,139-148.

Kmetko, E.A. (1971). Calculated effects of compression upon the band structure and density of states of several metals, electronic density of states. Nat. Bur. Stand. Spec. Publ., 323, 67.

Konôpková, Z., Lazor, P., Goncharov A.F., Struzhkin, V.V. (2011). Thermal conductivity of hcp Fe at high pressure and temperature. High Pressure Research., 31, 228.

Kubaschewski, O. (1982). Fe-binary phase diagrams. New York: Springer.

Kudrnovský, J., Christensen, N.E., Andersen, O.K. (1991). Electronic structures and magnetic moments of $Fe_{3+y}Si_{1-y}$ and $Fe_{3-x}V_xSi$ alloys with DO_3-derived structure, Physical Review B (Condensed Matter), 43(7), 5924-5933.

Labrosse, S., Poirier, J. P., Le Mouël, J. L. (1997). On cooling of the Earth's core. Phys. Earth Planet. Inter., 99, 1-17.

Labrosse, S., Poirier, J.P, Le Moüel, J.L. (2001). The age of the inner core. Earth Planet. Sci. Lett., 190,111-23.

Labrosse, S. (2003). Thermal and magnetic evolution of the Earth's core. Phys. Earth Planet. Inter.,140,127-143.

Lay, T., Hernlund, J., Buffett, B. (2008). Core-mantle boundary heat flow. Nature Geosci., 1, 25-32.

Leger, J.M., Loriers-Susse, C., Vodar, B. (1972). Pressure effect on the curie temperatures of transition metals and alloys. Phys. Rev. B6., 4250- 4261.

Li, J., Agee, C.B. (2001).The effect of pressure, temperature, oxygen fugacity and composition on partitioning of nickel and cobalt between liquid Fe-Ni-S alloy and silicate liquid: implications for the Earth' core formation. Geochim. Cosmochim. Acta., 65, 1821-32.

Li, J., Fei, Y. (2003). Experimental constraints on core composition. Treatise on Geochemistry, Volume 2. Editor: Richard W. Carlson. Executive Editors: Heinrich D. Holland and Karl K. Turekian, 521-546.

Lin, J.F., Campbell, A.J., Heinz, D.L. (2003a). Static compression of Fe-silicon alloys: Implications for silicon in the Earth's core. J. Geophys. Res., 108, B1, 2045.

Lin, J.F., Heinz, D.L., Campbell, A.J., Devine, J. M., Shen, G. (2002). Fe-silicon alloy in Earth's core? Science, 295, 313-315.

Lin, J.F., Scott, H.P., Fischer, R.A., Chang, Y.Y., Kantor, I., Prakapenka, V.B. (2009). Phase relations of Fe-Si alloy in Earth's core. Geophy. Res. Lett., 36.

Lin, J.F. , Struzhkin, V.V., Sturhahn, W., Huang, E., Zhao, J.Y., Hu, M.Y , Alp, E.E., Mao, H.K., Boctor, N., Hemley, R.J. (2003b). Sound velocities of iron–nickel and iron–silicon alloys at high pressures, Geophys. Res. Lett., 30.

Litasov, K.D., Sharygin, I.S., Dorogokupets, P.I., Shatskiy, P.N., Sokolova, P.S., Ohtani, E., Li, J., and Funakoshi, K. (2013). Thermal equation of state and thermodynamic properties of iron carbide Fe_3C to 31 GPa and 1473 K, Journal of Geophysical Research: Solid Earth, 118 (10), 5274-5284.

Littmann, M.F. (1971). Fe and silicon-Fe alloys. IEEE Trans. Magn., MAG., 7(1), 48-60.

Lota,V. Klepeis, J.H.P.C., Yoo, S., Lang, J., Haskel, D., andSrajer, G. (2007). Electronic structure and magnetism in compressed 3d transition metals, Appl. Phys. Lett.,90, 042505.

Mao, Z., Lin, J. F., Liu, J., Alatas, A., Gao, L., Zhao, J., Mao, H.K. (2012). Sound velocities of Fe and Fe-Si alloy in the Earth's. Proc. Natl. Acad. Sci. USA, 109(26),10239-44.

Massalsky, T. (Eds.). (1996). Binary alloy phase diagrams, 2nd Edition, ASM International, Materials Park, OH.

Matassov, G. (1977). The electrical conductivity of Fe–silicon alloys at high pressures and the Earth's core. Ph.D. Thesis. Lawrence Livermore Laboratory, University of California, CA.

McDonough, W.F. (2003). Compositional model for the Earth's core. In Treatise on Geochemistry, Vol. 2: The Mantle and Core, ed. RW Carlson, pp. 547-68. Oxford: Elsevier-Pergamon.metals- in situ study of Fe hydride. Science 253, 421-24.

Miller, N.A. (2009). Melting and phase relations in Fe-silicon alloys with applications to the Earth's core. M.Sc. Thesis. University of Maryland (College Park, Md.).

Mirzoev,A.A., Sobolev, A.N. (2011). Liquid-liquid phase transition: is it possible in Fe melts? EPJ Web of Conferences, 15, 01012.

Mooij, J.H. (1973). Electrical conduction in concentrated disordered transition metal alloys. Phys. Status Solidi A., 17, 521-530.

Morard, G., Andrault, D., Guignot, N., Siebert, J., Garbarino, G., Antonangeli, D. (2011). Melting of Fe-Ni-Si and Fe-Ni-S alloys at megabar pressures: Implications for the core-mantle boundary temperature. Phys. Chem. Minerals., 38, 767-776.

Morard, G., Sanloup, C, Guillot, B., Fiquet, G., Mezouar, M., Perrillat, J.P., Garbarino, G., Mibe, K., Komabayashi, T., and Funakoshi, K. (2008). In situ structural investigation of Fe-S-Si immiscible liquid system and evolution of Fe-S bond properties with pressure, J. Geophy. Res., 113, B10205.

Nimmo, F., Price, G.D., Brodholt, J., Gubbins, D. (2004). The influence of potassium on core and geodynamo evolution. Geophys. J. Int., 156,363-76.

Nishino,Y., Inoue, S.Y, Asano, S. (1993). Anomalous temperature dependence of the electrical resistivity in binary and pseudobinary alloys based on Fe3Si. Phys. Rev., B Condens. Matter., 48 (18), 13607-13613.

Numakura, K., Tsugawa, A. (1972). Magnetic and electric properties of Fe-silicon alloys. Science reports of the Research Institutes, Tohoku University. Ser. A, Physics, chemistry and metallurgy, 24 pp. 48-60, Tohoku University.

O'Neill, H.S.C., Canil, D., Rubie, D.C. (1998). Oxide-metal equilibria to 2500◦C and 25 GPa: implications for core formation and the light component in the Earth's core. J. Geophys. Res., 103, 12239-60.

Ohnuma, I., Abe, S., Shimenouchi, S., Omori, T., Kainuma, R., Ishida, K. (2012). Experimental and thermodynamic studies of the Fe–Si binary system. ISIJ International, 52(4), 540-548.

Poirier, J.P. (1994). Light elements in the Earths' core: a critical review. Phys. Earth Planet. Inter., 85, 319-37.

Powell, R.W. (1953). The electrical resistivity of liquid Fe, Philos. Mag., 44, 772-775.

Pozzo, M., Alf', D., Davies, C., Gubbins, D. (2013). Transport properties for liquid silicon-oxygen-Fe mixtures at Earth's core conditions. Physical Review B - Condensed Matter and Materials Physics, 87.

Pozzo, M., Davies, C., Gubbins, D., Alfè, D. (2012).Thermal and electrical conductivity of Fe at Earth's core conditions. Nature, 485, 355-358.

Pry, R. H. (1959). Development of metallurgical structures and magnetic properties in Fe. Silicon Alloys J. Appl. Phys., 30, S189.

Rhee, J.Y., Harmon, B.N. (2004). Metamagnetic behavior of Fe3*M* (*M*=Al and Si) alloys at high pressure, Physical Review B, 70, 094411.

Ricolleau, A., Fei, Y.W., Corgne, A., Siebert, J., Badro, J. (2011). Constraints on oxygen and silicon contents of Earth's core from metal-silicate partitioning experiments at high pressure and temperature. Earth Planet. Sci. Lett., 310, 409-421.

Ringwood, A.E., Hibberson, W. (1991). Solubilities of mantle oxides in molten Fe at high pressures and temperature: implication for the composition of the Earth's core. Earth Planet. Sci. Lett., 102, 235-251.

Rossiter, P.L. (1987). The electrical resistivity of metals and alloys. Cambridge University Press, ISBN-10: 0521249473

Ros-Yanez, T., Houbaert, Y., Fischer, O., Schneider, J. (2003). Production of high silicon steel for electrical applications by thermomechanical processing. J. Mater Process Tech., 143, 916-921.

Ros-Yanez, T., Ruiz, D., Lopez, D., Hilgert, T., Dupré, L., Vandenberghe, R.E., Houbaert, Y. (2005). Influence of ordering phenomena on the magnetostriction of high Si alloys for electrical applications. Journal of Applied Physics, 97(10), 10F901-10F901-3.

Rubie, D.C., Gessmann, C.K., Frost, D.J. (2004). Partitioning of oxygen during core formation on the Earth and Mars. Nature, 429, 58-61.

Ruiza, D., Ros_Yanez, T., Vandenbossche, L., Dupre, L.,Vandenberghe, R.E., Houbaer, Y. (2005). Effect of atomic order on the electrical and magnetic properties of $Fe_{100-x}Si_{x\ (6 < x < 14)}$ alloys. J. Magn. Magn. Mater., 290-291, 1423.

Sakai, T., Kondo, T., Ohtani, E., Terasaki, H, Endo, N., Kuba, T., Suzuki, T., Kikegawa, T. (2006). Interaction between Fe and post-perovskite at core-mantle boundary and core signature in plume dource region, Geophys. Res. Lett., 33, L15137.

Sakamaki, K., Takahashi, E., Nakajima, Y., Nishihara, Y., Funakoshi, K., Suzuki, T., Fukai, Y. (2009). Melting phase relation of FeHx up to 20 GPa: Implication for the temperature of the Earth's core. Physics of Earth and Planetary Interiors, 174, 192-201.

Sanloup, C., Fei, Y. (2004). Closure of the Fe-S-Si liquid miscibility gap at high pressures. Phys. Earth Planet. Int., 147, 57-74.

Sanloup ,C., Guyot, F, Gillet, P., Fiquet, G., Hemley, R.J., Mezouar, M., and Martinez, I.

(2000). Structural changes in liquid Fe at high pressures and high temperatures from Synchrotron Xray Diffraction. Europhys. Lett., 52, 151.

Sanloup, C., Westrenen, W.V, Dasgupta, R., Maynard-Casely, H., Perrillat, J.P. (2011). Compressibility change in iron-rich melt and implications for core formation models. Earth and Planetary Science Letters, 306, 118-122.

Sata, N., Hirose, K., Shen, G., Nakajima, Y., Ohishi, Y., Hirao, N. (2010).Compression of FeSi, Fe_3C, $Fe_{0.95}O$, and FeS under the core pressures and implication for light element in the Earth's core. J. Geophys. Res.,115, B09204.

Satish-Kumar, M., So, H., Yoshino, T., Kato, M., Hiroi, Y. (2011). Experimental determination of carbon isotope fractionation between Fe carbide melt and carbon: C-12-enriched carbon in the Earth's core? Earth Planet Sc Lett., 310(3-4), 340-348.

Secco, R. A., Schloessin, H.H. (1989). The electrical resistivity of solid and liquid Fe at pressures up to 7 GPa. J. Geophys. Res., 94, 5887-5894.

Sha, X., Cohen, R.E. (2011). First-principles studies of electrical resistivity of Fe under pressure. J. Phys.: Condens. Matter, 23, 075401.

Shahar, A., Hillgren, V.J., Young, E.D., Fei, Y. Macris, C.A., Deng, L. (2011). High-temperature Si isotope fractionation between Fe metal and silicate. Geochim. Cosmochim. Acta., 75, 7688.

Shahar, A., Ziegler, K., Young, E.D., Ricolleau, A., Schauble, E., Fei, Y. (2009). Experimentally determined Si isotope fractionation between silicate and Fe metal and implications for Earth's core formation. Earth Planet. Sci. Lett.,288, 228-34.

Sherman, D.M. (1991). Chemical bonding in the outer core: high pressure electronic structures of oxygen and sulfur in metallic Fe. J. Geophys. Res., 96, 18029-18036.

Sherman, D.M. (1995). Stability of possible Fe-FeS and Fe-FeO alloy phases at high pressure and the composition of the Earth'core. Earth Planet. Sci. Lett., 132, 87-98.

Sherman, D.M. (1997). The composition of the Earth's core: constraints on S and Si vs. temperature. Earth Planet. Sci. Lett., 153,149-155.

Shibazaki,Y., Ohtani, E., Fukui, H., Sakai, T., Kamada, S., Ishikawa, D., Tsutsui, S., Baron, Alfred Q.R., Nishitani, N., Hirao, N., and Takemura, k. (2012). Sound velocity measurements in dhcp-FeH up to 70 GPa with inelastic X-ray scattering: implications for the composition of the Earths' core. Earth Planet. Sci. Lett., 313-314, 79-85.

Siebert, J., Guyot, F., Malavergne, V. (2005). Diamond formation in metalcarbonate interactions, Earth Planet. Sci. Lett., 229 205-216.

Spektor, E.Z., Snezhko, O.M., Baum, B.A., and Gel'd, P.V. (1971). Constitution of liquid iron-silicon alloys. Soviet Physics Journal, 14(10), 1364-1367.

Stacey, F. D., Anderson, O. L. (2001). Electrical and thermal conductivities of Fe–Ni–Si alloy under core conditions. Phys. Earth Planet. Interiors, 124, 153-162.

Stacey, F.D., Davis, P.M. (2008). Physics of the Earth. Cambridge, UK: Cambridge University Press.

Stacey, F.D., Loper, D.E. (2007). A revised estimate of the conductivity of Fe alloy at high pressure and implications for the core energy balance. Physics of the Earth Plan. Int., 161, 13-18.

Stevenson, D.J. (1981). Models of the Earth's core. Science 214,611-19.

Stixrude, L., Wasserman, E., Cohen, R.E. (1997). Composition and temperature of Earth's inner core. J. Geophys. Res. [Solid Earth], 102, 24729-24739.

Strong, H.M., Tuft, R.E., Hanneman, R.E. (1973). The Fe fusion curve and γ-δ-l triple point. Metall. Trans., 4. 2657-2661.

Tateno, S., Hirose, K., Ohishi, Y., Tatsumi, Y. (2010). The structure of Fe in Earth's inner core, Science, 359-361.

Tateyama, R., Ohtani, E., Terasaki, H., Nishida, K., Shibazaki, Y., Suzuki, A., Kikekawa, T. (2011). Density measurements of liquid Fe-Si alloys at high pressure using the sink-float method. Phys. Chem. Miner., 38, 801-7.

Tsuei, C.C., (1986). Nonuniversality of the Mooij correlation-the temperature coefficient of electrical resistivity of disordered metals. Phys. Rev. Lett., 57 (15), 1943-1946.

Tuff, J., Wood, B. J., Wade, J. (2011). The effect of Si on metal-silicate partitioning of siderophile elements and implications for the conditions of core formation. Geochim. Comoschim. Acta., 75, 673-690.

Van Zytveld, J.B. (1980). Electrical resistivities of liquid transition metals. J. Phys. Colloq. Orsay Ft., 41, C8.503-C8.506.

Varga, L.K., Mazaleyrat, F., Kovac, J., Greneche, J.M. (2002). Structural and magnetic properties of metastable Fe_{1-x} Si_x (15<x<.34) alloys prepared by rapid quenching technique. J. Phys.: Condens. Matter, 14, 1985-2000.

Vočadlo, L. (2007). Ab initio calculations of the elasticity of Fe and Fe alloys at inner core conditions: evidence for a partially molten inner core. Earth Planet. Sci. Lett., 254, 227.

Wade, J., Wood, B.J. (2005). Core formation and the oxidation state of the Earth. Earth Planet. Sci. Lett., 236, 78-95.

Weiss, R.J., Marotta, A.S. (1959). Spin-dependence of the resistivity of magnetic metals. Journal of Physics and Chemistry of Solids, 9(3–4), 302-308.

Wiesmann, H., Gurvitch, M., Lutz, H., Ghosh, A.K., Schwarz, B., Strongin, M., Allen, P. B., Halley, J.W. (1977). Simple model for characterizing the electrical resistivity in *A*-15 superconductors. Phys. Rev. Lett., 38, 782.

Williams, Q., Jeanloz, R. (1990). Melting relations in the Fe-sulfur system at ultra-high pressures: implications for the thermal state of the Earth. J. Geophys. Res., 95, 19299-19310.

Wittig, J.E, Frommeyer, G. (2008). Deformation and fracture behavior of rapidly solidified and annealed Fe-silicon alloys. Metallurgical and materials transactions A- physical metallurgy and materials science, 39A, 252-265.

Wood, B.J. (1993). Carbon in the core. Earth Planet. Sci. Lett., 117, 593-607.

Wood, B.J., Walter, M.J., Wade, J. (2006). Accretion of the Earth and segregation of its core. Nature ,441, 825-33.

Wood B., Li J., Shahar A. (2013). Carbon in the Core: Its Influence on the Properties of Core and Mantle, Reviews in Mineralogy and Geochemistry, 75, 231-250.

Wysocki, A.L., Sabirianov, R.F., van Schilfgaarde, M., Belashchenko, K.D. (2009). First-principles analysis of spin-disorder resistivity of Fe and Ni, Physical Review B, 80, 224423.

Yang, H. (1999). Melting behavior, electrical resistivity, viscosity of Fe-Si alloys at high pressures: Implications for outer core dynamics. Ph.D. diss., The University of Western Ontario (Canada).

Yang, H., Secco, R.A. (1999). Melting boundary of Fe-17%Si up to 5.5 GPa and the timing of core formation. Geophys. Res. Lett., 26,263-266.

Yensen, T.D. (1915). Magnetic and other properties of Fe-silicon alloys melted in vacuo Trans. Am. Inst. Electr. Eng., 34, 23.

Yousouf, M., Sahu, P.C., Rajan, K.G. (1986). High-pressure and high-temperature electrical resistivity of ferromagnetic transition metals: Nickel and Fe. Phys. Rev. B, 3411, 8086-8100.

Zhang, J., Guyot F. (1999). Experimental study of the bcc-fcc phase transformations in the Fe-rich system Fe-Si at high pressures. Phys. Chem. Miner., 26, 419-424.

Ziegler, K., Young, E.D., Schauble, E.A., Wasson, J.T. (2010). Metal–silicate silicon isotope fractionation in enstatite meteorites and constraints on Earth's core formation. Earth and Planetary Science Letters, 295, 487- 496.

Zinov'ev, V.E., Abel'skii, Sh. Sh., Sandakova, M.I., Petrova, L.N., Gel'd, P.V. (1973). Matthiessen rule and high-temperature electrical resistivity of solid solutions of silicon in Fe. JETP, 36(6), 1174.

APPENDIX A

Results of electron microprobe analyses

Electron microprobe analyses for P2n and P1n series were performed using a CAMECA SX20 electron microprobe in the Microprobe Laboratory, Department of Earth Sciences, and University of Toronto. All analyses were carried out with a beam current of 15nA and an accelerating voltage of 20 kV. For S15, L11, L12 and L13, a JEOL JXA - 8900R Superprobe was deployed at the University of Alberta. The accelerating voltage was15 kV and the beam current was 15 nA. Results are tabulated in the following tables.

Table A.1 EMP results for P21 experiment.

Probe point	Si (wt%)	Fe (wt%)	Pt (wt%)	Totals (wt%)
1	4.10	32.86	61.70	98.66
2	7.62	23.86	68.40	99.88
3	2.45	34.73	61.52	98.69
4	3.28	33.83	61.60	98.72
5	8.61	22.76	68.46	99.83
6	4.01	33.01	61.79	98.81
7	5.60	26.23	67.21	99.04
8	3.70	13.68	35.49	52.86
9	2.44	34.58	61.10	98.12

Table A.2 EMP results for P22 experiment.

Probe point	Si (wt%)	Fe (wt%)	Pt (wt%)	Totals (wt%)
1	4.97	95.26	0.05	100.28
2	4.82	95.36	0.00	100.17
3	5.50	94.31	0.03	99.84
4	6.02	91.86	0.00	97.87
5	4.56	95.54	0.00	100.08
6	12.01	80.00	0.00	92.01
7	5.46	93.68	0.00	99.11
8	5.93	93.93	0.00	99.85
9	6.17	93.40	0.02	99.58
10	6.56	92.62	0.02	99.21

Table A.3 EMP results for P11 experiment.

Probe point	Si (wt%)	Fe (wt%)	Pt (wt%)	Totals (wt%)
1	0.84	97.38	0.93	99.14
2	0.85	98.14	0.99	99.98
3	1.71	97.65	1.01	100.37
4	1.11	97.18	0.97	99.26
5	1.37	97.04	1.05	99.46
6	3.91	93.90	1.66	99.46
7	3.85	94.41	1.65	99.91
8	3.12	95.45	1.53	100.10
9	1.50	95.88	1.17	98.55

Table A.4 EMP results for P12 experiment.

Probe point	Si (wt%)	Fe (wt%)	Pt (wt%)	Totals (wt%)
1	13.69	84.80	0.07	98.56
2	14.67	84.32	0.12	99.11
3	17.40	82.45	0.04	99.88
4	17.34	81.65	0.04	99.03
5	17.47	82.05	0.07	99.60
6	17.64	81.58	0.04	99.25
7	15.86	83.45	1.73	101.04
8	13.65	85.81	0.16	99.62
9	17.49	82.33	0.10	99.92
10	13.69	84.80	0.07	98.56
11	14.67	84.32	0.12	99.11
12	17.40	82.45	0.04	99.88

Table A.5 EMP results for P13 experiment.

Probe point	Si (wt%)	Fe (wt%)	Pt (wt%)	Totals (wt%)
1	0.03	98.96	0.07	99.06
2	0.02	99.18	0.14	99.34
3	12.21	87.47	0.09	99.76
4	13.63	79.43	6.52	99.58
5	16.51	82.96	0.09	99.56
6	17.29	82.50	0.01	99.80
7	16.87	82.69	0.03	99.59
8	12.24	87.90	0.04	100.18
9	11.29	88.10	0.08	99.47
10	0.03	98.96	0.07	99.06
11	0.02	99.18	0.14	99.34

Table A.6 EMP results for P14 experiment.

Probe point	Si (wt%)	Fe (wt%)	Pt (wt%)	Totals (wt%)
1	0.03	99.54	0.00	99.57
2	0.02	99.42	0.00	99.42
3	9.74	90.17	0.02	99.93
4	14.83	84.43	0.12	99.38
5	16.68	82.09	0.56	99.33
6	15.63	84.01	0.05	99.70
7	15.95	83.58	0.11	99.63
8	9.30	90.04	0.38	99.72
9	6.87	93.09	0.10	100.05
10	0.03	99.54	0.00	99.57
11	0.02	99.42	0.00	99.42

Table A.7 EMP results for S13 experiment.

Probe point	Si (wt%)	Fe (wt%)	Pt (wt%)	Totals (wt%)
1	0.67	94.89	4.38	100.24
2	0.67	94.03	4.23	99.17
3	0.69	94.41	4.32	99.90
4	0.69	92.22	4.34	97.48
5	0.61	94.29	5.19	100.37

Table A.8 EMP results for S15 experiment.

Probe point	Si (wt%)	Fe (wt%)	Totals (wt%)
1	12.45	87.61	100.06
2	13.65	86.14	99.79
3	14.92	84.55	99.47
4	15.65	83.74	99.39
5	16.07	83.66	99.73
6	16.16	82.89	99.05
7	16.10	83.21	99.31
8	16.27	83.24	99.51
9	16.11	83.73	99.84
10	15.77	84.21	99.98
11	15.29	84.86	100.15
12	13.74	86.19	99.93
13	13.01	86.64	99.65

Table A.9 EMP results for L11 experiment.

Probe point	Si (wt%)	Fe (wt%)	Totals (wt%)
1	11.81	87.24	99.05
2	12.36	86.76	99.12
3	12.07	86.43	98.50
4	11.78	86.44	98.22
5	11.14	87.25	98.39
6	10.68	87.56	98.24
7	10.34	87.75	98.09
8	10.44	87.09	97.53
9	9.72	86.39	96.11
10	10.49	87.62	98.11
11	7.93	88.26	96.19
12	10.10	89.17	99.27
13	9.42	88.28	97.70
14	10.17	89.25	99.42
15	10.35	88.85	99.20
16	10.20	88.38	98.58
17	10.66	88.17	98.83
18	10.89	87.85	98.74
19	11.41	87.21	98.62
20	11.20	87.84	99.04
21	11.64	86.96	98.60
22	9.47	89.47	98.94
23	9.53	89.82	99.35
24	10.79	88.44	99.23

Table A.10 EMP results for L12 experiment.

Probe point	Si (wt%)	Fe (wt%)	Totals (wt%)
1	13.70	86.12	99.82
2	12.36	86.83	99.19
3	14.00	85.79	99.79
4	14.89	84.93	99.82
5	15.41	84.73	100.14
6	17.11	83.40	100.51
7	17.40	82.64	100.04
8	17.78	82.17	99.95
9	17.35	82.47	99.82
10	16.21	83.33	99.54
11	14.61	84.56	99.17
12	11.99	87.81	99.80
13	9.23	89.01	98.24
14	12.18	86.75	98.93
15	0.38	98.80	99.18

Table A.11 EMP results for L13 experiment.

Probe point	Si (wt%)	Fe (wt%)	Totals (wt%)
1	12.17	87.10	99.27
2	14.59	85.35	99.94
3	16.09	83.58	99.67
4	16.57	82.94	99.51
5	17.39	82.38	99.77
6	17.64	82.12	99.76
7	17.69	82.04	99.73
8	17.81	82.11	99.92
9	18.07	81.73	99.80
10	17.54	81.97	99.51
11	16.91	82.44	99.35
12	15.94	83.52	99.46
13	12.84	86.39	99.23
14	6.44	92.45	98.89
15	3.94	95.03	98.97

Curriculum Vitae

Name: Soushyant Kiarasi

Post-secondary Education and Degrees:

Shahid Beheshty University
Tehran, Iran
1997-2002 B.Sc.

Azad University Tehran North Branch
Tehran, Iran
2004-2006 M.Sc.

The University of Western Ontario
London, Ontario, Canada
2008-2013 Ph.D.

Honours and Awards:

1St Honor student in the PhD national entrance exam
2006

CGU-CMOS travel award Geophysics Travel Scholarship
2010

Graduate Thesis Research Award
2011-2012

Western Graduate Research Scholarship (WGRS)
2008-2012

Related Work Experience

Research Assistant in HPT Mineral Physics Laboratory
Skilful in operating Multi Anvil Press machines
The University of Western Ontario
2008-2012

Teaching Assistant
The University of Western Ontario
2008-2012

Publications:
2006 – Kiarasi, S. Piezomagnetic Anomalies before Earthquake Occurrence (MSc. Thesis).
2008 – Mokhtari, M., and Kiarasi, S. The pattern and magnitude of rotational piezomagnetic anomalies along the dip-slip Mosha fault, Northern Tehran, Iran. *Nat. Hazards Earth Syst. Sci.*, 8, 1293-1297.
2010 – Kiarasi, S., and Secco, R. Heat Conductivity of Binary Fe Alloys through the Melting at High Pressure, Canadian Geophysical Union Meeting (CGU), Ottawa.

2013 – High pressure- temperature electrical resistivity experiments on Fe-Si alloys bearing on conductive heat flow at the inner-outer core boundary. (PhD thesis).

2013 – Kiarasi, S. and Secco, R. Electrical resistivity of iron-silicon alloys under high pressure and temperature. American Geophysical Union Meeting (AGU), San Francisco.